Members of the Jury:

Professor Yves Zech, Université catholique de Louvain (Supervisor)
Professor Jean Berlamont, Katholieke Universiteit Leuven
Professor Jean-Michel Hiver, Université Libre de Bruxelles
Professor Sandra Soares Frazão, Université catholique de Louvain
Professor Jean-François Remacle, Université catholique de Louvain (President)

Université catholique de Louvain

Ecole Polytechnique de Louvain (EPL)

Institute of Mechanics, Material and Civil engineering
(iMMC)

FLUVIAL MORPHODYNAMICS IN SUPER- AND TRANSCRITICAL FLOWS

EXPERIMENTAL AND ANALYTICAL APPROACHES

Thesis presented for the degree
of Doctor in Engineering Sciences
by

MOURAD BELLAL

August 2012

A ma mère Yezza,
Aujourd'hui, c'est à toi que je pense

A mon père Mohamed,
A mon épouse Faïza,
A mes enfants Camil, Yanis et Manil Sami

Remerciements

Cette thèse fut entamée il y a quelques années déjà et nombreux sont celles et ceux qui ont contribué de près ou de loin à ce travail de longue haleine. A cette occasion, je voudrai leur témoigner ma profonde gratitude.

Avant tout, je tiens à remercier mon promoteur, Yves Zech, qui m'a intégré dans son équipe et qui m'a initié à la recherche. Je voudrai le saluer pour son sens de la précision et pour ses remarques pertinentes qui m'ont aidé à aller vers l'essentiel et à hisser le niveau de cette thèse. Je tiens aussi à lui exprimer toute ma reconnaissance pour l'aide et la collaboration que j'ai trouvées auprès de lui. En particulier, la dernière année de cette thèse, lors de mon retour pour finaliser ma rédaction après plusieurs années d'absence pris par le monde de l'entreprise. Malgré toute la discontinuité dans la cadence de mes recherches, il m'a donné l'occasion d'aller jusqu'au bout. Aujourd'hui, je lui dis du fond du cœur « CHOUKRAN ».

Mes remerciements vont également aux professeurs Jean Berlamont de la Katholieke Universiteit Leuven et Jean-Michel Hiver de l'Université Libre de Bruxelles qui ont accepté de faire partie de mon comité d'encadrement. Ils ont bien voulu continuer l'aventure doctorale malgré ma longue absence. Je les remercie pour le temps consacré à la lecture de mes différents textes. Je leur exprime ma profonde gratitude pour m'avoir reçu dans leur bureau tout au début de cette thèse. Les échanges et les discussions que j'ai eus avec eux lors de ma défense privée ont été très intéressants et de grande qualité. Ceci m'a permis de corriger certaines erreurs, d'apporter plus de clarté à mon texte et de l'améliorer nettement.

Le professeur Sandra Soares m'a été d'une grande aide pour boucler cette thèse en m'encourageant à franchir les différents étapes et examens. Elle m'a aidé sans me le dire, je l'ai lu entre les lignes, Je tiens à lui exprimer toute ma reconnaissance. Je la remercie aussi d'avoir accepter de faire partie de mon jury et de consacrer des heures de son temps pour lire mes différents

textes malgré son planning très chargé. Ses corrections et ses conseils m'ont été très utiles.

Je remercie le professeur Jean-François Remacle, vice-président de l'institut iMMC, pour avoir accepté d'assurer la présidence de mon jury de thèse. Les discussions avec lui sur la partie mathématique et méthodologique lors de ma défense privée m'ont été très utiles. Je tiens à le remercier et à le saluer pour sa gestion de la réunion de défense privée.

Dès le début de cette thèse, j'ai rencontré Hervé Capart qui est actuellement professeur à la National Taïwan University. Nous avons échangé et collaboré sur plusieurs aspects de mon travail, notamment sur les diverses solutions analytiques comme le témoigne les nombreux articles sur les solutions analytiques déjà publiés et certains en cours. Je n'oublie jamais que les nombreuses discussions que nous avons eues ensemble m'ont été d'une grande utilité. Je tiens à lui exprimer tous mes remerciements pour toute cette collaboration, pour la qualité scientifique de ses conseils mais aussi pour l'Homme qu'il est et en qui j'ai trouvé un bon soutient surtout durant ma traversée du désert.

Le professeur Michael Reissig de la Fakultat fur Mathematik und Informatik, Institut fur Angewandte Analysis, Freiberge (Deutschland) a accepté de me recevoir dans son service en prenant en charge la totalité des frais de ce séjour scientifique. Je le remercie aussi pour ses conseils et les nombreuses heures qu'il m'a consacrées pour discuter des problèmes de frontières mobiles et leurs solutions dans les systèmes de référence mobile.

Je voudrai également remercier les professeurs Jean- François Thimus et Alain Holeyman du pôle génie civile pour leur sympathie et leur gentillesse.

La réalisation de cette thèse était aussi l'occasion pour moi de collaborer avec Michele Iervolino (Università degli Studi di Napoli "Frederico II"), en particulier sur l'utilisation du modèle numérique de Leopardi pour la modélisation des écoulements transcritiques.

J'ai eu l'occasion de côtoyer de nombreuses personnes et de collaborer avec elles au sein de l'équipe d'hydraulique. Je tiens à saluer Benoit Spinewine pour nos échanges divers, en particulier dans l'imagerie digitale pour une partie de mes expériences. Je remercie tout aussi particulièrement Céline Savary pour m'avoir permis d'utiliser les résultats numériques qui figurent dans une partie de mes comparaisons concernant les écoulements transcritiques. Merci à Laurent Goutière pour les discussions fructueuses que j'ai eues avec lui notamment sur les solutions analytiques des valeurs propres. Je souhaiterai témoigner ma gratitude aux autres collègues et anciens collègues de l'équipe d'hydraulique : Catherine Swartenbroekx, Rui Aleixo, Sylvie Van Emelen, Chien Pham Van, Christine Dal Cin, Didier Bousmar, Nicolas Dubois, Damien Christiansen, Laurent Delattre, Quentin Fraselle et Nicolas le Grelle.

Je remercie également mes autres collègues et mes ex-collègues du pole Génie civil : Patrick Conde Pérez, Mohamed Talbaoui, Laurent Mbumbia, Malek Allani, Sami Hamdi, Nicolas Denies, Kelly Guerrier et Berthomieux Junior. Tous mes remerciements vont aussi à Steeve Ambroise pour les intéressantes discussions sur Matlab. Un grand merci Christophe Frippiat pour ta disponibilité. Tu as consacré une partie de ton temps à lire le chapitre 2 de ma thèse malgré tes nombreux engagements.

Les expériences sont une composante principale de cette recherche et le staff du laboratoire m'a été d'une grande aide que soit lors des discussions consacrées aux aspects de conception du modèle physique ou sur la partie acquisition des données lors des essais. Le travail au sein du laboratoire était une réussite totale grâce aux compétences des techniciens, notamment André Renard, Alex Bertholet, Eric Dupuis, Vincent Forzée, Stéphane Gorski, Philippe Halloy, Hassan Kamhi, Francis Goffin et Eugène Bouchonville. Tout ceci n'aurait pas été possible sans la disponibilité de Guy Henriet. Je le remercie de m'avoir permis de profiter des ressources du laboratoire. Merci enfin à Viviane Misson et Marie-Rose Bodart pour leurs compétences mises au service de chacun.

La réalisation de cette thèse était aussi une agréable occasion d'encadrer des étudiants pour des travaux de fin d'études: Cédric Dewandre, Nicolas

Losseau, Laurent Boxus, Cedric de Roover, Tran Khai et Bruno Vande Meerssche. Je tiens à leur que c'était un plaisir de travailler avec vous.

Merci également à José Flémal pour la qualité de certaines illustrations présentées dans ce document. Sa gentillesse et sa disponibilité ont été remarquable.

A Faïza Bellal qui a lu cette thèse, merci pour les corrections que tu as apportées à mon anglais.

Merci à tous mes amis qui, en dehors de mon travail et de cette recherche, m'ont permis de voir et de parler d'autres choses. J'ai nommé Hamid Bendifallah et Djamel Bellal.

Je ne saurai terminer sans exprimer ma profonde reconnaissance à mon épouse Faïza pour ses sacrifices et son soutien sans faille, mes enfants Camil, Yanis et Manil Sami pour leur patience les dernières années de cette recherche. Sans leur présence, je n'aurai certainement pas été jusqu'au bout de cette aventure.

Table of contents

Remerciements vii

Table of contents xi

Notations xv

Chapter 1 : Introduction 19

Chapter 2 : Laboratory set-up and brief description of experiments on the morphodynamics evolution of super- and transcritical flows 29

2.1 Introduction 29

2.2 Experimental set-up: the sediment flume 30

2.2.1 Flume description 30

2.2.2 Settling tank 31

2.2.3 Sediment feeder 34

2.3 Measuring devices and procedures 37

2.3.1. Electronic profiler and ultrasonic probe 38

2.3.2 Imaging apparatus 39

2.3.3 Imaging method 41

2.3.4 Interface identification 41

2.4. Material properties 42

2.5. Tests configurations 43

Chapter 3 : Mathematical analysis of governing equations and derivation of general mathematical structure of morphodynamics diffusion model 47

3.1 Introduction 47

3.2. Governing equations 48

3.3 Eigenvalues analysis and boundary conditions 50
3.3.1 Method of partial derivatives 50
3.4 Analytical expressions of the Eigenvalues of the Saint-Venant – Exner equations 57
3.5 Diffusion model in fluvial morphodynamics 61
3.5.1 Introduction 61
3.5.2 Linear diffusion equation 62
3.5.3 General self-similar structure 68
3.5.4 Restrictions on the initial and boundary conditions in similarity structure 74

Chapter 4 : Fluvial morphodynamics in supercritical flow over mobile bed: Aggradation and degradation 77
4.1 Introduction 77
4.2 Experiments of aggradation and degradation 78
4.2.1 Description 78
4.2.2 Experimental procedure 79
4.3 Analytical solution for aggradation and degradation in supercritical flow 80
4.3.1 Transient bed profile 80
4.3.2 Harmonics calculation 84
4.4 Approximation of the equilibrium bed slope in the steep-sloped reach from few bed level measurements 86
4.5 Numerical simulation: SedRiv model 87
4.5.1 Numerical algorithm 88
4.5.2 Limitation of Preissmann scheme for transcritical flow 89
4.6 Comparison of results and discussion 90
4.6.1 Equilibrium bed slope simplified expression results comparison 90
4.6.2 Analytical solution results comparison 91

4.7 Conclusions 94

Chapter 5 : Fluvial morphodynamics in transcritical flow over mobile bed: Sediment front and hydraulic jump 95

5.1 Introduction 95

5.2 Experiments of hydraulic jump and prograding sediment front 97

5.2.1 Description 97

5.2.1 Experimental procedure 98

5.2.3 Experimental results 100

5.3 Self-similar solution for the prograding sediment front 109

5.4 Finite difference solution 116

5.5 Numerical simulations 120

5.5.1 Two-layer model 120

5.6 Comparisons 122

5.7 Conclusions 129

Chapter 6 : Fluvial morphodynamics in transcritical flow over mobile bed: Knickpoint and critical section 131

6.1 Introduction 131

6.2 Experiments of knickpoint and critical section 133

6.2.1 Description 133

6.2.2 Experimental procedure 133

6.3 Self-similar solution for knickpoint migration 140

6.3.1 Kinckpoint migration in infinite channel 140

6.3.2 Knickpoint migration in finite channel 146

6.4 Numerical simulations 153

6.4.1 Two-layer model 153

6.5 Comparisons 155

6.6 Conclusions 159

Chapter 7 : Conclusions 161

References 167

Notations

Roman

A	Cross section
A_0	Conventional area comprise between the river bed and arbitrary reference
A_1, B_1,	Constants determined from boundary conditions
A', B'	Constants determined from the boundary conditions
A_n	Coefficient of Fourier Series
A_0	Coefficient of Fourier Series corresponding to the first harmonic $n=0$
c_1, c_2, c_3	Information celerities
C_1	Constant determined from boundary conditions
$\hat{C}$	The mean volumetric sediment concentration in the mixture (on A)
C_b	Sediment concentration in the bed
C_d	Drag coefficient
$C_{f,w}$	Friction coefficient for water
$C_{f,m}$	Global friction coefficient (one velocity model)
C_f	Chezy friction coefficient
C_iA	Analytical expressions of the eigenvalues
$C_{H1,2}$	Hydrodynamic eigenvalues
C_s	Sediment concentration in the transport layer
D	constant diffusion coefficient
d_m	Median sediment diameter d_{50}
e_b	Erosion rate
e_s	Displacement of the interface z_s
exp	exponential function
$f(\sigma)$	dimensionless function of dimensionless argument express the shape of the profile
$f'(\sigma)$	First derivative of the shape function

$f''(\sigma)$	Second derivative of the shape function
$f_1(\sigma)$	One of the basis solutions of second order linear ODE
$f_2(\sigma)$	The second basis solutionS of second order linear ODE
Fr	Froude number = $u/\sqrt{gh}$
$\mathrm{Fr}_0^{\mathrm{up}}$	Initial Froude number upstream
$\mathrm{Fr}_0^{\mathrm{dwn}}$	Initial Froude number downstream
g	Acceleration due to gravity
h	Water depth
h_s	Transport layer depth in the two-layer model
$H_{w,\mathrm{down}}$	Downstream water depth
h_w	Water depth in the 2L model
ierfc	The integral of the complementary error function
L	Channel length
Ls	Settling length
n	Manning roughness coefficient
n_b	Manning roughness coefficient relative to the bottom
n'_b	Manning roughness coefficient taking grain roughness into account
n_w	Manning roughness coefficient relative to the walls
q	Unit water discharge
q_s	Unit solid discharge
R	Slope of the submerged delta foreset
R_h	Total Hydraulic radius
R_b	Hydraulic radius related to the bed
s	Relative density of the sediments
S_f	Friction slope = head loss per unit length
S_0	Bottom slope
s_1	Position of the upstream moving boundary
s_2	Position of the downstream moving boundary
$s(t)$	Moving boundary position $s(t) = 2\lambda\sqrt{Dt}$
S_1	Upstream bed slope
S_2	Downstream bed slope
S_0^{∞}	Equilibrium bed slope

S_0^{up}	Bed slope upstream the nickpoint
S_0^{dwn}	Bed slope downstream the nickpoint
t	Time
T_n	Characteristic response time
T_0	Characteristic response time for the first harmonic $n=0$
T_s	Settling time
$U(x, t)$	general invariant solution defined such that $u(x,t) = t^{k/2}F(xt^{-1/2})$
u	Mean velocity in the x-direction
V^i	Initial stored sediment in the flume
V^∞	Equilibrium stored sediment in the flume
x	Abscissa along the channel axis
z	Vertical co-ordinate, level
z_b	Bed level
z_b'	Transient bed level
z_b^∞	Equilibrium bed level

Greek

Δx	Distance increment
Δt	Time increment
ε_0	Porosity
θ	Time weighting coefficient
λ	Scaling constant
μ	Dimensionless coefficient which control the rate of lake level change
ν	Kinematic viscosity
ρ_b'	Volumetric mass of the bed
ρ	Volumetric mass of the water
ρ_s	Grain volumetric density
ρ_s'	Transport layer volumetric density
ρ_w	Water volumetric density
σ	dimensionless argument defined such that $\sigma = x/\xi(t)$
σ_g	Sediment gradation coefficient
τ_b	Lower shear stress along moving / at rest sediments interface
τ_{*c}	Critical shear stress = τ_{crit}
τ_s	Upper shear stress along moving / at rest sediments interface

τ_{sw}	Lower shear stress at clear water / moving sediments interface
τ_{w}	Shear stress at clear water / moving sediments interface
τ_{ws}	Lower shear stress at clear water / moving sediments interface
φ	Space weighting coefficient
χ_1, χ_2	Non dimensional factors associated to the sediment transport
$\xi\,(t)$	an evolving length scale

Subscripts

0	Relative to the initial time
b	Relative to the bottom/bed
fw	Relative to the friction between the water layer and the transport layer
fs	Relative to the friction between the transport layer and the fixed bed
i=1,2	Index to indicate boundary values
k=1	Exponent of general invariant solution corresponding to used form
k= 0	Exponent of general invariant solution corresponding to the classical Neumann solution
j	Time level
L	Relative to the left side
R	*Relative to the right side*
s	Relative to the sediment transport layer
sw	Relative to both the sediment and the water layers
w	Relative to the water

Superscripts

$'$	Relative to the intermediate state
∞	Relative to the equilibrium state

Chapter 1

Introduction

River system is generally in natural equilibrium under some controlling parameters: bed slope, liquid discharge, sediment characteristics and bed-load discharge. If any perturbation occurs, either natural as floods or landslide, or artificial as dams or check dams, this perturbation may change the hydraulic regime and the sediment transport mode.

Among many others, we could mention two examples of such natural perturbation: the 1987 flooding of the Mallero at Sondorio in Northern of Italy (Di Silvio and Peviani, 1989), where the flooded city was located only 12 Km downstream of the nearest landslide that overloaded the river with sediments, and, on the other hand, the massive aggradation of the Ok Tedi river at Tabubil in a mountain area due to landslide (Fig 1.1). Artificial perturbations to the river course could be an effect of man fight against flood threats: human have developed many control techniques such as levees, check dams (Fig 1.2) or sills. Such an obstruction placed across the channel, where supercritical flow dominates, may create a transition in the flow regime when a sudden rise of the downstream water level generates a back-water effect or a hydraulic jump. The resulting prograding sediment front propagates downstream. Figure 1.3 shows a small mountain dam with a hydroelectric plant that was recently put out of service due to the nearly complete backfill of the reservoir by a prograding alluvial delta. It took only one year for the delta front to advance from the dashed line marked on the photo to its current oblique position (Fig 1.3).

Another example of the perturbation induced by man activities is the intensive gravel exploitation on the Wilson river which caused bed degradation over 14 km (Fig 1.4). Aggradation, degradation and the ultimate equilibrium profile depend a lot on the flow conditions.

Figure 1.1: Massive aggradation of Ok Tedi river at Tabubil in mountain area after a landslide, 1984 (http://www.rettet-die-lbe.de/oktedi/environ2.htm)

Figure 1.2: Slit dam, Italy (Armanini et al.,2002)

Figure 1.3: Delta front prograding into standing water: Ronghua Dam, Northern Taiwan, November 2005(photo by A.T.H. Perng).The dashed line in the background shows the location of the delta front in August 2004

Figure 1.4: Wilson River, NSW, Australia. 14 km degradation by gravel exploitation (http://www.hastings.nsw.gov.au /www/html/3844-river-rehabilitation.asp).

Usually, fluvial regime prevails in most of the alluvial rivers: subcritical flow is predominant, during most of the time. However, the most drastic alterations in river morphology happen during floods and are thus associated with sudden changes in discharge and water level. Moreover, intense erosion and deposition may disrupt the river features forming a sequence of breaks in the bottom slope. Regime discontinuities may appear, such as hydraulic jumps and control sections, leading to transcritical flow.

Besides, supercritical flows are found mostly in mountain environments. From a topographical point of view mountain rivers can be defined as rivers that directly drain catchments areas, and convey water and sediment from mountainous headwaters to a river system. In many ways rivers in mountainous regions differ from lowland-rivers. Mountain rivers can be characterised by: (a) Steep and non uniform slopes, (b) Small watersheds, (c) Flows with higher turbulence.

The development of rich and accessible parts of mountainous regions has also raised a need of protection measures and warning systems against hazardous fluvial impacts. One of the control policy strategy of mountain streams is the prevention of bedload sediment transport by check dams (Armanini et al., 1989; Larcher , 1998).

In order to predict conveniently the river morphological evolution, it is thus required to model supercritical flow as well as subcritical. Also transitions from one regime to the other have to be captured.

The present work aims at modelling the morphodynamics of super- and transcritical flows. It is important to understand the mutual interaction of the upstream and downstream boundary conditions and their impact on river bed evolution (Cui, 1995; Sieben, 1997). Also flow transitions that control the morphology require better description (Zech, 1996).

The present investigation was carried out using three complementary approaches: experimental work, analytical self-similar formulations and numerical simulations, these latter aiming at validating the analytical solutions.

The experimental set-up has been designed and constructed in the frame of this thesis with the help of graduate students to conduct a series of experiments, which represent idealised situations appropriate to validate analytical and numerical calculation. The conception of the existing experimental set-up has been completed by a sediment feeder designed to supply a constant solid discharge distributed uniformly during the whole test; the downstream sediment decanter is dimensioned to settle the smallest grain size of the used sediment. The experiments should also provide better knowledge of the flow mechanisms thanks to visual observations trough glassed walls also allowing accurate measurements by means of digital imagery (Spinewine and Zech, 2000).

The first experimental campaign concerned aggradation and degradation corresponding sediment overloading and underloading conditions in fully supercritical flow. Subsequently, a series of experiments featuring transcritical flow over mobile bed have been conducted in situations presenting a hydraulic jump and a critical section. Digital imagery technique has been used to detect the earlier rapid stage of bed deformation and the upwards propagating of the sediment humps.

Some aspects, while present in real cases, are not considered here: graded sediment; variable geometry, etc. Another limitation was imposed by the size of the experimental set-up and the sediment feeder: experiments requiring large space or long time scales were excluded.

Regarding modelling aspects of super- and transcritical flows, using either analytical or numerical approach, it is useful to recall the classical eigenvalues analysis of the Saint-Venant–Exner equations (Vreugdenhil and de Vries, 1967; Cunge et al., 1980; Zech, 1994; Altinakar, 2002). This analysis constitutes a guide for the specification of boundary conditions and leads to three characteristics describing the celerity of perturbations, two of them are positive and one is negative. Therefore, three boundary conditions must be fixed, two at the upstream, one at the downstream boundary.

Most of the analytical solutions for transient river bed consider low-land rivers. Several authors (Yen et al., 1987; Yen et al., 1992; Bianco et al., 1994) have experimentally observed the asymptotic character of the equilibrium resulting from sediment overloading and underloading in reaches of finite length. In particular, their measurements exhibit a well defined response time for which Yen et al. (1992) have proposed an empirical characterisation. For channels of infinite length, analytical solutions such as proposed by Soni et al. (1980), Jain (1981) and Gill (1983), based on the linear diffusion model of de Vries (1973), are known to compare reasonably well with experimental measurements, those of Soni et al. (1980) constituting the main empirical reference. Analytical solutions have been derived as well for channels of finite length (Gill, 1983), but do not appear to have been confronted with experimental data.

In the framework of analytical approaches, a linear diffusion equation can be obtained under the non realistic consideration that the flow is everywhere close to the steady uniform regime defined by the local bed gradient. So the solid discharge becomes a function of the local bed slope S_0 only.

Seminal works, in which this diffusion equation has been used to solve sediment motion problems, include de Vries (1973), Begin et al. (1981), Ribberink and van der Sande (1985), and Paola et al. (1992). In the case of steep-sloped river beds evolving under supercritical flow in finite channel, the linear diffusion equation is resolved in fixed boundaries and the solutions are developed using Green functions or Fourier series.

In the case of transcritical flow, at least one of the two boundaries is supposed to evolve in time, downwards for the prograding sediment front and upwards in the case of the erosive knickpoint front. The mathematical problem becomes more complex, as the diffusion equation has to be solved in moving domain. In that case, exact self-similar solutions can be derived by exploiting the symmetries of the diffusion equations.

More recently, moving boundary problems have been solved analytically for various alluvial phenomena, including prograding deltas (Voller et al., 2004, Lai and Capart 2007), migrating bedrock-alluvial transitions, (Lai and Capart 2009), and the formation of tributary-dammed lakes (Hsu and Capart, 2008).

Based on the analytical work of Voller (2004) developed for a zero channel length; in other terms the prograding delta forms and propagates in a body of standing water, the present work illustrates at the theoretical level the existence of a general mathematical structure shared by several sedimentary problems featuring semi-infinte channels evolving under diffusional sediment transport where moving boundary are considered at one end of the channels (Capart et al., 2007): bedrock-alluvial transition, lake breaching and prograding delta. Using the accurate boundary conditions, exact similarity solutions can be derived for each case.

Using the approach described above, we shall show that analytical solutions can be found for evolving profiles with migrating knickpoints. We derive an exact solution for channel reaches of semi-infinite extent on both sides of the knickpoint, and use it to construct an approximate solution for the more realistic case of a finite channel. Governing equations similar to those adopted here to treat terrestrial knickpoints were earlier applied by Mitchell (2006) to knickpoints in submarine canyons.

The third approach is numerical modeling. The numerical simulations of aggradation and degradation of steep-sloped river beds in fully supercritical flow were handled by using the SedRiv model (Zech, 1996). The implicit Preissmann finite-difference scheme (Preissmann, 1961; Cunge and Perdreau, 1973), used by Holly and Rahuel (1990) and by Correia (1992) is adopted to resolve simultaneously at each time step the set of governing equations. The implicit Preissmann finite difference scheme is stable for long time steps, which is an advantage for long-term simulations. However, the main problem is that such a method, applied on the Saint-Venant–Exner equations, is not able to model transcritical flows (Meselhe and Holly, 1997), since the number and nature of the boundary conditions depend on the flow regime. For example in the case of a transition from supercritical flow to subcritical flow via a hydraulic jump, this method does not permit to manage simultaneously two contradictory water depths, upstream and downstream of the reach.

The explicit finite-volume schemes turn out to be a right alternative for rapid transient flows, since they address the transcritical flows and capture shocks like hydraulic jumps (Leopardi, 2001). However, because of the small time step required by such an approach, it is impossible to model the morphological evolution for a long time scale.

In the present work, another numerical approach in used: the two-layer model from Savary (2007). This numerical model was initially developed by Capart (2000) and improved by Capart & Young (2002), Spinewine (2005) and Chen et al. (2007), in which more suitable treatment of the boundary conditions has been introduced (Savary & Zech, 2007). In this thesis, a one-dimensional approach is used and a unit width is considered.

According to the above considerations, the present document is organised in the following way.

The chapter 2 describes the UCL laboratory experimental set-up, where morphodynamics evolution under super- and transcritical flow has been experimented. The guidelines in the design of the different parts of the experimental set-up are explained: the flume, the sediment feeder and the downstream decanter. The measuring devices and procedures are also explained: probes and digital imagery techniques. Finally a brief introduction to the various cases is proposed: aggradation and degradation in fully supercritical flow, knickpoint evolution, control section migration and the sediment front movement.

In chapter 3, the system of partial differential equations that represents a cross-sectionally integrated flow over a mobile bed is analysed trough a classical eigenvalues analysis. This analysis concerns the behaviour of solutions and the type and number of boundary conditions for sub-, trans- and supercritical flows regimes. A novel and accurate approximation of those eigenvalues developed in Goutière et al. (2008) will be presented and finally a general mathematical structure of fluvial diffusion model will be explained.

The morphological evolution of steep sloped-river beds subject to supercritical flow regime is considered in chapter 4. Here analytical solutions for bed evolution, transient sediment rate and an explicit expression of time scale characteristic are considered. A numerical solution procedures based on the implicit Preissmann scheme is explained. The conducted experiment related to aggrading or degrading steep sloped river beds is detailed. A comparison and an analysis of the results of the three approaches conclude this chapter.

Chapter 5 describes experimental, analytical and numerical approaches to morphodynamics evolution of transcritical flow over mobile bed in presence of hydraulic jump and sediment front. This transition in flow regime is a consequence of the incompatibility between upstream and downstream boundary conditions (water level imposed upstream and downstream). The use of digital imagery in the tests allow to identify two stages of bed deformation confirming the theoretical analysis of Sieben (1999), a sudden decrease of bed shear stress induces a bed deformations: (a) first humps propagating upstream until the downstream water level get stable and afterwards (b) the prograding sediment front propagating downwards. Self-similar solution has been developed considering the prograding sediment front evolving under diffusional sediment transport. Moving boundary is taken into account downstream. Results of simulation by means of a two-layer model are compared with the experimental and the self-similar solution.

Chapter 6 describes experimental, analytical and numerical approaches solution to morphodynamics evolution of transcritical flow in transition of flow regime through control section and knickpoint. The experimental campaign concerns the knickpoint migration process, characterized by a sudden increase of the bed shear stress and a regressive front propagating upwards. Adopting the same approach as used in the analytical modelling of the prograding sediment front, an exacts self-similar solutions has been developed, first, for knickpoint migration in infinite channel length and afterwards adapted to finite channel. The results of experimental and analytical approaches are confronted to the numerical two-layer results.

Chapter 7 is devoted to draw a retrospective view on the work, formulate the main conclusions of the different results and conclude with suggestions for future research.

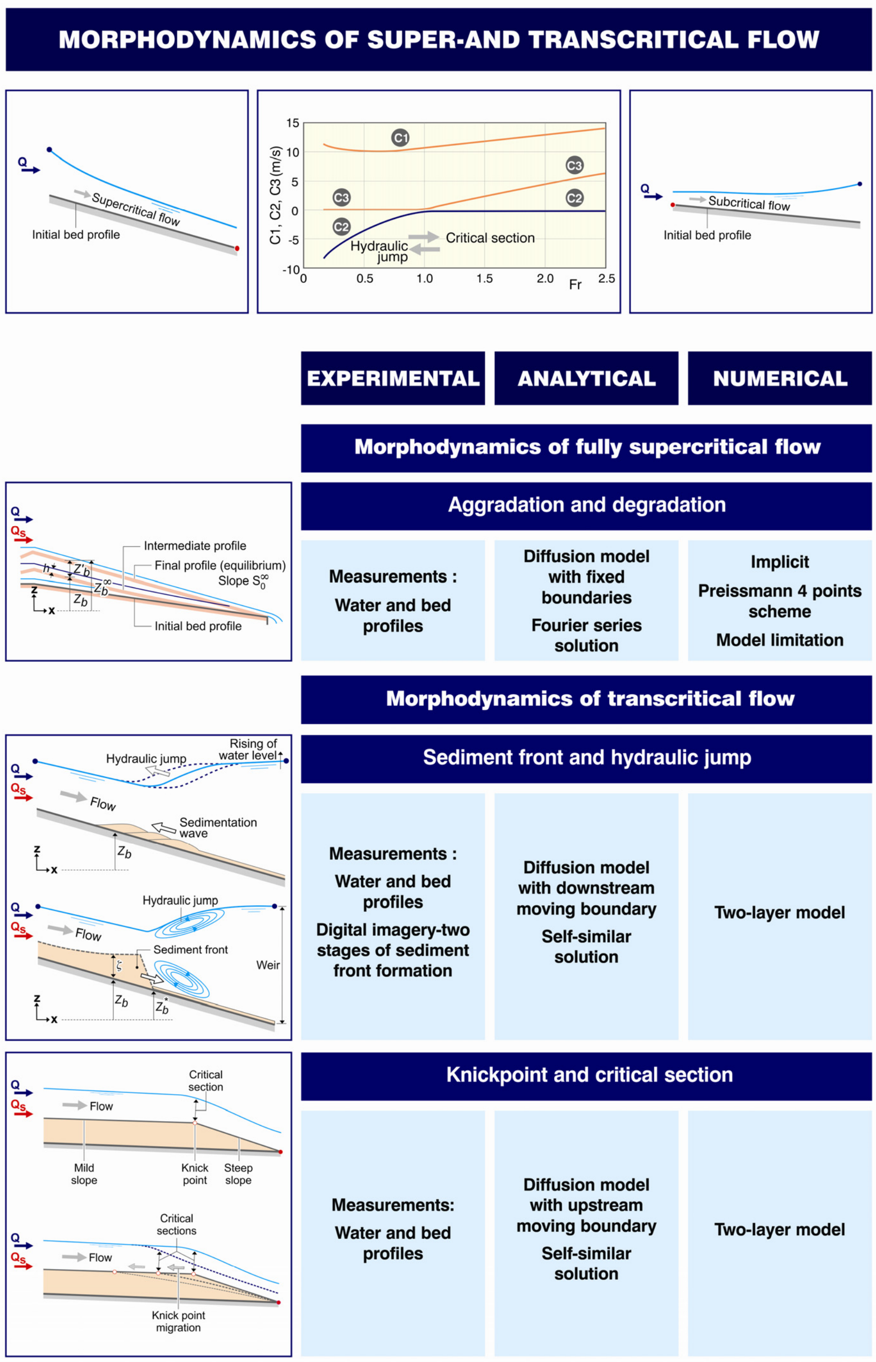

Figure 1.5: Thesis plan

Chapter 2

Laboratory set-up and brief description of experiments on the morphodynamics evolution of super- and transcritical flows

2.1 Introduction

We present the design of the laboratory set-up and a short introductive description of the experimental campaign carried out to investigate the morphodynamic evolution of the river bed in the presence of super- and transcritical flows. The experimental set-up allowed testing various morphological configurations: (a) aggradation and degradation in supercritical flow; (b) transition from subcritical flow to supercritical flow over a control section and knickpoint; and (c) transition of the flow regime from supercritical to subcritical over a hydraulic jump and a sediment front.

It is imperative that the experiments be designed with care to make sure that the test situation approximates as closely as possible the reality of the physical problem.

Such idealized experiments also have theoretical and computational importances, as they represent clear-cut situations rightly appropriate for the validation and the comparison with analytical and numerical models.

In a broad sense, aggradation-type experiments imply that the quantity of sediment entering the reach is larger than the carrying capacity of the stream. Consequently, a certain amount of sediment will be deposited and the bed level will rise. Degradation of river stretch occurs when the sediment discharge entering the stretch is lower than the sediment discharge transported downstream of the reach; the extra sediment required to satisfy the streams' carrying capacity is obtained from the erosion of the bed level and widening of the stream.

To conduct these various tests, a sediment flume was designed and constructed for this purpose. The construction and equipment of the sediment flume were done in succeeding stages whose design criteria were directed in order to ensure a good quality of experiment by combining the various limits of the experimental set-up. This will constitute the point of section 2 of the present chapter. Section 3 presents the flow instrumentation by means of electronic profiler and ultrasonic probe used to measure the water and bed profiles and digital imaging techniques used to obtain a precise visualisation of the flow and high-quality images providing good qualitative description of some rapid aspect of the experiment non noticeable by the electronic profiler such as the first humps in sediment front experiments. In section 4, we then present the test conditions and the used sediment of the experiments that will be exploited throughout the thesis.

Finally, section 5 describes the configurations of the tested cases. Experimental description is restricted here to a relatively general presentation of the flow behaviour, while more detailed aspects of the experiments will be explained with details and exploited afterwards in the corresponding chapter 4, chapter 5 and chapter 6.

2.2 Experimental set-up: the sediment flume

2.2.1 Flume description

The flume designed for the present experiments is illustrated in Fig. 2.1: a glass-walled channel with adjustable slope (from 0 to 5 %, by a steps of 1 %). On the three supports of the flume, circular perforations corresponding to each slope value are positioned in the corresponding level. The flume is linked to a water recirculation system, an upstream sand feeder supplying dry sediments at a constant rate, and a downstream settling tank. The flume is 7.6 m long, 0.5 m wide and the sand feeder is located 70 cm away from the upstream end. Side walls are made of glass with a 5-cm high steel frame at the bottom that partially obstructs lateral visual access. Under supercritical flow conditions, the water depth is self-regulated upstream through a control section at the channel entrance and water and sediments fall freely at the channel outlet.

The flume is mounted on 2x2 horizontal IPE 240 crossbeams installed on three supports. The distance between the supports of the crossbeams is 3.8 m, designed in order to keep the deformation in the horizontal plane under 1 mm over the flume length in the case of a maximum stress of 2930 N/m² (corresponding to 60 % sediment and 40% of water over whole the flume depth of 45cm). The beam theory was used to calculate the maximum deformation and the shell theory was used to confirm the result.

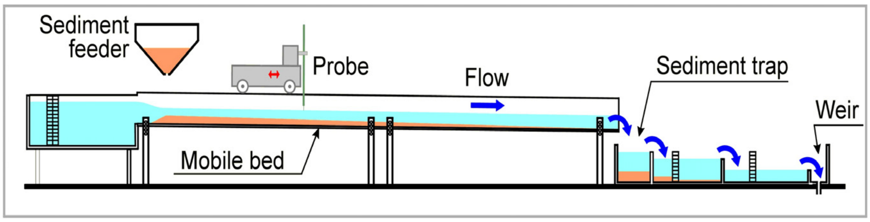

Figure 2.1: Experimental set-up of sediment flume.

2.2.2 Settling tank

Experiments with mobile bed require collecting the sediment downstream of the flume to avoid that the finest particles reach the water reservoir and the pump. For this purpose, a special attention was devoted to the design of the settling tank (Bellal et al., 2000) with the ambition to reach the above condition. The challenge lies here in the need to collect the finest sediment particles under the highest solid discharge rate condition (highest liquid discharge, highest bed slope.)

The maximum settling length corresponding to the finest solid particle was calculated as detailed in the next section.

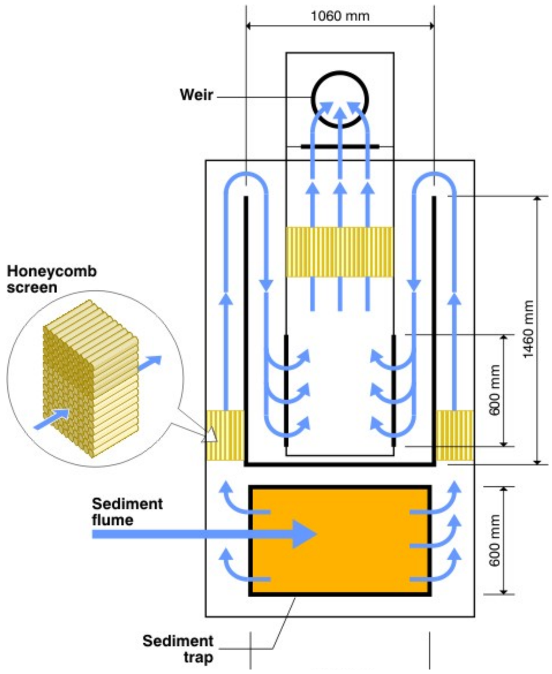

Figure 2.2: Top view of the sediment settling tank

2.2.2.1 Flow velocity and settling length

The available theoretical settling length in each channel of the settling tank (Fig. 2.2) is of 2.320 m. The mean flow velocity is calculated from the liquid discharge and the water depth. We calculate the water depth above the weir for the maximum possible liquid discharge of 30 l/s passing trough the single conduct of the settler. From the corresponding water depth of 0.515m and the liquid discharge, we estimate a maximal mean flow velocity of 0.29 m/s.

The fall velocity of a solid particle depends on the shape and the size of the particle, its density and that of the fluid, as well as the viscosity of the fluid. In addition, it depends on the depth of the fluid in which it falls, on the number of particles fallings and on the level of turbulence intensity. Turbulence conditions occur when settling takes place in a flowing fluid and can also occur when a cluster of particles is settling. Falling under the influence of gravity, the particles will reach a constant velocity - the regime velocity - when the drag equals the submerged weight of the particle. For spherical particle in a stationary fluid, the falling velocity w is given by

$$\pi \frac{d^3}{6} g(\rho_s - \rho) = C_d \pi \frac{d^2}{4} \rho \frac{w^2}{2} \tag{2.1}$$

where w is the falling velocity, ρ_s the sediment density, ρ the water density, and g is gravitation. C_d is the drag coefficient, depending on the Reynolds number

$$R_e = \frac{wd}{\nu} \tag{2.2}$$

where ν is the kinematic viscosity of water. We obtain the expression of the fall velocity

$$w^2 = \frac{4}{3C_d} gd \frac{(\rho_s - \rho)}{\rho} \tag{2.3}$$

The settling time is estimated for the maximum water depth. Considering the case of perfect rectangular settling tanks (Bellal et al., 2000), we can then use the following expression

$$T_s = \frac{h_{\max}}{w} \tag{2.4}$$

where T_s is the settling time and $h_{\max}$ is the maximum water depth. The settling length is calculated using the maximum flow velocity.

$$L_s = V_{\max} T_s \tag{2.5}$$

Diameter	C_d	*w(cm/s)*	T_S	L_S	*% passing*
0.08	45	0.62	83.57	24.23	0
0.125	20	1.15	44.57	12.92	0
0.25	5	3.27	15.76	4.57	0
0.5	2	7.30	7.04	2.04	0.01
0.8	1.2	1.19	4.31	1.25	0.02
1	0.9	15.40	3.34	0.97	0.08
1.25	0.75	18.86	2.72	0.79	1.06
2	0.55	27.86	1.84	0.53	77.23
2.25	0.52	32.04	1.6	0.46	98.61
3.15	0.48	37.43	1.37	0.39	99.93
4	0.45	43.57	1.18	0.34	100

Table 2.1: Settling characteristics for the used sediment

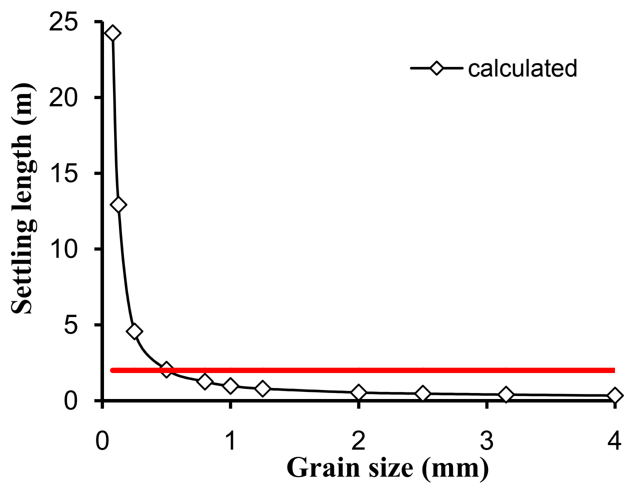

Figure 2.3: Calculated settling length for the used sediment

Considering our grain size distribution curve, the maximum needed settling length to settle the finest grains (d = 0.5 mm) is 2.04 m which implies that no sediment particle can go over the settler. The sediment collected is dried before being used again in the sediment feeder for the next experiment.

2.2.3 Sediment feeder

In order to ensure a constant solid discharge in the upstream part of the sediment flume, a sediment feeder has been designed and constructed. Small-scale models of sediment feeder with a capacity of 15 dm³ were tested, in order to check the constancy and the stability of feeding before selecting the final design of the feeding system. Two different shapes of regulating device for solid discharge were tested: rectilinear openings and circular perforations of various diameters and various equidistances (Fig. 2.4). For the rectilinear openings system, various opening widths varying from 6 mm to 20 mm have been tested.

According to the tests on small-scale models with rectilinear openings, the solid discharge is very sensitive to the opening width. Due to the difficulty in keeping constant the same opening size for reproducing the same results, the rectilinear opening system was found to be less accurate (Fig. 2.5).

On the contrary, for the circular perforations system, we can maintain a constant solid discharge value with the same perforation size and equidistance (Fig. 2.6). According to De Jaeger (1991), the minimum perforation diameter is about 7-8 times the medium sediment diameter to avoid the hindrance of the feeding system. Considering this, the second system provides constant and reproducible solid discharge. We choose the system of the circular perforations (Ø = 11 mm, 12.5 mm, 13.5 mm and 14 mm) because it is more accurate in spite of its limitation in varying the solid discharge during the same test.

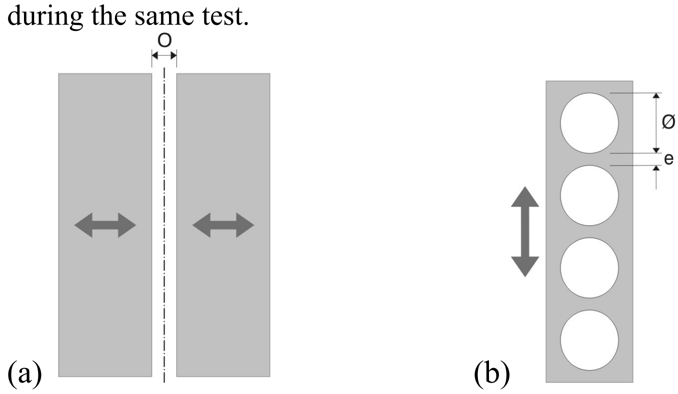

Figure 2.4: (a) Rectilinear opening system; (b) Circular opening of the feeding device

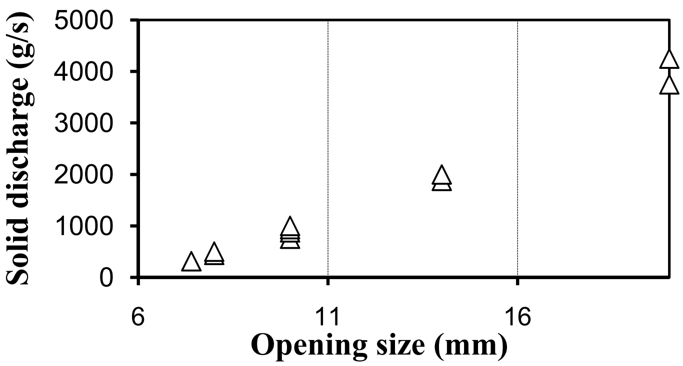

Figure 2.5: Solid discharge for the rectilinear opening system

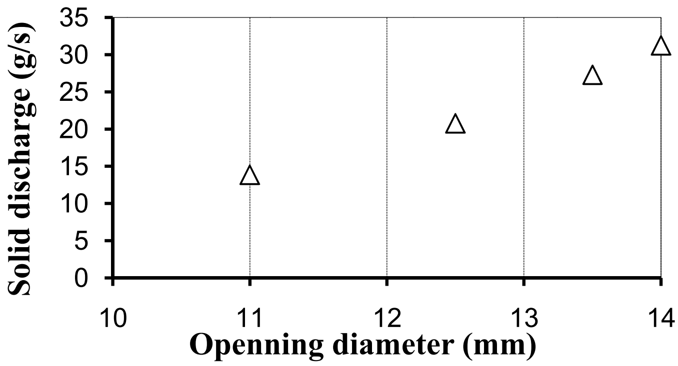

Figure 2.6: Solid discharge for the circular perforation system

The calibration of the sediment feeder is operated using a load-cell. The sediment is stored in a basket hanging to a load-cell during a time interval Δt. Each measurement is repeated several times for the same regulating device to check the recurrence of the measured value.

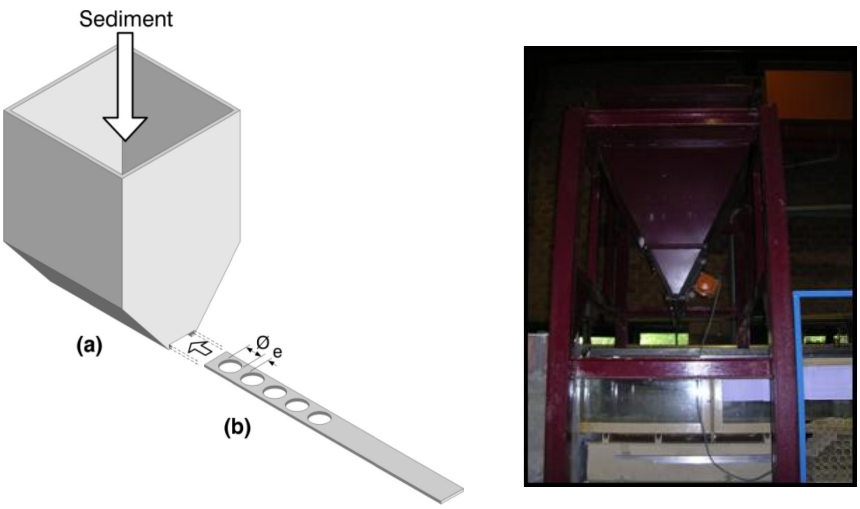

Figure 2.7: (a) Sediment silo; (b) and solid discharge regulating device

Finally, a set of four regulating devices has been chosen to regulate solid discharge in the sediment feeder. A vibrating system is fixed to the sill in order to make easy the fall of sediments. The characteristics of these devices are summarized in the table below:

Diameter of perforation	12	14	12	14
Equidistance e (mm)	100	100	50	50
Solid discharge (g/s)	128.9	185.6	270.6	360.5

Table 2.2: Main characteristics of solid discharge regulating device

The flume constructed according to the design described in the above sections was found to perform satisfactorily. Upstream, the sediment feeder was operated without problems; sediment was distributed uniformly with a constant discharge via the circular perforations over the entire section.

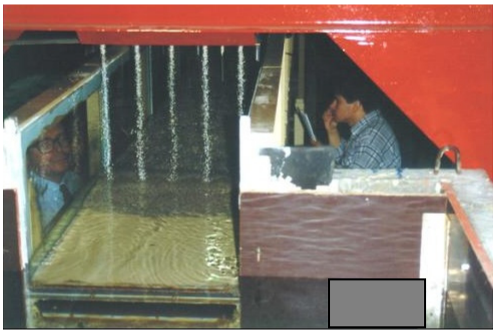

Figure 2.8: Uniform distribution of sediment at inlet of the flume

2.3 Measuring devices and procedures

Observation of water and bed levels during the tests was acquired using two different measuring systems: probes along the axis of the channel, mounted on a trolley and pulled upstream and downstream repetitively, and an imaging system.

2.3.1. Electronic profiler and ultrasonic probe

The first experiments have been operated only with an electronic profile-indicator probe (Fig. 2.9a) to measure bed and water surface profiles, one profile in each direction. Later, an acoustic probe (Fig. 2.9b) has been used during the knickpoint experiments, to complement the electronic profile-indicator probe.

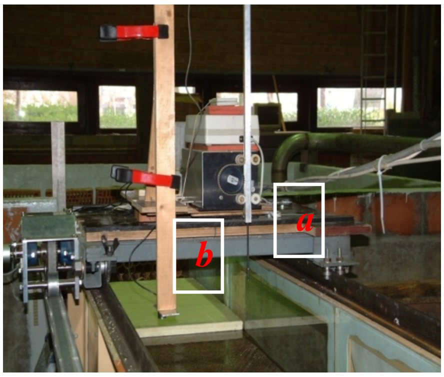

Figure 2.9: a) Capacitive profiler and b) ultrasonic probe

The electronic profile-indicator PV-07 has been developed by Delft Hydraulics to measure continuously water or bed profile. The instrument consists of a needle, placed vertically in the water. A servo-mechanism maintains the point of the probe at a constant distance (adjustable to 0.5 – 2.55mm) above the bed. When the instrument is being displaced in horizontal direction, the probe will follow the configuration of the bed or water surface continuously. The principle of the operation is the appreciable difference between the electric conductivities of water and bed material.

The ultrasonic probe Keyence UD-500 has been used to measure water surface profile. This probe is composed of a source of ultrasonic waves and a receiver that picks up the signal reflected from the free surface. The analysis of this signal allows having the distance from the water surface. The resolution of measurement is ± 0.1 mm.

A potentiometer 46HD20 10K Bushingmount attached to the trolley enables the position of the probe to be indicated.

Liquid discharge is supplied trough an upstream reservoir with a constant level in such a way that accurate discharge control is possible, independently from the pump working. Flow rate in the interval Q = 0 .. 30 l/s is available and discharge measurement is completed by means of an electromagnetic flow-meter (ABB-MAG-XE), with an accuracy of 0.25 %. Several equipments are used in order to smooth calm the flow at the supply-pipe end in the inlet tank: (1) metallic fibres mesh, wrapped around the pipe; (2) a honeycomb screen, ensuring parallel flow (Fig. 2.10).

Figure 2.10: Settling device at the flume inlet

All the instruments have been connected to an acquisition card. Signals of data have been transformed from analogue source to a computer in numerical format.

2.3.2 Imaging apparatus

The observation of unperturbed flow and bed movement is not allowed for more than 90 cm as lateral view because of the steel structure separating each module of the flume. For this reason, we have to deal with this design limitation and treat the acquired images in the field of 90 cm.

A single fast digital camera (Dalsa DS-21-001M0150 CMOS) was used to acquire sequences at frame rate of 2 images per second with a resolution of 1024x1024 pixels. This camera gives image with 8-bit digital output or 256 grey levels. The camera was installed on a camera head which was placed at a chosen position, adjusted horizontally at a fixed distance of the sidewall. The focal distance of the lens used with the camera was chosen to cover a field of view of 90 cm for the sediment front tests and knickpoint tests.

Two frontal spots head of 5000 watts each were used to provide lighting, positioned to guarantee uniform illumination of the scene and avoid direct reflections of light towards the cameras. The back side wall of the flume in the operating area was covered with an external white leaf to have a uniform background. The used apparatus is schematised in Fig. 2.11.

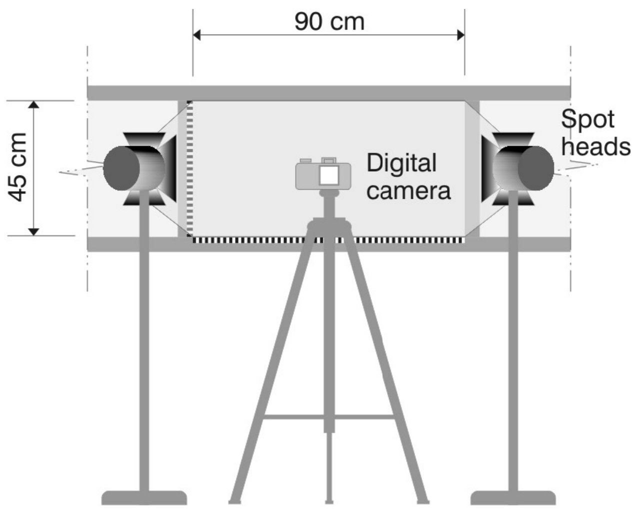

Figure 2.11: Imagery apparatus

Besides side-view imaging, probe measurements include flow and bed profile measurements, which give a good description of the bed and water profiles evolution.

2.3.3 Imaging method

Besides qualitative visual interpretation, the image sequences (for example Fig. 2.12 and 2.13) were analysed quantitatively with a method which aims at identifying the interfaces separating water and bed profiles (Spinewine and Zech, 2002). The viewing window was chosen to observe the formation and initial development of the sediment front, and extends from 2.9 m to 3.8 m from the upstream end of the flume. The bed elevations were checked to remain always higher than the steel plate at the bottom of the side-wall, allowing full visual access to the bed profile. Special attention was paid to the lighting conditions, in order to ensure good contrast between the sediment, water and air regions on the images.

2.3.4 Interface identification

Based on the pioneering work of Capart (2000) and the successive improvements of Spinewine and Zech (2002) and Spinewine et al. (2003), the imaging method allowed the identification of the characteristic flow regions on the images related to sediment front and hydraulic jump, for example. Specific image processing algorithms, mainly involving a combination of low-pass and high-pass filters, were developed to highlight the position of water and bed profiles on the images. Accurate positioning of both interfaces was then obtained automatically (Fig. 2.14).

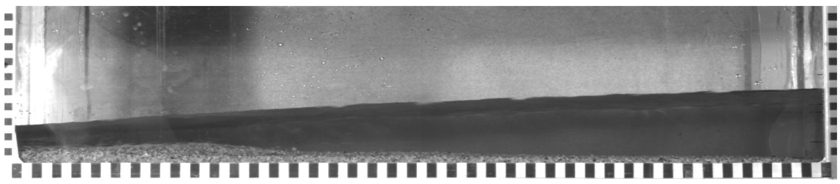

Figure 2.12: Detection of flow and first humps formation from the experimental image of sediment front (run# 2) at 30 s

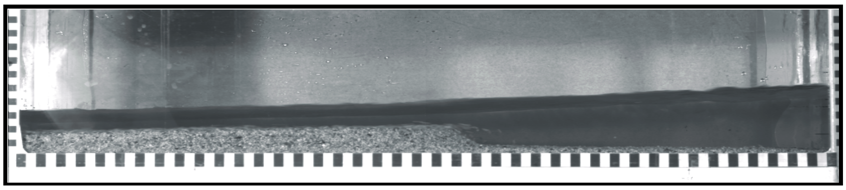

Figure 2.13: Typical image of hydraulic jump and sediment front (run# 2) at 95 s

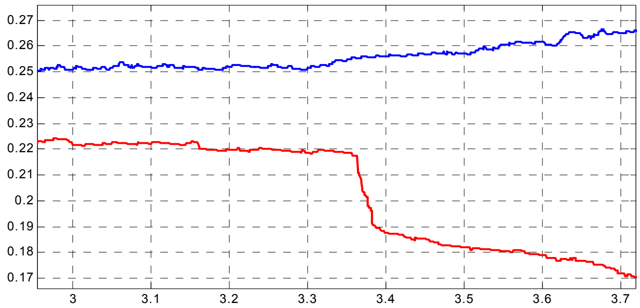

Figure 2.14: Detection of flow and bed interfaces from the experimental image of sediment front run# 2 at 95s

2.4. Material properties

The experimental set-up allows experiments to be conducted with various sediment materials. We have decided to use uniform sediment furnished at a constant rate (Table 2.2). To determine the main characteristics of the selected sediment, a sample of 800 g has been initially analysed in the laboratory according to the standard NBN-B11-013. The cumulative size distribution curve is presented in Fig. 2.15. In order to eliminate the finer particles and to have uniform sediment, the total amount of sediment of 4000kg has been sieved. A new sample of 800 g of the sieved sediment has been analysed again. The new cumulative size distribution curve (Fig. 2.15) shows that particles finer than 0.5mm were removed. Thus, the used material has the following characteristics:

Non-cohesive, uniform coarse sand of mean grain diameter d_m = 1.65mm, sediment porosity ε_0 = 0.42 and 2.633 as specific weight; with a gradation coefficient σ_g= 1.25 in conformity with the uniformity criteria of Raudkivi.

$$\sigma_g = \sqrt{\frac{d_{84}}{d_{16}}} = 1.25 < 1.35 \qquad (2.6)$$

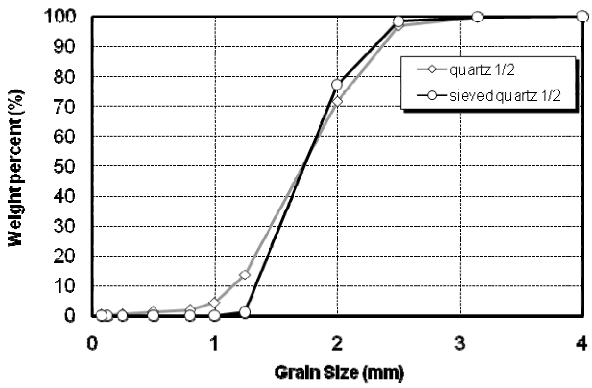

Figure 2.15: Grain size distribution of the used sediment quartz ½ before and after sieving

The main characteristics of the used sediment are summarised below in Table 2.3.

Sediment characteristics	
median diameter d_{50} (mm)	1.65
d_{16} (mm)	1.4
d_{84} (mm)	2.2
d_{90} (mm)	2.35
density ρ_s	2.633
Porosity ε_0	0.42

Table 2.3: Sediment characteristics

2.5. Tests configurations

In the frame of this thesis several tests has been conducted under various hydraulic, sediment parameters and initial conditions. The various initial conditions are obtained by adjusting the sediment bed profile at desired slope. A relatively flat bed of sediment is obtained by first pouring sediments in surplus, without compacting them, and profiling them at wanted profile by passing with a scrapper plate along the channel to gradually eliminate layers of excess sediments. Water is then added carefully and gradually to the desired level, at small rate to guarantee that the bed is fully saturated. Level regulation at the downstream end of the channel is achieved by inserting steel plates of 5 cm height. A first 5 cm-high steel plate is used to fix the initial height of the sediment bed. Overflow is conveyed into a settling tank.

a-Aggradation and degradation

The configuration corresponding to the aggradation (Fig. 2.16) or degradation (Fig. 2.17) in fully supercritical flow consists in: (a) initial steep sloped bed,(b) a critical depth in the upstream boundary of the channel where sediment flux and liquid discharge are imposed and (c) a fixed bed level in the downstream boundary.

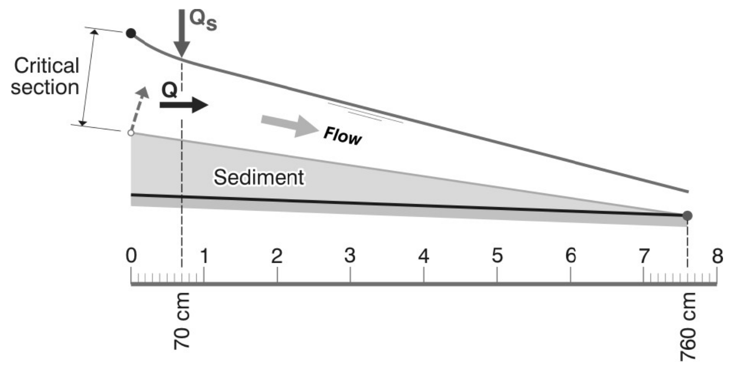

Figure 2.16: Initial experimental aggradation configurations

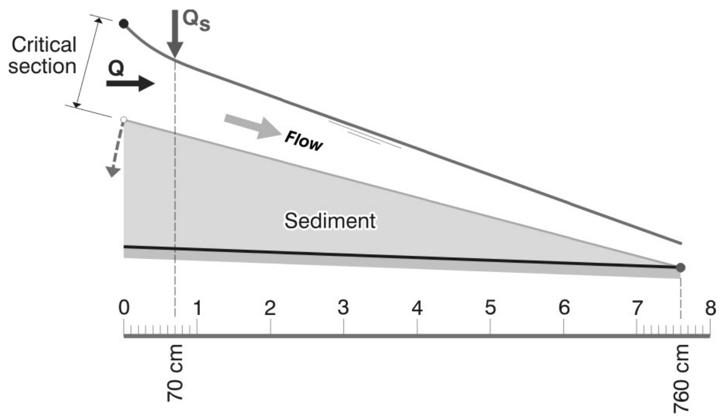

Figure 2.17: Initial experimental degradation configurations

b-Knickpoint migration

The initial make-up of knickpoint consists in a breaking of the bed slope at the knickpoint position with a mild slope upstream of the knickpoint yielding subcritical flow and a steep slope downstream of the knickpoint resulting in a supercritical flow (Fig. 2.18).

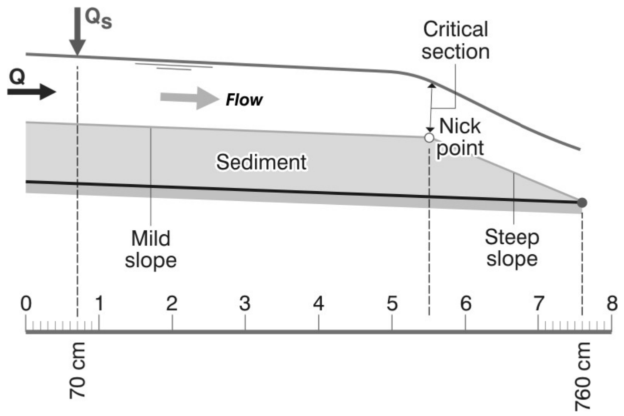

Figure 2.18: Initial experimental knickpoint migration configuration

c-Hydraulic jump and sediment front

We consider a steep-sloped channel of finite length initially in equilibrium, with constant water and sediment discharges and a uniform bed profile (Fig. 2.19). At a reference time $t = 0$, a subcritical condition is imposed downstream by raising the water level by closing of downstream gate.

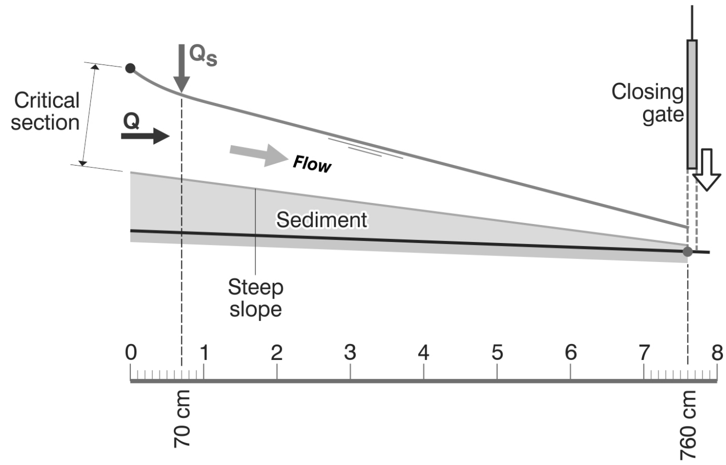

Figure 2.19: Initial experimental sediment front configurations

Chapter 3

Mathematical analysis of governing equations and derivation of general mathematical structure of morphodynamics diffusion model

3.1 Introduction

In order to deal mathematically with the boundary conditions in super- and transcritical flows over mobile bed, it is important to recall the classical approach to the eigenvalues analysis of the Saint-Venant-Exner equations as performed by (Abbott, 1966, Janssen, 1978 and Zech 1996) . The results of such analysis allows to understand the propagation of disturbance in mobile bed and flow surface. The evolution of theses disturbances is depending on the flow regime itself. The behaviour of the disturbances propagation in the case of near critical flows, as identified by Seiben (1997 and 1999) between $0.8 < Fr < 1.2$, is of significance for the present work. For better illustration, a simple (compared to the complex numerical models) and accurate analytical approximation of those eigenvalues is recalled (Goutière and Laraichi, 2006).

The next mathematical analysis consists in derivation of a linear diffusion model from the Exner equation. The resolution of this equation in a fixed domain using the accurate boundary conditions provides easily the analytical solutions corresponding for example to aggradation or degradation in supercritical flow. For moving boundary situations like knickpoint migration with the presence of control section and sediment front propagation with the presence of hydraulic jump, the problem is more complex, thus special solutions are needed. For this reason a general mathematical structure is developed in the present chapter.

3.2. Governing equations

Generally, the mathematical modelling of unsteady sediment-transporting flows relies on a system of three equations: two (Saint-Venant or shallow-water equations) describing flow continuity and momentum conservation with shallow-water assumptions, and one (Exner equation) expressing the sediment continuity (Zech, 1996).

Flow continuity

$$\frac{\partial A}{\partial t}+\frac{\partial A_0}{\partial t}+\frac{\partial Q}{\partial x}=0 \tag{3.1a}$$

Sediment continuity

$$\frac{\partial (A\hat{C})}{\partial t}+(1-\varepsilon_0)\frac{\partial A_0}{\partial t}+\frac{\partial Q_s}{\partial x}=0 \tag{3.1b}$$

Momentum balance

$$\frac{\partial Q}{\partial t}+\frac{\partial}{\partial x}(\beta\frac{Q^2}{A})+gA\frac{\partial h}{\partial x}+gA\frac{\partial z_{b0}}{\partial x}+gAS_f=0 \tag{3.1c}$$

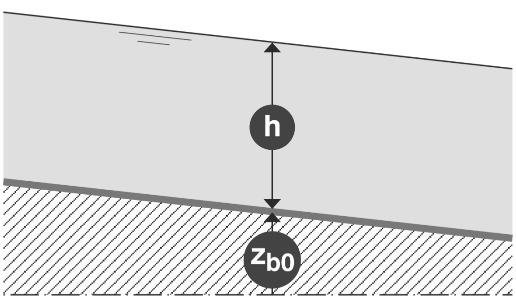

Fig 3.1a: longitudinal profile

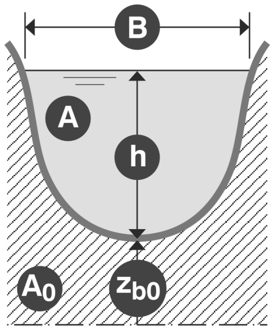

Fig 3.1b: Cross section

The parameters in the equations above have the following signification: Q is mixture discharge, Q_S is total load (bed load and suspension load), A cross section corresponding to the transport area, A_0 a conventional area comprised between the river bed and an arbitrary reference level defined on the width B

of the free surface, h local water depth in the cross section in movement, z_{b0} is the bed level computed from a reference level, $\hat{C}$ is the mean volumetric concentration of the sediment in the mixture (on A) and defined as $\hat{C} = \frac{1}{A}\int_A c dA$
where c is a local concentration of sediment. S_f energy slope per unit width, ε_0 is the bed porosity, ß is the coefficient of distribution of quadratic velocity (Boussinesq).

Where the friction slope S_f in (3.1c) may be calculated using the Manning-Strickler equation

$$S_f = n \frac{u}{R_h^{2/3}} \tag{3.2}$$

and the sediment discharge is estimated by Meyer-Peter and Müller relation

$$q_s = 8\sqrt{g\,(s-1)\,d_{50}^{\;3}}\left(\left(\frac{n_b^{'}}{n_b}\right)\frac{R_b\,S_f}{(s-1)\,d_{50}} - 0.047\right)^{3/2} \tag{3.3}$$

Where q_s is the solid discharge per unit width, R_b is the hydraulic radius related to the bed, s = ρ_s/ρ is the grain specific density, ρ_s and ρ being the volumetric mass of grain and water, respectively, $n_b = n_b^{'} + n_b^{''}$ is the global Manning roughness coefficient of the bed, taking into account the roughness proper to the sediments $n_b^{'} = d_{90}^{1/6}/26$ and the roughness related to bedforms $n_b^{''}$. Then the ratio n_b'/n_b is the roughness correction parameter to be taken equal to 1 when no bedforms are considered. For the evaluation of roughness and the tractive force, the wall effect is taken into consideration according to Einstein's assumption.

3.3 Eigenvalues analysis and boundary conditions

The governing equations of shallow flows are hyperbolic. The hyperbolicity of these equations implies they are physically based on the propagation of information. The celerities of the information are represented by the eigenvalues, calculated from the determinant of the coefficients matrix of the equations system and have to be real. The information is moving along characteristics curves in the plane (x, t), (Abbott, 1979) as illustrated in Figure 3.2 which shows respectively the domain of influence of a perturbation and the domain of dependence of a situation, depending on the characteristic curves.

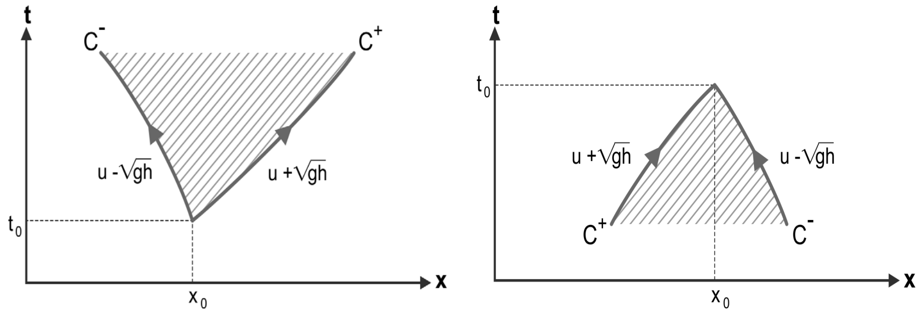

Figure 3.2: Influenced and dependent domain (subcritical regime)

3.3.1 Method of partial derivatives

The equations for sediment-loaded flow slightly differ from those for clear-water flow. To analyse the differences between these types of equations, we refer to previous works of Vreugdenhil and de Vries (1967), who proposed the first eigenvalues analysis of the Saint-Venant – Exner equations, Among several researchers: Jansen et al. (1979); Sloff (1992); Zech (1994, 1996) and Sieben (1999). The behaviour of these equations, in case of near- critical flows, was studied by Lyn and Altinakar (2002), Goutière and Laraichi

(2006), Savary (2007), Goutière et al. (2008). Vreugdenhil and de Vries (1967) have used the characteristics celerities of the hyperbolic system of the governing equations (3.1) to show the impact of the upstream and downstream boundary conditions on the morphodynamic evolution of rivers.

The analysis is given here for a wide rectangular channel, which implies that a unit width can be considered. Thus the governing equations can be rewritten as follows:

$$\frac{\partial h}{\partial t}+\frac{\partial z_b}{\partial t}+\frac{\partial q}{\partial x}=0\,, \tag{3.4a}$$

$$\frac{\partial (h\hat{C})}{\partial t}+(1-\varepsilon_0)\frac{\partial z_b}{\partial t}+\frac{\partial q_s}{\partial x}=0\,, \tag{3.4b}$$

$$\frac{\partial q}{\partial t}+\frac{\partial}{\partial x}\left(\frac{q^2}{h}\right)+g\,h\frac{\partial h}{\partial x}+g\,h\frac{\partial z_b}{\partial x}+g\,h\,S_f=0 \tag{3.4c}$$

where $q = h\,u$ and q_s are the mixture and solid discharge per unit width, u the mean velocity, $\hat{C}$ the sediment concentration assumed equal to q/q_s, ε_0 the porosity, z_b and h the bed level and the water depth respectively, and S_f is the energy slope.

The momentum equation (3.4c) can be rewritten by replacing $q = h\,u$, developing the derivatives and subtracting (3.4a):

$$\frac{\partial u}{\partial t}-\frac{u}{h}\frac{\partial z_b}{\partial t}+u\frac{\partial u}{\partial x}+g\frac{\partial h}{\partial x}+g\frac{\partial z_b}{\partial x}+g\,S_f=0 \tag{3.5}$$

An analysis of the system is possible subject to some simplifications: the variation of bed level z_b according to the time is neglected in (3.4a) and in (3.5) and also the first term in (3.4b). Assuming that the solid discharge is a function of the velocity u and the water depth h, and since the total differentials du, dh and dz_b also hold, a system of six partial differential equations is obtained (Jansen et al., 1979)

$$\begin{pmatrix} 1 & u & 0 & g & 0 & g \\ 0 & h & 1 & u & 0 & 0 \\ 0 & \dfrac{\partial q_s}{\partial u} & 0 & \dfrac{\partial q_s}{\partial h} & 1-\varepsilon_0 & 0 \\ dt & dx & 0 & 0 & 0 & 0 \\ 0 & 0 & dt & dx & 0 & 0 \\ 0 & 0 & 0 & 0 & dt & dx \end{pmatrix} \times \begin{pmatrix} \dfrac{\partial u}{\partial t} \\ \dfrac{\partial u}{\partial x} \\ \dfrac{\partial h}{\partial t} \\ \dfrac{\partial h}{\partial x} \\ \dfrac{\partial z_b}{\partial t} \\ \dfrac{\partial z_b}{\partial x} \end{pmatrix} = \begin{pmatrix} -gS_f \\ 0 \\ 0 \\ du \\ dh \\ dz_b \end{pmatrix} \tag{3.6}$$

The method of characteristics consists in generating fictitiously a small perturbation (first order discontinuity) in the system. These perturbations are like an infinitesimal wave, which travels with a finite speed. This means that the information path can be identified and followed in the plane (*x-t)*. Such information path is called a characteristic, which allows materializing the travel of the information (initial conditions and boundary conditions) in the problem. In such discontinuities, the partial derivatives are indeterminate which implies that the characteristic polynomial associated with the matrix of coefficients in (3.6) must vanish along the path of such discontinuities. Thus the condition determining the characteristic velocities *c=dx/dt* with $dt \neq 0$ is that the determinant of the matrix coefficients (3.6) be zero, which reads

$$dx^3[-(1-\varepsilon_0)] + dx^2 dt[2u(1-\varepsilon_0)]$$
$$+dxdt^2\left[\left(gh-u^2\right)(1-\varepsilon_0)+g\frac{\partial q_s}{\partial u}\right]+dt^3\left[gh\frac{\partial q_s}{\partial h}-gu\frac{\partial q_s}{\partial u}\right]=0 \tag{3.7}$$

and can be rewritten in the following form after dividing the different terms by (1-ε_0)and dx^3, and changing the sign:

$$a_0\left(\frac{dx}{dt}\right)^3 + a_1\left(\frac{dx}{dt}\right)^2 + a_2\left(\frac{dx}{dt}\right) + a_3 = 0 \tag{3.8}$$

with the subsequent coefficients values:

$$a_0 = 1, a_1 = -2u, a_2 = \left(u^2 - gh\right) - g\frac{\partial}{\partial u}\left(\frac{q_s}{1-\varepsilon_0}\right) \qquad (3.9a\text{-}c)$$

$$a_3 = gu\frac{\partial}{\partial u}\left(\frac{q_s}{1-\varepsilon_0}\right) - gh\frac{\partial}{\partial h}\left(\frac{q_s}{1-\varepsilon_0}\right) \qquad (3.9d)$$

3.3.1.1 Eigenvalues analysis with sediment transport situation

The roots of the determinant (3.8) related to matrix coefficients (3.6) are the three eigenvalues C_i ($i = 1 \ldots 3$). These roots should be theoretically calculable but their analytical expression is so complex that it is not exploitable in practice (Lyn, 1987; Lyn and Altinakar, 2002). To provide an example of those celerities, the following case corresponding to a wide channel was analyzed (Zech, 1996), Savary (2007). The used data are inspired by Rahuel (1988) and they concern an idealized stream of Rhône river: a unit water discharge $q = 16$ m^3/s/m, presenting a uniform flow in a channel with mobile bed (roughness n = 0.027778, grain diameter $d_{50} = 0.0274$ m, $\rho_s = 2650$kg/m^3). The flow is assumed to be uniform and steady for bed slope varying from 0.0001 up to 0.0400. Solid discharge is calculated using Meyer-Peter-Muller formula (Meyer-Peter and Muller, 1948) and the derivatives of the solid discharge $\partial q_s / \partial h$ and $\partial q_s / \partial u$ are computed analytically.

The resulting three celerities are plotted in Figure 3.3 as a function of the Froude number. Two celerities (C_1 and C_2) are always positive and the third one (C_3) is always negative for all values of Froude number.

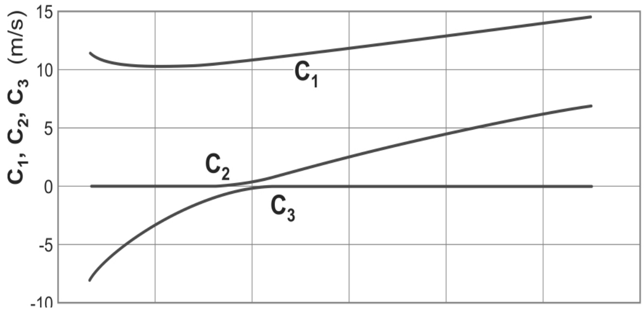

Figure 3.3: Eigenvalues vs Froude

The celerity that is small with respect to the others (C_2 for subcritical flows and C_3 for supercritical flows) is related to the sediments and corresponds to morphodynamic disturbances.

Relations (3.10 a and b) associated with Figures 3.4 below constitute a guide for the specification of boundary conditions. For subcritical flows (Figure 3.4 a), a hydrodynamic condition has to be imposed at the upstream end (e.g. a discharge) and at the downstream end of the channel (e.g. a water depth), while the morphological condition has to be set at the upstream end (e.g. a prescribed bed level). For supercritical flow (Figure 3.4 b), two hydrodynamic conditions are to be provided at the upstream end of the channel C_1 and C_2 (e.g. a discharge and a water depth) with a morphological condition imposed downstream C_3 (e.g. a prescribed bed level).

(a) subcritical flow

$$U < \sqrt{gh} \Rightarrow \begin{cases} C_1 > 0 \\ C_2 > 0 (C_2 \approx 0) \\ C_3 < 0 \end{cases} \quad (3.10a)$$

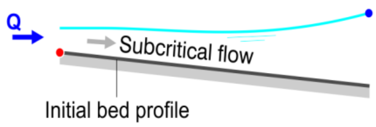

Signs of celerities of characteristics in subcritical flow

Figure 3.4 a: Boundary conditions in subcritrical flow

(b) supercritical flow

$$U > \sqrt{gh} \Rightarrow \begin{cases} C_1 > 0 \\ C_2 > 0 \\ C_3 < 0 (C_3 \approx 0 \end{cases} \qquad (3.10b)$$

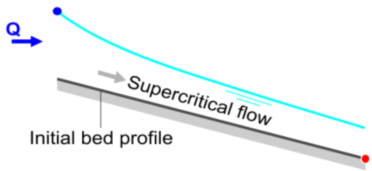

Signs of celerities of characteristics in supercritical flow

Figure 3.4 b: Boundary conditionsin supercritical flow

The break of the *physical* continuity of the characteristics celerities C_2 and C_3 respectively hydraulic and sediment characteristics celerities, in spite of their mathematical continuity illustrates that the transition between sub-and supercritical flow is an appealing aspect. In a pure hydrodynamic problem without sediment transport, this transition corresponds to a control section (from subcritical to supercritical flow) and one of the celerity is equal to zero. In the presence of sediment transport, this transition is still ambiguous, none of the celerity is equal to zero. What becomes the critical section corresponding to Fr = 1? Does a critical section proper to sediment transport or to the mixture (water and sediments) exists? These questions are challenging and show the interest to study transcritical and near critical flows over mobile beds as illustrated in Figures 3.5 a and b.

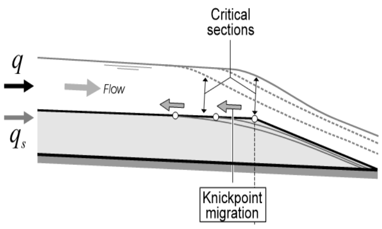

Figure 3.5a: Knickpoint and control section

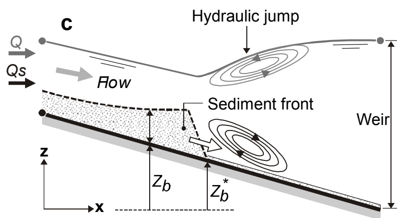

Fig 3.5b: Hydraulic jump and sediment front

3.3.1.2 Eigenvalue analysis without sediment transport situation

To illustrate the eigenvalue approach in a simple case of pure hydrodynamic without sediment transport $q_s = 0$ (fixed bed, or mobile bed with transport capacity below the transport threshold), we consider the coefficient $a_3 = 0$ from (3.9d). The equation (3.8) can be reduced to second-order equation

$$\left(\frac{dx}{dt}\right)^2 - 2u\left(\frac{dx}{dt}\right) + \left(u^2 - gh\right) = 0 \qquad (3.11)$$

which assumes that one root of the equation (3.7) is equal to 0. The three roots of the equation (3.7) are: two roots of equation (3.11) and one root null

$$C_1 = u + \sqrt{gh} \quad C_2 = u - \sqrt{gh}\,,\ C_3 \approx 0 \qquad (3.12\text{a-c})$$

The roots c_1 and c_2 are the hydrodynamic celerities of characteristics. According to the value of the velocity u, we can distinguish the following possible cases:

Subcritical flow

$$u < \sqrt{gh} \Rightarrow \begin{cases} C_1 > 0 \\ C_2 < 0 \end{cases} \qquad (3.13)$$

The information can propagate downward (typically liquid discharge) or propagate upward (water level, for example)

Supercritical flow

$$u > \sqrt{gh} \Rightarrow \begin{cases} C_1 > 0 \\ C_2 > 0 \end{cases} \qquad (3.14)$$

The information can only propagate downward (for example liquid discharge and water) level.

3.4 Analytical expressions of the Eigenvalues of the Saint-Venant – Exner equations

In the case where the solid discharge $q_s = 0$ (fixed bed, or mobile bed below the transport threshold), the celerities turn out to be $C_{H1} = u + c$ and $C_{H2} = u - c$,(subscript H for hydrodynamic), they are compared to three eigenvalues taking into consideration the presence of sediments Fig 3.6.

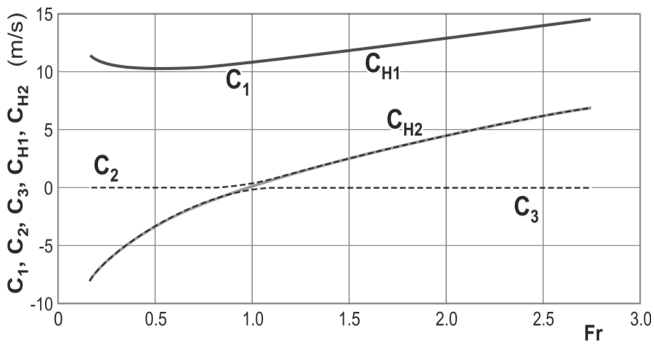

Figure.3.5:. Eigenvalues vs Froude number with and without sediments (Goutière et al., 2008)

A new approximate and usable analytical expression has been derived lately (Goutière and Laraichi, 2006; Goutière et al., 2008) by using the properties of cubic polynomials $\alpha x^3 + \beta x^2 + \gamma x + \delta = 0$ whose the roots x_1, x_2 and x_3 are associated together by the following relations:

$$x_1 + x_2 + x_3 = -\frac{\beta}{\alpha} \; , \; x_1 x_2 + x_2 x_3 + x_3 x_1 = \frac{\gamma}{\alpha} \; , \text{ and } \; x_1 x_2 x_3 = -\frac{\delta}{\alpha} \qquad (3.15a\text{-}c)$$

Applying (3.15a) to the characteristic polynomial (3.8) with the coefficients (3.9a-c) results in

$$C_1 + C_2 + C_3 = -a_1 = 2\frac{q}{h} = 2u \qquad (3.16)$$

seeing that the effect of sediments is considered to be an insignificant perturbation on the characteristic equations, it can be assumed that the main eigenvalue is not influenced by the presence of sediments (Lyn and Altinakar, 2002). Under the assumption, inspired from (Figures 3.6 and 3.7), $C_1 = C_{H1}$ and $C_2 + C_3 = C_{H2}$, it was possible to develop an approached analytical expression of the eigenvalues of the Saint-Venant–Exner equations (Goutière and Laraichi, 2006).

The eigenvalue C_1 appears to be unchanged by the presence of sediment, as the relative difference between C_1 and C_{H1} is very small Fig.3.7. The subscript H denotes the hydrodynamic value.

$$\delta_{1H} = \frac{C_1 - C_{H1}}{C_1} \tag{3.17}$$

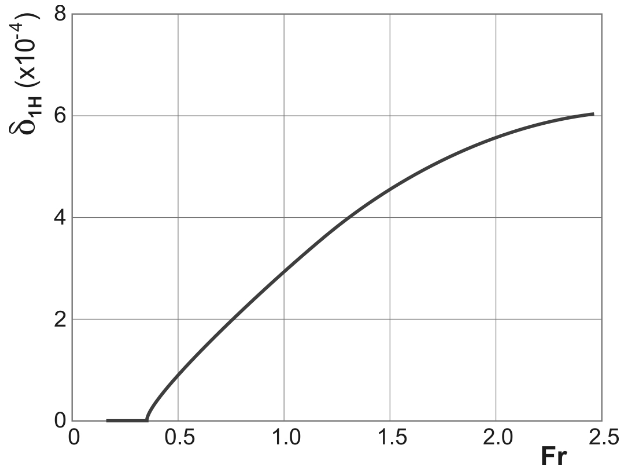

Figure 3.7: Relative difference δ_{1H} between C_1 and C_{1H} from (Goutière et al., 2008)

$$C_1 = C_{H1} = u + c \tag{3.18}$$

For each Froude number, the second hydrodynamic eigenvalue is decomposed into two parts when sediments are present, giving C_2 and C_3, the sum $C_2 + C_3$ is close to C_{H2}. The relative difference is represented in Figure 3.8.

$$\delta_{2\mathrm{H}} = \frac{(C_2+C_3)-C_{\mathrm{H2}}}{(C_2+C_3)} \tag{3.19}$$

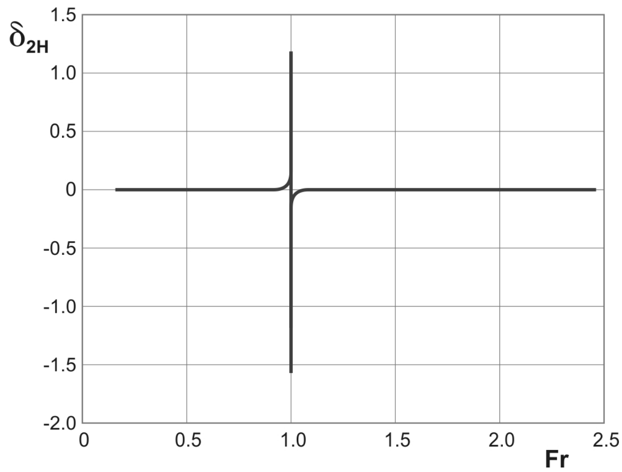

Figure.3.8: Relative difference δ_{2H} between ($C_2 + C_3$) and C_{H2} from (Savary, 2007)

$$C_2 + C_3 = (C_1 + C_2 + C_3) - C_1 = 2u - (u + c) = u - c = C_{\mathrm{H2}} \tag{3.20}$$

Consequently, since C_1 does not account for sediment effects, this effect is only applied to C_2 and C_3, under the form of a symmetrical deviation from $C_{H2} = u - c$. Then, applying (3.20) in (3.15c) leads to

$$C_1\, C_2\, C_3 = C_{\mathrm{H1}}\, C_2\,(C_{\mathrm{H2}} - C_2) = (u+c)C_2\,(u - c - C_2) = \\ -a_3 = \frac{gh}{1-\varepsilon_0}\frac{\partial q_s}{\partial h} - \frac{gu}{1-\varepsilon_0}\frac{\partial q_s}{\partial u} \tag{3.21}$$

which yields in quadratic polynomials in C_2, whose roots give C_2 and consequently also C_3,

$$C_{1\mathrm{A}} = u + c, \tag{3.22a}$$

$$C_{2\mathrm{A}} = \frac{1}{2}\left(u - c + \sqrt{(u-c)^2 + 4\frac{1}{(u+c)}\frac{g}{(1-\varepsilon_0)}\left(u\frac{\partial q_s}{\partial u} - h\frac{\partial q_s}{\partial h}\right)}\right) \tag{3.22b}$$

$$C_{3\mathrm{A}} = \frac{1}{2}\left(u - c - \sqrt{(u-c)^2 + 4\frac{1}{(u+c)}\frac{g}{(1-\varepsilon_0)}\left(u\frac{\partial q_s}{\partial u} - h\frac{\partial q_s}{\partial h}\right)}\right) \tag{3.22c}$$

in such a way that the three eigenvalues may be written in non-dimensional form as

$$\frac{C_1}{u} \cong \left(1 + \frac{1}{Fr}\right) \tag{3.23a}$$

$$\frac{C_{2,3}}{u} \cong \frac{1}{2}\left[\left(1 - \frac{1}{Fr}\right) \pm \sqrt{\left(1 - \frac{1}{Fr}\right)^2 + \frac{4}{(Fr^2 + Fr)}(\chi_2 - \chi_1)}\right] \tag{3.23b,c}$$

with $Fr = u/c$ is the Froude number and χ_1 and χ_2 are non-dimensional factors associated to the sediment discharge

$$\chi_1 = \frac{1}{(1-\varepsilon_0)u}\frac{\partial q_s}{\partial h},\ \chi_2 = \frac{1}{(1-\varepsilon_0)h}\frac{\partial q_s}{\partial h} \tag{3.24a,b}$$

The relative differences between the approached analytical expressions of the eigenvalues $C_{i\mathrm{A}}$ developed by Laurent Goutière (Goutière et al., 2008) and the exact values C_i computed numerically Savary (2007) are plotted in Figure 3.9. Their relative differences confirm that the analytical expressions are a good approximations.

$$\delta_1 = \frac{C_1 - C_{1\mathrm{A}}}{C_1} \qquad \delta_2 = \frac{C_2 - C_{2\mathrm{A}}}{C_2} \qquad \delta_3 = \frac{C_3 - C_{3\mathrm{A}}}{C_3} \tag{3.25a-c}$$

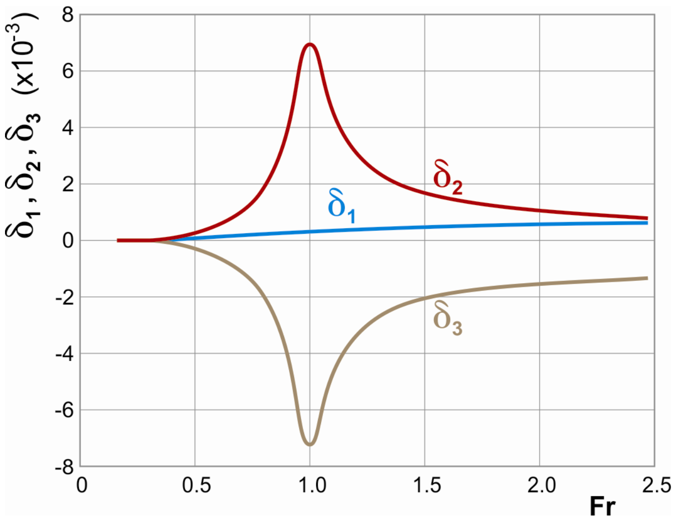

Figure.3.9: Relative difference between approached analytical eigenvalues and exact eigenvalues (δ_1, δ_2, δ_3) from Goutière et al. (2008) and Savary (2007)

Lyn and Altinakar (2002) give distinct expressions for the region far from the critical conditions and close to them. On the opposite the new expressions of Goutière et al. (2008) cover the whole range of Froude numbers with good accuracy.

3.5 Diffusion model in fluvial morphodynamics

3.5.1 Introduction

Mathematical solutions are obtained for several sedimentary problems featuring finite and semi-infinite alluvial channels evolving under a diffusional sediment transport. Fixed boundaries for aggraded or degraded steep sloped river beds and moving boundaries linked to transcritical flow are considered at one end of the channels. Two main cases are considered essentially because they are in the foremost line of this thesis: prograding deltas or sediment front advancing into a body of standing water (check dam, lake or sea) and the erosion and knickpoint migration.

The idealized formulations of all three problems are based on the diffusion equation and admit exact solutions: Green functions or Fourier series for fixed boundary problems. At the moving boundary, compatibility conditions are imposed depending on the specific case and then self-similarity solutions can be derived. This analytical solution captures both the motion of the boundary and the time evolution of the longitudinal channel profile.

In fact, we aim to show in this chapter that the moving boundary problems illustrated in Figure 3.5 share the same mathematical structure. In a rather natural way, their initial and boundary conditions can be made to satisfy a scaling symmetry of the diffusion equation. This in turn leads to the existence of self-similar alluvial profiles, evolving in time without changing their shapes. Exact solutions can then be worked out analytically. The approach adopted for this purpose draws upon the work of Voller et al. (2004), who recently exploited the same symmetry to solve a related problem: the progradation of a fluvial delta starting from a channel of zero length (the prograding delta starts in the body of standing water at the interface position x = 0) Figure 3.10b. Our objective is to extend the approach to semi-infinite channels, and use it to treat other problems of geomorphological interest.

3.5.2 Linear diffusion equation

If one considers that the flow is everywhere close to the steady uniform regime defined by the local bed gradient ($S_f = S_w = S_0 = S = -\partial z_b / \partial x$). This constitutes a good approximation when the Froude number is away from unity (Capart et al., 1998). A result of the above quasi-uniform assumption is that the solid discharge becomes a function of the local bed slope only

$$h = \mathrm{f}(q, S) \tag{3.26}$$

$$q_s = \mathrm{f}(q, h) = \mathrm{f}(q, S) \tag{3.27}$$

For q known and constant along x ($\partial q/\partial x = 0$):

$$q_s = \mathrm{f}(S) \tag{3.28}$$

Using, for instance, Meyer-Peter–Müller (3.3) in the following non-dimensional form:

$$\frac{q_s}{\sqrt{g\,(s-1)\,{d_{50}}^3}}=8\left(\frac{h\,S}{(s-1)\,d_{50}}-\tau_{*c}\right)^{3/2} \tag{3.29}$$

Where τ_{*c} is a non-dimensional critical bed shear stress. The Manning formula (3.2) could be replaced in the subsequent mathematical developments by Chézy relation for uniform flow:

$$q=C\ h^{3/2}\,S^{1/2} \tag{3.30}$$

$$h=\frac{q^{2/3}}{C^{2/3}\,S^{1/3}} \tag{3.31}$$

the solid discharge writes, with the threshold value τ_{*c} neglected:

$$\frac{q_s}{\sqrt{g\,(s-1)\,d^3}}=8\left(\frac{q^{2/3}\,S^{2/3}}{C^{2/3}\,(s-1)\,d}-\tau_{*c}\right)^{3/2}\cong\frac{8\,q}{C\,(s-1)^{3/2}\,d^{3/2}}\,S \tag{3.32}$$

$$q_s=\frac{8\sqrt{g}\ q}{C\,(s-1)}\,S=-\frac{8\sqrt{g}\ q}{C\,(s-1)}\,\frac{\partial\,z_b}{\partial x} \tag{3.33}$$

So, using (3.33) and assuming that the discharge q is constant along x ($\partial q/\partial x = 0$), Exner equation (3.4b) may write

$$\frac{\partial z_b}{\partial t}=-\frac{1}{1\text{-}\varepsilon}\,\frac{\partial q_s}{\partial x}=-\frac{1}{1\text{-}\varepsilon_0}\,\frac{\partial}{\partial x}\left(-\frac{8\sqrt{g}\ q}{C\,(s-1)}\,\frac{\partial\,z_b}{\partial x}\right)=D\,\frac{\partial^2\,z_b}{\partial x^2} \qquad (3.34$$

With
$$D=\frac{1}{1-\varepsilon_0}\,\frac{8\sqrt{g}}{C\,(s-1)}\,q \tag{3.35}$$

D is a constant diffusion coefficient proportional to the water discharge per unit width. Equation (3.34) is standard and applies to many problems in heat flow and solute transport. In the context of fluvial morphodynamics, it expresses conservation of sediment mass.

The general relation expressing the sediment transport is linearised around an equilibrium transport where $S = S^{\infty}$. As the sediment discharge converges everywhere towards this value, we can write:

$$q_s\left(x,t\right)=q_s^{\infty}+\left(\frac{\partial q_s}{\partial S}\right)_{q=\mathrm{cst}}\left[S\left(x,t\right)-S^{\infty}\right]+\ldots \tag{3.36}$$

Introducing (3.36) in (3.4b) without its first term, yields

$$\frac{\partial z_b}{\partial t}=-\frac{1}{1-\varepsilon_0}\frac{\partial q_s}{\partial x}=-\frac{1}{1-\varepsilon_0}\left[\left(\frac{\partial q_s}{\partial S}\right)_{q=\mathrm{cst}}\frac{\partial S}{\partial x}\right]=\left(\frac{1}{1-\varepsilon_0}\left(\frac{\partial q_s}{\partial S}\right)_{q=\mathrm{cst}}\right)\frac{\partial^2 z_b}{\partial x^2} \tag{3.37}$$

equivalent to (3.34-3.35), if the above assumptions are made.

Equation (3.34) constitutes a linear diffusion equation and has been used as a morphodynamic model by de Vries (1973). In the present thesis, the solution of this equation is provided for both fixed boundary problems and moving boundary problems.

In order to re-introduce the threshold concept, it is possible, according to Hsu and Capart (2008) to write (10) on the approximate following form:

$$\frac{q_s}{\sqrt{g\left(s-1\right)d^3}}=8\left(\frac{q^{2/3}}{C^{2/3}\left(s-1\right)d}\left(S^{2/3}-S_{\min}^{2/3}\right)\right)^{3/2}\cong\frac{8q}{C\left(s-1\right)^{3/2}d^{3/2}}\left(S-S_{\min}\right) \tag{3.38}$$

leading to a kind of generalisation of (3.33):

$$\begin{aligned} q_s &= \max\left[\frac{8\sqrt{g}\,q}{C\left(s-1\right)}\left(S-S_{\min}\right),0\right] \\ &= \max\left[\frac{8\sqrt{g}\,q}{C\left(s-1\right)}\left(-\frac{\partial z_b}{\partial x}-S_{\min}\right),0\right] \end{aligned} \tag{3.39}$$

where Smin is the minimum slope required for sediment transport. This latter expression leads to the same diffusion equation as (3.34) as far as $S > S_{\min}$. This latter bed slope can be determined from the calibration of the sediment transport relationship Fig. 3.10.

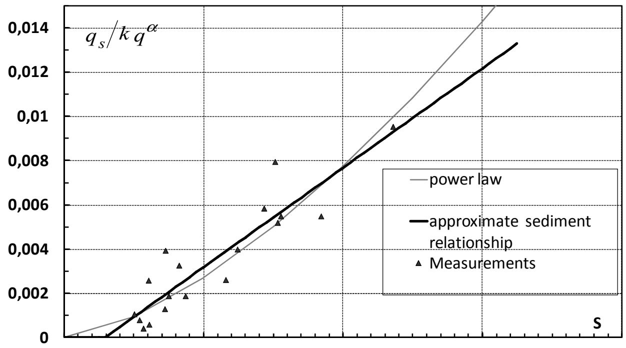

Figure 3.10: Calibrated sediment transport relationship from experimental data (S_{min}= 0.01)

a-Fixed boundaries problems

For fixed boundaries s_1 and s_2, the linear diffusion equation (3.34) is well-known to admit general solutions, typically constructed using Green functions or Fourier series by using the appropriate Dirichlet (upstream) and Neumann (downstream) boundary conditions. Such diffusion solutions over fixed domains have been applied to sedimentary processes and compared with experiments in Begin et al. (1981), Gill (1983) and in the present thesis. The equation is most simply derived by assuming steady water discharge, constant channel width, normal water flow, and sediment transport proportional to stream power.

b-Moving boundaries problems

This section focuses instead on moving boundary problems. The channel is bounded upstream and downstream by positions $x = s_1$ and $x = s_2$, either one of which can be sent to infinity for which one of the two positions can evolve over time. Coupling between the channel response and boundary motion makes the problem non-linear and general solutions can no longer be expected. For particular problems, however, special solutions can be derived by exploiting symmetries of the diffusion equation. Two known solutions of this kind are illustrated in Figures 3.11. Figure 3.11a shows the classical solution of Neumann (see Crank, 1984), originally derived for the ‘singlephase' Stefan problem in which conductive heat transfer in a liquid (water) drives the advance of a melting front into an isothermal solid (ice) at the melting temperature. The solution is displayed here for an evolving alluvial channel: sediment is supplied upstream of a lake of constant depth in such a way that the upstream bed level z_{b0} at position $x = 0$ is held constant. This leads to channel aggradation and to the advance of a delta into the standing water. The well-known exact solution to this problem has the similarity structure

$$z_b(x,t) = f(x/\xi(t))z_{b0}, \quad s_1 = 0 < x < s_2(t) = \lambda\xi(t) \tag{3.40}$$

where function $\xi(t)$ is an evolving length scale, function $f(\sigma)$ is a dimensionless function of dimensionless argument $\sigma = x/\xi(t)$, and λ is a dimensionless constant, all chosen to satisfy eq. (3.34) and its boundary conditions.

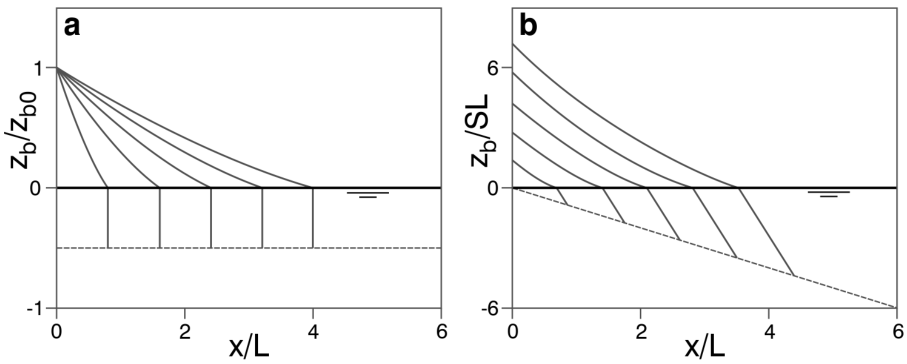

Figure 3.11: Two known similarity solutions for evolving shorelines: **a**) the classical Neumann solution (see e.g. Crank 1984), cast as a delta problem; **b**) the recent delta solution of Voller, Swenson and Paola (2004). Both solutions feature a fixed boundary condition at the origin and a moving boundary at the shoreline. Dashed lines show the initial lake bed; thin lines are snapshots of the alluvial profile for equally spaced values of the square root of the elapsed time $t^{1/2}$.

Recently, Voller et al. (2004) derived an analytical solution for a different problem illustrated in Figure 3.11b. Instead of a prescribed sediment level upstream of a lake of constant depth, they considered the case of a prescribed sediment influx upstream of a lake of linearly increasing depth. This problem is characterized by a different similarity structure

$$z_b(x,t) = f(x/\xi(t))\xi(t), \quad s_1 = 0 < x < s_2(t) = \lambda\xi(t) \qquad (3.41)$$

in which both the elevation z and the spatial coordinate x are normalized with respect to the evolving length scale $\xi(t)$. The resulting time sequence of self-similar profiles is obtained by simultaneously rescaling both the x and z coordinates, rather than just the x coordinate as in the classical Neumann solution.

The solution proposed by Voller et al. (2004) is of interest in its own right, both as a source of insights regarding shoreline dynamics and as a benchmark for the validation of numerical models. Its existence also suggests that other alluvial problems may be amenable to analytical treatment along the same lines. This is indeed the case, and we show in the present thesis that the approach can be extended to various problems involving semi-infinite channels. Before presenting specific solutions of geomorphic interest, the wider family to which they belong is first examined in the next section from a mathematical point of view.

Throughout this chapter, the water profile is approximated in the following manner. Over active alluvial reaches, the depth is assumed to coincide with the normal depth. As discussed in Paola (2000), this approximation applies when channels are examined over length scales large relative to the backwater length. As a further simplification, the normal depth is neglected compared to the typical height variations of interest. In regions of standing water, on the other hand, the water level is assumed horizontal. These idealizations are reasonable for large scale problems in steep sloped areas, reproducing the sharp contrast between steep, shallow channel flow and deep, nearly horizontal backwater zones. It may nevertheless lead to local errors in uplands, or even cause global discrepancies if applied to gently sloped lowlands. This idealization is highly useful because it effectively removes the water profile from the problem. Surface water is reduced to a diffusion agent (in active alluvial reaches) or to a boundary condition (at the edge of a body of standing water).

3.5.3 General self-similar structure

Following Voller et al. (2004), we focus on special solutions of the diffusion equation (3.34) having the self-similar structure. Commonly, self-similarity means that a given relation between space (x, z) and time t is conserved along time such that scaling x by the appropriate function of time delivers a relation with the same scaling for z as for x. A consequence is that along straight lines originating from $(x, z) = (0, 0)$, homothetic situations will be met; in particular, the slope $\partial z/\partial x$ will be conserved along those straight lines.

In the case of morphodynamics, the typical problem is the evolution of time of the river bottom profile (x, z_b). Both the bed elevation z_b and spatial coordinate x have to be normalized with respect to a length scale evolving in time:

$$\frac{z_b(x,t)}{\xi(t)} = \mathrm{f}\left(\frac{x}{\xi(t)}\right) = \mathrm{f}(\sigma) \tag{3.42}$$

where function $f(\sigma)$ expresses the shape of the profile as a function of dimensionless argument

$$\sigma = \frac{x}{\xi(t)} \tag{3.43}$$

and $\xi(t)$ is a function of time having dimension of length, which governs the space of the self-similar rescaling of the solutions. Substitution of a mathematical formulation (3.44)

$$z_b(x,t) = \mathrm{f}\left(\frac{x}{\xi(t)}\right)\xi(t) = \mathrm{f}(\sigma)\,\xi(t) \tag{3.44}$$

into the diffusion equation (3.34) implies, by mathematical analysis, $\xi(t)$ proportional to $\sqrt{Dt}$:

$$\xi(t) = \kappa\sqrt{Dt} = 2\sqrt{Dt} \tag{3.45}$$

where factor $\kappa = 2$ is introduced for convenience. The assumption (3.45) will be validated if it leads to an equation where the dependence on x and t is replaced by a dependence on σ only.

Both (3.42) and (3.43) can be constructed on dimensional grounds. From a mathematical point of view, they constitute a special case of the more general invariant solution (see e.g. Hydon 2000)

$$U(x,t) = t^{k/2} F(xt^{-1/2}) . \tag{3.46}$$

For any value of k (not necessarily equal to an integer), these are exact solutions describing the evolution of a scalar u subject to the dimensionless diffusion equation $\partial U / \partial t - \partial^2 U / \partial x^2 = 0$. Form (3.44) corresponds to $k = 1$, while the classical Neumann solution corresponds to $k = 0$.

In case where the bed profile presents a singularity (knickpoint or delta front) that moves in time, self-similarity relation (3.45) also holds for the singularity position that can be expressed by

$$s(t) = 2\,\lambda \sqrt{D\,t} \tag{3.47}$$

where λ is a scaling constant to be determined as a part of the solution. Self-similarity implies that the discontinuity is initially at the space origin $(x, z_b) = (0, 0)$, which is matched by (3.47).

Let us check if assumption (3.45) actually succeeds in replacing the diffusion equation (3.34) in x and t by an equation where only σ appears as variable. From (3.45) the time-derivative may be deduced:

$$\frac{\partial \xi}{\partial t} = 2\sqrt{D}\,\frac{1}{2}\,t^{-1/2} = \frac{2\,D}{2\sqrt{D\,t}} = \frac{2\,D}{\xi} \tag{3.48}$$

and from (3.44) and (3.48), with the definition (3.43):

$$\frac{\partial z_b}{\partial t} = \mathrm{f}(\sigma)\frac{\partial \xi}{\partial t} + \xi\,\mathrm{f}'(\sigma)\frac{\partial \sigma}{\partial t} = \mathrm{f}(\sigma)\frac{\partial \xi}{\partial t} - \mathrm{f}'(\sigma)\xi\,\frac{x}{\xi^2}\,\frac{\partial \xi}{\partial t} = \frac{2D}{\xi}\left[\mathrm{f}(\sigma) - \sigma\,\mathrm{f}'(\sigma)\right] \tag{3.49}$$

$$\frac{\partial z_b}{\partial x} = \xi\, f'(\sigma)\frac{\partial \sigma}{\partial x} = \xi\, f'(\sigma)\frac{1}{\xi} = f'(\sigma) \qquad (3.50)$$

$$\frac{\partial^2 z_b}{\partial x^2} = \frac{\partial}{\partial x}\left[f'(\sigma) \right] = f''(\sigma)\frac{\partial \sigma}{\partial x} = \frac{1}{\xi} f''(\sigma) \qquad (3.51)$$

where $f'(\sigma)$ and $f''(\sigma)$ are the first and second derivatives of the shape function $f(\sigma)$ according to σ.

Inserting (3.49) and (3.51) in the diffusion equation (3.34) leads to

$$\frac{\partial z_b}{\partial t} - D\,\frac{\partial^2 z_b}{\partial x^2} = \frac{2D}{\xi}\left[f(\sigma) - \sigma\, f'(\sigma) \right] - D\,\frac{1}{\xi} f''(\sigma) = 0 \qquad (3.52)$$

which reduces to the following ordinary differential equation (ODE):

$$f''(\sigma) + 2\,\sigma\, f'(\sigma) - 2\, f(\sigma) = 0 \qquad (3.53)$$

in which space x and time t do not appear separately anymore, so, validating assumption (3.45) as compatible with auto-similar solutions.

Equation (3.53) is a second-order ordinary differential equation (ODE) with non-constant coefficients. An obvious basis solution of (3.53) is

$$f_1(\sigma) = -\sigma \qquad (3.54)$$

where the minus sign is chosen for convenience. Reduction of order can be used to find the second basis solution. This must be of the form

$$f_2(\sigma) = f_1(\sigma)\, g(\sigma) = -\sigma\, g(\sigma) \qquad (3.55)$$

Such a form allows reducing the order of the differential equation. Indeed, introducing the derivatives

$$\begin{aligned} f_2(\sigma) &= -\sigma\, g \\ f_2'(\sigma) &= -\sigma\, g' - g \\ f_2''(\sigma) &= -\sigma\, g'' - 2\, g' \end{aligned} \qquad (3.56)$$

in (3.53) yields

$$-\sigma g''-2g'+2\sigma(-\sigma g'-g)+2\sigma g=0 \tag{3.57}$$

that reduces to first-order differential equation

$$\sigma g''+2\left(1+\sigma^2\right)g'=0 \tag{3.58}$$

Defining function h as

$$h=g' \tag{3.59}$$

equation (3.58) writes

$$\sigma\frac{\partial h}{\partial\sigma}+2\left(1+\sigma^2\right)h=0 \tag{3.60}$$

whose solution is found by separation of variables:

$$\frac{dh}{h}=-2\,\frac{1+\sigma^2}{\sigma}\,d\sigma=-2\,\frac{d\sigma}{\sigma}-2\,\sigma\,d\sigma \tag{3.61}$$

whose integral writes, with the last term as constant of integration

$$\ln h=-2\ln\sigma-\sigma^2+\ln(\alpha) \tag{3.62}$$

$$\ln(h)=\ln\left(\sigma^{-2}\right)+\ln\left(e^{-\sigma^2}\right)+\ln(\alpha) \tag{3.63}$$

$$h=\alpha\,\frac{e^{-\sigma^2}}{\sigma^2} \tag{3.64}$$

Integration by parts of (3.64) will yield function g (σ):

$$g=\int h\,d\sigma=\alpha\int e^{-\sigma^2}\,\frac{d\sigma}{\sigma^2}=\int u\,dv=u\,v-\int v\,du$$

$$=\alpha\left[e^{-\sigma^2}\left(-\frac{1}{\sigma}\right)-\int e^{-\sigma^2}\,(-2\sigma)\left(-\frac{1}{\sigma}\right)d\sigma\right]=\alpha\left[-\frac{e^{-\sigma^2}}{\sigma}-2\int e^{-\sigma^2}\,d\sigma\right]$$

$$(3.65)$$

So the second basis solution (3.55) becomes

$$f_2(\sigma) = -\sigma\, g = \alpha\left[e^{-\sigma^2} + \sqrt{\pi}\,\sigma\,\frac{2}{\sqrt{\pi}}\int e^{-\sigma^2}\,d\sigma\right] = \alpha\left\{e^{-\sigma^2} + \sqrt{\pi}\,\sigma\left[\operatorname{erf}(\sigma) + C\right]\right\} \tag{3.66}$$

using the error function

$$\operatorname{erf}(\eta) = \frac{2}{\sqrt{\pi}}\int_{-\infty}^{\eta} e^{-\tau^2}\,d\tau \tag{3.67}$$

and introducing an arbitrary constant of integration C in order to pass from indefinite to definite integral. The general solution of (3.53) now writes, using f_1 and f_2 as basis solutions

$$\begin{aligned} f(\sigma) &= A_1\, f_1(\sigma) + B_1\, f_2(\sigma) \\ &= -A_1\,\sigma + B_1\left\{e^{-\sigma^2} + \sqrt{\pi}\,\sigma\left[\operatorname{erf}(\sigma) + C_1\right]\right\} \end{aligned} \tag{3.68}$$

in which constant α is now included in constant B_1. Constant C_1 may be either concatenated with constant A_1 such that only two constants have to be determined from boundary conditions, or arbitrarily chosen for convenience. Figure 3.12 features the error function as defined in (3.67), while Figure 3.13 represents $\psi(\sigma)$, defined as the part in braces of expression (3.68) in the case where $C_1 = 1$.

$$\psi(\sigma) = e^{-\sigma^2} + \sqrt{\pi}\,\sigma\left[\operatorname{erf}(\sigma) + 1\right] \tag{3.69}$$

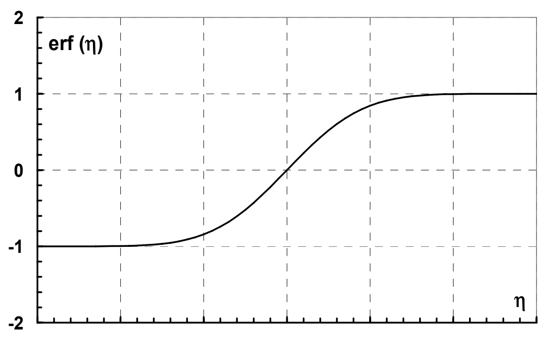

Figure 3.12: Error function $\operatorname{erf}(\eta) = \frac{2}{\sqrt{\pi}}\int_{-\infty}^{\eta} e^{-\tau^2}\,d\tau$

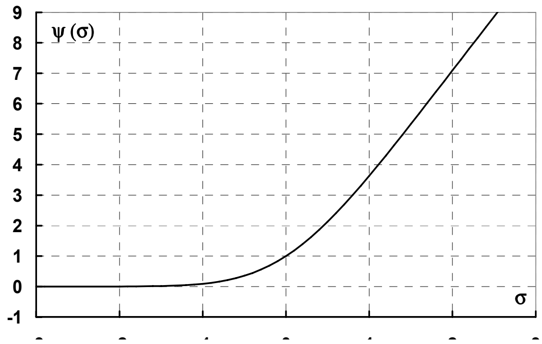

Figure 3.13: Function $\psi(\sigma)=e^{-\sigma^2}+\sqrt{\pi}\,\sigma\,[\mathrm{erf}(\sigma)+1]$

As the integral of the complementary error function may be written

$$\int \mathrm{erfc}(\eta)\,d\eta=\int[1-\mathrm{erf}(\eta)]\,d\eta=\eta\,\mathrm{erfc}(\eta)-\frac{e^{-\eta^2}}{\sqrt{\pi}}=\eta\,[1-\mathrm{erf}(\eta)]-\frac{e^{-\eta^2}}{\sqrt{\pi}} \tag{3.70}$$

it is interesting to redefine A_1 ($A'=-A_1$), B_1 ($B'=B_1\times\pi^{1/2}$) and C_1 ($C'=-1$) in (3.68) to write the function f (σ) under the alternative form

$$\mathrm{f}(\sigma)=A'\sigma+B'\left[\frac{\mathrm{e}^{-\sigma^2}}{\sqrt{\pi}}+\sigma[\mathrm{erf}(\sigma)-1]\right]=A'\sigma+B'\,\mathrm{ierfc}(\sigma) \tag{3.71}$$

with function ierfc (η) defined as the opposite of the integral of the complementary error function represented in Figure 3.14:

$$\mathrm{ierfc}(\eta)=-\int \mathrm{erfc}(\eta)\,d\eta=\frac{\mathrm{e}^{-\eta^2}}{\sqrt{\pi}}-\eta\,\mathrm{erfc}(\eta)=\frac{\mathrm{e}^{-\eta^2}}{\sqrt{\pi}}-\eta\,[1-\mathrm{erf}(\eta)] \tag{3.72}$$

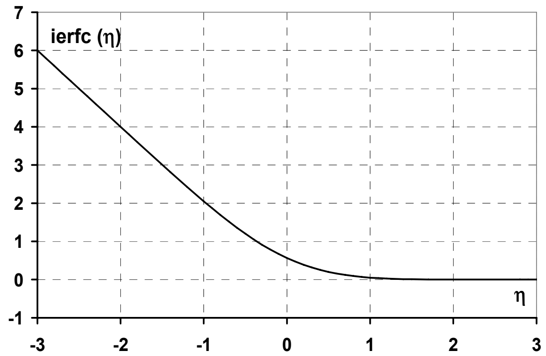

Figure 3.14: Function ierfc (η)

So, using (3.44) and (3.45), the bed level writes

$$z_b\left(x,t\right)=\mathrm{f}\left(\sigma\right)\xi(t)=2\sqrt{Dt}\left[A'+B'\,\mathrm{ierfc}(\sigma)\right] \qquad (3.73)$$

3.5.4 Restrictions on the initial and boundary conditions in similarity structure

The assumed similarity structure also imposes certain restrictions on the boundary and initial conditions that can be applied. First, for boundary conditions of ODE (3.53) to be specified at given values of ratio $\sigma = x/\xi(t)$, the boundary positions s_1 and s_2 must be of the form

$$s_1 = \lambda_1 \xi(t), \quad s_2 = \lambda_2 \xi(t), \qquad (3.74)$$

where scaling constants λ_i, $i=1,2$ can be either given or unknown (and must then be subject to additional boundary conditions). Form (3.74) allows non-moving boundary conditions, but only at locations $s_i = 0$ or $s_i \to \mp\infty$. Conversely, any λ_i different from zero or infinity yields a moving boundary. Restrictions on boundary speeds then follow from

, $$\frac{ds_i}{dt} = \lambda_i \frac{d\xi}{dt} = \frac{2D\lambda_i}{\xi} = \frac{2D\lambda_i^2}{s_i}, \qquad (3.75)$$

which implies that products $s_i(ds_i/dt)$ must be invariant. Other boundary invariants implied by similarity form (3.44) and their consequences (3.50) and (3.51) are

$$z_{b_i}/\xi,\ \ z_{b_i}/s_i \text{ and } (\partial z_b/\partial x)_i, \tag{3.76}$$

where index i is used to indicate boundary values, i.e. $z_{b_i} = z(s_i, t)$ and $(\partial z_b/\partial x)_i = (\partial z_b/\partial x)|_{x=s_i}$. Simple boundary conditions guaranteed to satisfy the similarity structure can therefore be imposed by setting any one of these invariants equal to a prescribed constant, or by specifying a relationship between two different invariants. Examples will be provided below.

Likewise, initial conditions are subject to certain restrictions. Moving boundary conditions must start from the origin at time $t = 0$, i.e. $s_i(0) = 0$. If instead, either of the boundaries is sent to infinity, profiles of constant slope are required on the corresponding half- domain:

$$z_b(x,0) = \begin{cases} -S_1 x & x < 0 \\ -S_2 x & x > 0 \end{cases} \tag{3.77}$$

The corresponding boundary condition at infinity must be of the form $(\partial z_b/\partial x)_i = -S_i$.

The requirements laid out above still leave much room for choice, allowing for any combination of fixed and moving boundaries, each subject to boundary conditions of different types. No systematic classification will be attempted here. Instead, our objective in the present work is to derive detailed solutions for our problems involving moving boundary in semi-infinite channels.

Chapter 4

Fluvial morphodynamics in supercritical flow over mobile bed: Aggradation and degradation

4.1 Introduction

In mountainous environments, movable bed channel reaches are subject to supercritical flows. A typical case is that of a torrential stream conveying sediment from an upstream catchment to a downstream alluvial fan, with transport occurring as bedload. From a geomorphological and engineering point of view, it is interesting to try characterising the response of the channel bed to changes in upstream loading and downstream conditions.

Consider a steep-sloped channel of finite length, with a steady water discharge and a given initial bed profile. If a stable supply of sediment is imposed upstream, overloading or underloading respectively results in channel aggradation or degradation. Tending to equalise sediment supply and transport capacity, the system will evolve towards a state of morphological equilibrium characterised ultimately by a constant slope (Fig. 4.1).

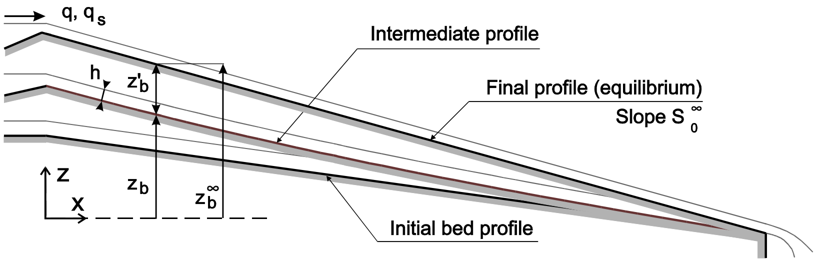

Figure 4.1: Slope evolution resulting from sediment overloading. z_b' =transient component of bed level, z_b^∞ =equilibrium bed level, $\partial^2 z_b'(x,t)/\partial x^2 > 0$

To deal with the problem of the morphological evolution of mountainous rivers where supercritical uniform flow regime is prevailing, experimental, analytical and numerical approaches were proposed.

In the present work, we develop analytical solutions similar to that of Gill (1983). In the next part, they will be compared with full numerical results obtained from SedRiv numerical model based on the implicit four point scheme of Preissmann and with new measurements obtained in the UCL steep-sloped laboratory flume. A new explicit expression for the response time, deriving from the theoretical analysis, is also compared with the empirical response times characterising both our own data and the data of other investigators. This chapter is organised as following:

In the first section, the conducted aggradation degradation test and the experimental procedure are described.

The second section consists of theoretical and analytical approach of transient bed profile and solid discharge of a steep-sloped channel of finite length. The transient evolution of the bed profile is compared. An explicit theoretical expression for the dominant response time is shown to compare favourably with the present measured data and those of previous investigators.

In the third section, the SedRiv numerical model based on the implicit four-point Preissmann scheme and using a double sweep method is rapidly explained. Finally the results of the used approaches are compared together with experimental data of other investigators.

4.2 Experiments of aggradation and degradation

4.2.1 Description

The idealized experiments reproducing a typical transient aggradation or degradation under a constant overloading or underloading sediment supply were conducted using a sediment flume facility described in chapter 2.

Under supercritical flow conditions, the water depth is self-regulated upstream through a control section at the channel entrance and falls freely downstream at the channel outlet. Aggradation and degradation experiments were conducted at constant water discharge and sediment supply upstream. The results have been obtained for the following ranges of parameters: initial slopes from 1 to 3.5 %, Froude number in the range 1.25 to 1.80.

4.2.2 Experimental procedure

Experiments were carried out in the following sequence: (a) the sediment is set with the desired initial slope, (b) the sediment bed is saturated with a small liquid discharge, (c) the liquid discharge is increased progressively up to the decided value and (d) a constant sediment discharge is provided upstream by means of the sediment feeder.

The measurement of the water surface and the bed profile have been executed at regular time intervals by means of a probe mounted on a trolley pulled alternately in the upstream and downstream directions. Several experiments were performed within the following ranges of main initial parameters reported in Table 4.1.

Run #	$S_{initial}$(%)	Q (l/s)	Q_s	S_{final} (%)
Run 1	1	7.65	0.070	2.22
Run 2	2	7.98	0.101	2.79
Run 3	2.79	8.31	0.101	2.9
Run 4	3	5.12	0.101	3.68
Run 5	2.14	7.98	0.147	2.76
Run 6	3.38	15.87	0.101	2.45

Table 4.1: Main experimental parameters of aggradation-degradation experiments in fully supercritical flow. The volumetric sediment discharge Q_S is defined from weighted sediment and is including voids

4.3 Analytical solution for aggradation and degradation in supercritical flow

A number of authors (Yen et al., 1987; Yen et al., 1992; Bianco et al., 1994) have observed experimentally the asymptotic character of the approach to equilibrium which results from sediment overloading and underloading in reaches of finite length. In particular, their measurements exhibit a well defined response time for which Yen et al. (1992) have proposed an empirical characterisation.

For channels of infinite length, analytical solutions such as proposed by Soni et al. (1980), Jain (1981) and Gill (1983), based on the linear diffusion model of de Vries (1973), are known to compare reasonably well with experimental measurements, those of Soni et al. (1980), constituting the main empirical reference. Analytical solutions have been derived as well for channels of finite length (Gill, 1983) but do not appear to have been confronted with experimental data.

4.3.1 Transient bed profile

Let's recall again the sediment continuity equation which is non-linear in general, but can be approximated by linearization around the equilibrium slope S_0^∞ corresponding to the equilibrium sediment discharge imposed upstream q_s^∞.

$$\frac{\partial(h\hat{C})}{\partial t} + (1-\varepsilon_0)\frac{\partial z_b}{\partial t} + \frac{\partial q_s}{\partial x} = 0 \tag{4.1}$$

As the sediment discharge converges everywhere towards this value S_0^∞, we can write:

$$q_s(x,t) = q_s^\infty + \left(\frac{\partial q_s}{\partial S_0}\right)_{q=\mathrm{cst}}^{\infty} \left(S_0(x,t) - S_0^\infty\right) + \dots \tag{4.2}$$

The bed level can be decomposed into asymptotic z_b^∞ and transient components z_b' (see Fig. 4.1) according to:

$$S_0 = -\frac{\partial z_b}{\partial x} = -\frac{\partial}{\partial x}\left(z_b^{\infty} - z_b'\right). \tag{4.3}$$

Since the asymptotic component of the bed level z_b^{∞} is independent of time, the sediment continuity equation (4.1) can be rewritten in terms of the transient component as:

$$-\frac{\partial z_b'}{\partial t} + \frac{1}{1-\varepsilon_0}\frac{\partial q_s}{\partial x} = 0\,, \tag{4.4}$$

where we have neglected the first term in (4.1) accounting for storage due to the sediment load in the water column. Substitution of (4.2) and (4.3) into equation (4.4) along with the observation that the equilibrium slope S_0^{∞} is constant then yields:

$$\frac{\partial z_b'}{\partial t} = \frac{1}{1-\varepsilon_0}\left(\frac{\partial q_s}{\partial S_0}\right)_{q=\mathrm{cst}}^{\infty}\frac{\partial^2 z_b'}{\partial x^2} = D\,\frac{\partial^2 z_b'}{\partial x^2} \tag{4.5}$$

Equation (4.5) constitutes a linear diffusion equation and has been used as a morphodynamic model by de Vries (1973). For the case of aggradation and degradation of a channel of finite length which concerns us here, solutions can be derived in the form of a Fourier series (Gill, 1983) in close analogy to the problem of heat diffusion in a slab of finite thickness (see e.g. Mei, 1995). First, the boundary condition at the downstream end and upstream end can be expressed as:

$$x = L:\; z_b'=0\,; \quad x=0:\; q_s = q_s^{\infty} \overset{(4.2)}{\Rightarrow} S_0 = S_0^{\infty} \overset{(4.3)}{\Rightarrow} \frac{\partial z_b'}{\partial x} = 0 \tag{4.6a,b}$$

the general solution of equation (4.5) can be obtained by separation of variables as the product of an exponential function of time and trigonometric functions of distance. Choice of the trigonometric component derives from boundary condition (4.6a) and we can write:

$$z_b' = X(x)\,T(t) \tag{4.7}$$

Skipping over the trivial cases in which the separation constant is either positive or zero, we write

$$\frac{X''}{X}=\frac{T'}{T}\frac{1}{D}=-\alpha_1^2 \tag{4.8}$$

Where, D a diffusion coefficient and k is constant. This equality leads to two ordinary differential equations

$$T' + D\,\alpha_1^2 T = 0 \text{ and } X'' + \alpha_1^2 X = 0 \qquad (4.9), (4.10)$$

The general solutions are

$$T = e^{-D\alpha_1^2 t} \text{ and } X = ASin\alpha\, x + BCos\alpha\, x \qquad (4.11), (4.12)$$

Using the above boundary conditions (4.6a, b) consequently we find

$$z_b'(x,t) = A\mathrm{e}^{-\frac{t}{T}}\sin\left(\sqrt{\frac{1}{TD}}(L-x)\right) \tag{4.13}$$

where T is a time constant which takes a discrete set of eigenvalues imposed by boundary condition (4.6b), i.e. :

$$T_n = \frac{1}{D}\left(\frac{1}{2n+1}\frac{2}{\pi}L\right)^2 \; n = 0, 1, 2,\ldots, \infty \tag{4.14}$$

leading to a complete solution for the transient bed profile expressed as a Fourier series :

$$z_b'(x,t) = \sum_{n=0}^{\infty}\left[A_n \mathrm{e}^{-\frac{t}{T_n}}\sin\left((2n+1)\frac{\pi}{2}\frac{L-x}{L}\right)\right] \approx A_0\mathrm{e}^{-\frac{t}{T_0}}\sin\left(\frac{\pi}{2}\frac{L-x}{L}\right) + \ldots$$

(4.15a,b)

The latter approximation (4.15) results from the observation that the time constants (4.14) decrease quadratically with n. This means that the smaller wavelength modes are damped very quickly and that the first term of the series dominates after a short time.

The coefficients A_n in Fourier Series are given in (4.16a,b)

$$A_n = \frac{2}{L}\int_0^L (S_0 - S_0^\infty)(L-x)\sin\left((2n+1)\frac{\pi}{2}\frac{L-x}{L}\right)dx\,, \qquad (4.16a)$$

giving

$$A_n = \frac{(-1)^n}{(2n+1)^2}\frac{8}{\pi^2}L(S_0 - S_0^\infty) \text{ and } A_0 = \frac{8}{\pi^2}L(S_0 - S_0^\infty) \qquad (4.16b, c)$$

A characteristic response time for the problem can thus be given by the following theoretical expression:

$$T_0^{th} = \left[\frac{1}{1-\varepsilon_0}\left(\frac{\partial q_s}{\partial S_0}\right)^\infty_{q=cst}\right]^{-1}\left(\frac{2}{\pi}L\right)^2 \quad . \qquad (4.17)$$

Approximation (4.14b) can also be integrated over length L to obtain an evolution equation for the volume of sediment V stored within the channel. It can be written in integral and differential forms respectively as:

$$\frac{V(t)-V^i}{V^\infty - V^i} = 1 - e^{-\frac{t}{T_0}}\,; \quad \frac{dV}{dt} = \frac{1}{T_0}\left(V^\infty - V\right) \qquad (4.18a,b)$$

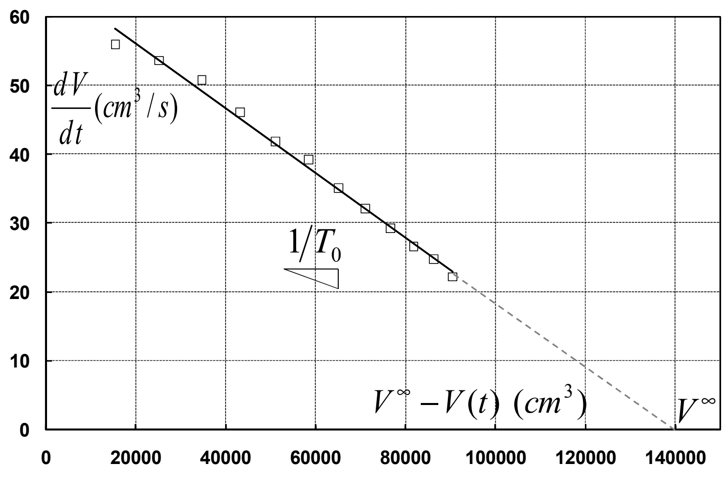

Figure 4.2: Approximation of time scale characteristic from experimental data (run# 2)

where V^i is the initial sediment volume. Based on experimental observations, relations (4.17) have been proposed as an interpretative model by Yen et al. (1992) and adopted as such by Bianco et al. (1994). We show here that, at least for supercritical flow, such equations can be derived from a theoretical analysis with the important consequence that an explicit expression can be obtained for the response time T_0. Experimentally, we can obtain V^∞ and T_0 Fig 4.2.

4.3.2 Harmonics calculation

In order to show the impact of different harmonics on the analytical solution giving the transient bed profile, calculation of these harmonics for at least *n* first values is needed.

Unlike, the wave equation whose solution oscillates in time, the diffusion process is distinguished by attenuation in time.

Example of harmonics calculation

Computation of the *n* (*n* =0, 1, 2) first harmonics in Fourier series allows to confirm that the T_0 is the dominant response time. The following Figures 4.3a to 4.3d obtained from equations (4.19-4.21) illustrate the harmonics calculation for t/T_0 = 0, 0.1 and 0, 3 corresponding to finite channel length. Without carrying out the general solution, we can note that the first harmonic has a determinant influence on the global solution.

$$\frac{z_b'(x,t)}{z_b'(x,t)_{upst}} = \sum_{n=0}^{\infty}\left[\frac{(-1)^n}{(2n+1)^2}\frac{8}{\pi^2}\,\mathrm{e}^{-\frac{t}{T_n}}\sin\left((2n+1)\frac{\pi}{2}\frac{L-x}{L}\right)\right] \tag{4.19}$$

$$z_b'(x,t)_{upst} = z_b'(0,t) = L\,(S-S^\infty)\ ,\ \frac{t}{T_n} = \frac{t/T_0}{(2n+1)^2} \qquad (4.20), (4.21)$$

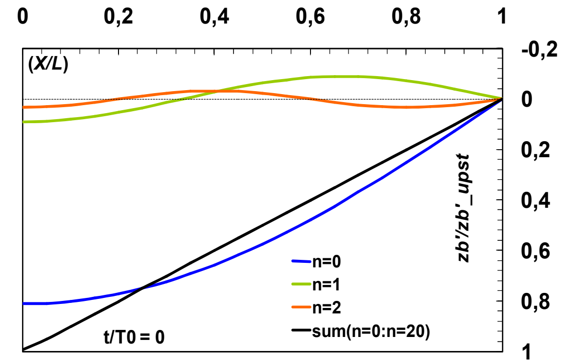

Figure 4.3a: Dimensionless harmonics (n = 0, 1, 2) and the sum of the 20th first harmonics for finite channel length ($t/T_0 = 0$)

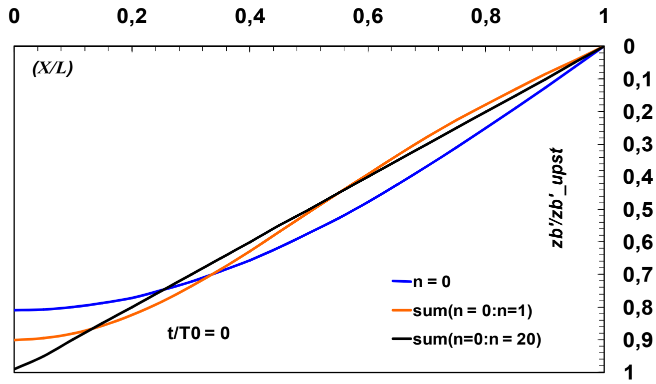

Figure 4.3b: Dimensionless harmonics (n = 0), the sum of the first two (n = 0, n =1) and the sum of the 20th first harmonics for finite channel length (t/T_0 = 0)

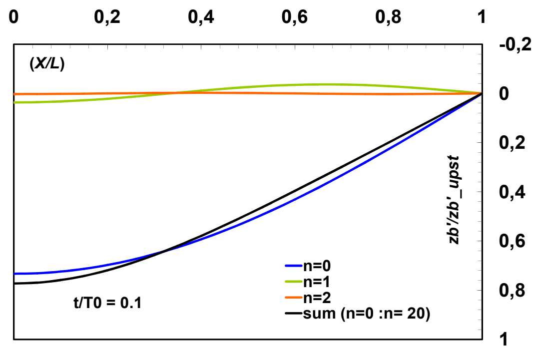

Figure 4.3c: Dimensionless harmonics (n = 0, 1, 2) and the sum of the 20th first harmonics for finite channel length ($t/T_0 = 0.1$)

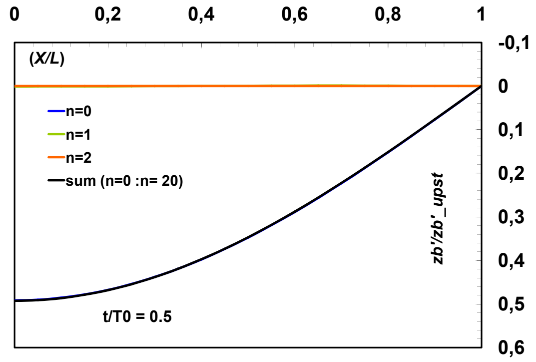

Figure 4.3d: Dimensionless harmonics (n = 0, 1, 2) and the sum of the 20th first harmonics for finite channel length ($t/T_0 = 0.5$)

4.4 Approximation of the equilibrium bed slope in the steep-sloped reach from few bed level measurements

From the complete solution for the transient bed profile formulated above, a simple analytical expression, using few bed level measurements at three times and without knowing the sediment transport relation, allows estimating the equilibrium bed slope S^{∞} for aggrading or degrading steep sloped river beds (Fig 4.4).

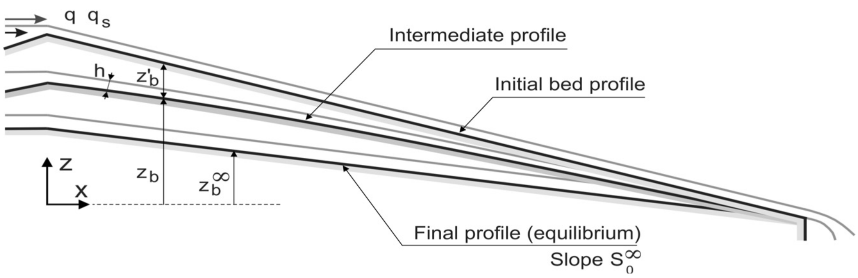

Figure 4.4: Slope evolution resulting from sediment underloading.
z_b' =transient component of bed level, z_b^{∞} =equilibrium bed level,
$\partial^2 z_b'(x,t) / \partial x^2 < 0$

For a fixed position x at three different times t_1, t_2 and t_3, $z_b'(x,t_1)$, $z_b'(x,t_2)$ and $z_b'(x,t_3)$ are measured. We can write the difference between these bed level values in terms of:

$$z_b'(x,t_1) - z_b'(x,t_2) = z_b(x,t_2) - z_b(x,t_1) = A_0\, Sin\left(\frac{\pi}{2}\frac{L-x}{L}\right)\left[e^{-t_1/T_0} - e^{-t_2/T_0}\right] \tag{4.22}$$

we obtain the same equation for t_1 and t_3

$$z_b'(x,t_1) - z_b'(x,t_3) = z_b(x,t_3) - z_b(x,t_1) = A_0\, Sin\left(\frac{\pi}{2}\frac{L-x}{L}\right)\left[e^{-t_1/T_0} - e^{-t_3/T_0}\right] \tag{4.23}$$

$$\frac{z_b(x,t_3) - z_b(x,t_1)}{z_b(x,t_2) - z_b(x,t_1)} = \frac{1-e^{-(t_3-t_1)/T_0}}{1-e^{-(t_2-t_1)/T_0}} \tag{4.24}$$

Once the equilibrium state is reached, $t_3 \to \infty \Rightarrow \quad z_b(x,t_3) \to z_b^{\infty}$ and (4.24) turn to

$$z_b^{\infty} = \frac{1}{1-e^{-(t_2-t_1)/T_0}}\left[z_b(x,t_2) - z_b(x,t_1)\right] + z_b(x,t_1) \tag{4.25}$$

From $z_b^{\infty}(x)$, we can find the equilibrium bed slope S_0^{∞}

4.5 Numerical simulation: SedRiv model

The present numerical simulation concerning the aggradation degradation of steep sloped river-bed is conducted using the SedRiv model developed by Zech (1996).

This model is based on the fully coupled implicit Preissmann 4-point scheme. It allows modelling a long scale morphological evolution simulation.

4.5.1 Numerical algorithm

The full system of Saint-Venant-Exner equations is non-linear equations and can also be solved numerically. This is achieved in the present work using the Preissmann four-point scheme Fig 4.5. In uncoupled form, this implicit algorithm has been applied previously to the aggradation problem by Lin and Tsai (1991) and we adopt here a fully coupled formulation. The dependent variables and their partial derivatives are developed in the following finite difference form:

$$f(x,t) = \theta\phi f_{i+1}^{j+1} + \theta(1-\phi) f_i^{j+1} + (1-\theta)\phi f_{i+1}^{j} + (1-\theta)(1-\phi) f_i^{j} = \theta\phi(\Delta f_{i+1} - \Delta f_i) + \theta\Delta f_i + \phi f_i + f_i \tag{4.26}$$

$$\frac{\partial f}{\partial x} = \frac{1}{\Delta x}\left[\theta\left(f_{i+1}^{j+1} - f_i^{j+1}\right) + (1-\theta)\left(f_{i+1}^{j} - f_i^{j}\right)\right] = \frac{1}{\Delta x}\left[\theta\left(\Delta f_{i+1} - \Delta f_i\right) + \left(f_{i+1} - f_i\right)\right] \tag{4.27}$$

$$\frac{\partial f}{\partial t} = \frac{1}{\Delta t}\left[\phi\left(f_{i+1}^{j+1} - f_{i+1}^{j}\right) + (1-\phi)\left(f_i^{j+1} - f_i^{j}\right)\right] = \frac{1}{\Delta t}\left[\phi\Delta f_{i+1} + (1-\phi)\Delta f_i\right] \tag{4.28}$$

where θ and ϕ are weighting coefficient pertaining to time and space respectively. The symbol j refers to the variable increments over the time step. From (4.26-4.28), a linear system of equations can be formulated for every reach $[x_i, x_{i+1}]$, and the various systems can be concatenated (Correia et al., 1992) into the following formulation linking the upstream ($i = 0$) and the downstream ($i = m$) variable increments :

$$\begin{bmatrix} \Delta h_m \\ \Delta q_m \\ \Delta z_{b,m} \end{bmatrix} = [\mathbf{M}] \begin{bmatrix} \Delta h_0 \\ \Delta q_0 \\ \Delta z_{b,0} \end{bmatrix} + [\mathbf{N}] \tag{4.29}$$

Where six unknowns appear, three of which are to be determined by applying appropriate boundary conditions. For the supercritical aggradation or degradation problem, $\Delta q_0 = 0$, Δh_0 is linked to Δq_0 by a critical-stage relationship, and $\Delta z_{b,m} = 0$.

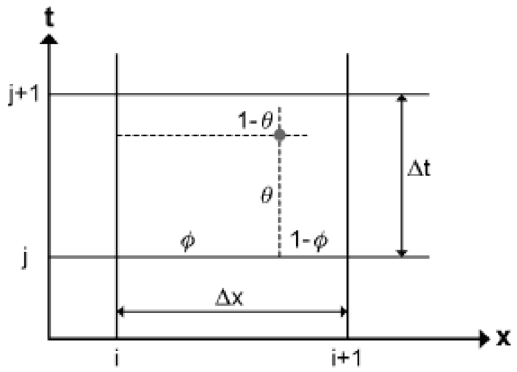

Figure 4.5: Preissmann scheme

4.5.2 Limitation of Preissmann scheme for transcritical flow

The implicit four-point of Preissmann scheme fails in transcritical flow modelling (Meselhe and Holly, 1997) in spite that is one of the most stable, robust and widely method in free-surface in pure subcritical or pure supercritical numerical modelling. This algorithm is based on the imposing of one boundary condition at each end of the computational domain.

The descritized Saint-Venant equations are written for every reach connecting two nodes in the computational domain. Therefore, for a domain of *N* computational points *N-1* computational reaches, there are *2N-2* discretised equations. Given that there are two unknowns at each node, there are *2N* unknowns, i.e., two boundary conditions are necessary to close the system of equations. If other than two boundary conditions are given, the system is ill-posed. For the case of transcritical trough the hydraulic jump two boundary conditions must be specified at the upstream end (liquid discharge and critical water depth) and one boundary condition at the downstream end (water level), i.e., there is a total of three boundary conditions Fig 4.6a. For transition in flow regime over a critical section, we will have only one boundary condition (liquid discharge) Fig 4.6b. Thus, the problem is poorly posed for both cases, for detail (see Meselhe and Holly, 1997).

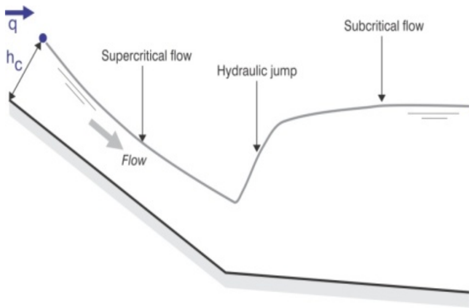

Figure 4.6a: Transcritical flow through hydraulic jump

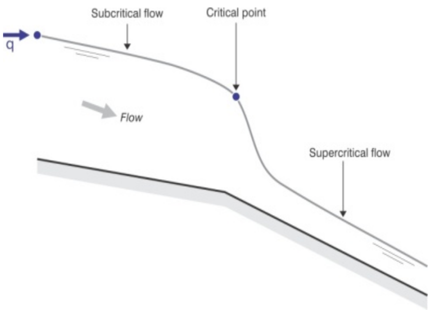

Figure 4.6b: Flow Transcritical flow through critical section

4.6 Comparison of results and discussion

4.6.1 Equilibrium bed slope simplified expression results comparison

Sample results for one degradation test are presented in the following Figure 4.7. The measured bed level data used in the theoretical determination of the equilibrium bed slope are corresponding to t_1=127 s, t_2= 484 s and t_3 = 788 s (run #2). Analytical full numerical results are very close even though only the first harmonic component was retained for the Fourier series. The computed equilibrium bed slope S_0^∞ is computed using SedRiv numerical model.

Agreement with experimental data is relatively good considering that the numerical results are obtained using the Meyer-Peter-Müller transport formula.

Run #	S_0 (%)	Q (l/s)	Q_s (l/s)	S_{num}^{∞} (%)	S_{ana}^{∞} (%)
Run 7	2.47	10.80	0.0701	2.32	2.28

Table 4.2: Main experimental parameters

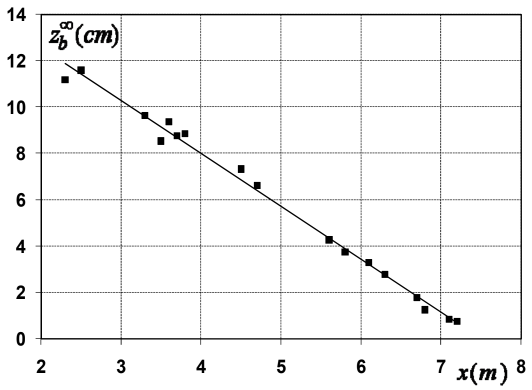

Figure 4.7: Equilibrium bed level for degradation test (run#7)

4.6.2 Analytical solution results comparison

Sample results for one of the aggradation tests are presented in Figures 4.8 and 4.9. Figure 4.8 features analytical, numerical and experimental bed profiles, while Figure 4.9 compares the various results for the time evolution of sediment volume. Parameters for the test are the following: channel length L = 6.90 m; width l = 0.50 m; initial slope S_0^i = 2.14 %; mean grain diameter d = 1.65 mm; porosity ε_0 = 0.42; bed roughness n_b = 0.0165; wall roughness n_w = 0.0195; water discharge Q = 7.98 l/s; upstream sediment load Q_s = 0.147 l/s. For these parameter values, the theoretical response time is T_0^{th} = 1670 s and the computed final equilibrium bed slope is S= 3.03 %. Analytical and full numerical results are very close even though only the first harmonic component was retained for the Fourier series. Agreement with experimental data is also quite good considering that the computed results are obtained using the Meyer-Peter-Müller transport formula. The good correspondence indicates that the exponential approximations (4.14b) and (4.17) accurately describe the morphological evolution of steep-sloped channels.

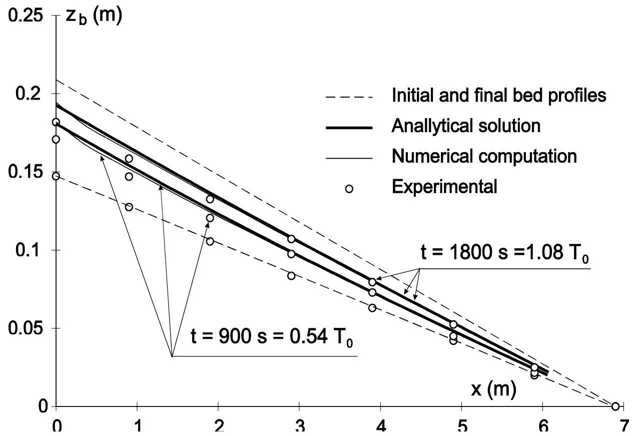

Figure 4.8: Evolution of bed profile

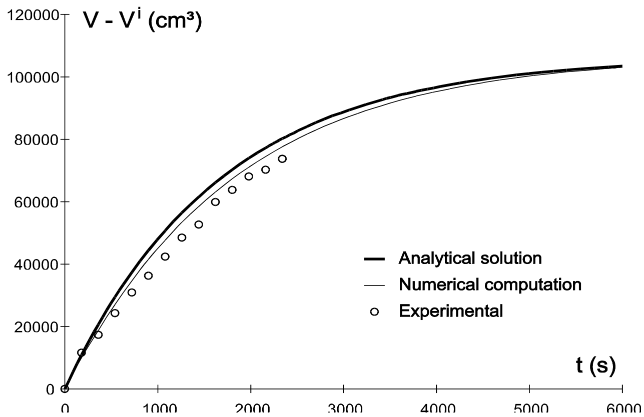

Figure 4.9: Time evolution of aggraded volume

In Figure 4.10, we compare theoretical and experimental results for the response time. Theoretical response times are computed using equation (4.16). For our own experiments, the Meyer-Peter-Müller equation is used to describe the dependence between q_s and S_0. For the experiments of other investigators, a simple linear relation is extracted from the measurements themselves. Experimental response times, on the other hand, are evaluated by fitting relation to (4.17) to the measured data. The results of Yen et al.

(1987) quoted by Lin and Tsai (1991) were obtained for coarse sediment material (d = 4.36 mm) in the supercritical regime (Froude number in the range 1.2-1.35). Both this set of data and our own pertain to steep-sloped channels, and exhibit a reasonable agreement between theoretical and experimental values.

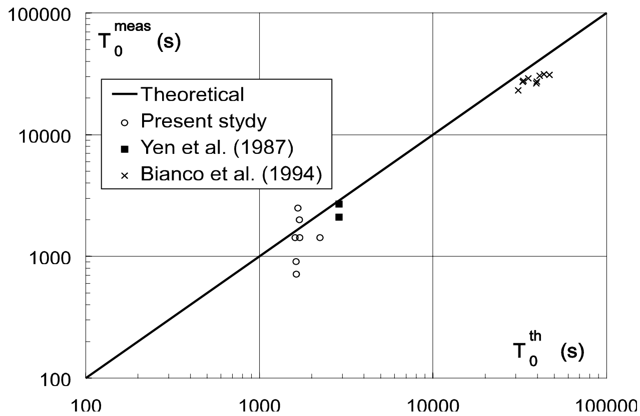

Figure 4.10: Theoretical and experimental response times

Application of equation (4.17) to subcritical flow cases can only be of indicative value since the analytical assumptions are not strictly valid. In particular, a hydrodynamic boundary condition has to be imposed downstream rather than condition (4.6a), in accordance with the characteristic analysis of section 2. For the subcritical experiments of Yen et al. (1992), a constant water level is imposed downstream and the analysis does not apply, so that the corresponding set of data is not included. No precise information is given concerning the downstream conditions for the subcritical results of Bianco et al. (1994) and we have plotted the results for reference in Figure 4.10. The observed agreement is to be taken with caution but suggests that a modified theoretical analysis could be applicable, provided adequate boundary conditions are supplied downstream.

4.7 Conclusions

Analytical, numerical, and experimental results were compared in the present work for the case of aggradation of a steep-sloped channel. For the supercritical case, good agreement was observed between the Fourier series solutions of Gill (1983), fully coupled numerical results and experimental measurements. In particular, a simple theoretical expression has been shown to reliably predict the dominant response time governing the morphological evolution of steep-sloped channels. For the subcritical case, analytical solutions might be applicable provided a modified analysis succeeds in accounting for adequate boundary conditions downstream. A simple analytical expression to estimate the equilibrium bed slope from few measurements has been confronted to the experiments.

Chapter 5

Fluvial morphodynamics in transcritical flow over mobile bed: Sediment front and hydraulic jump

5.1 Introduction

Sediment transport in alluvial channels constitutes the most common mode of long range sediment delivery. In many cases, this alluvial transit does not occur continuously from upstream to downstream. Instead, alluvial reaches may co-exist with reaches of different characters, for example: bedrock exposures, along which sediment may move but where erosion is limited; bodies of standing water, in which sediment transport does not happen and deposits amass. These transitions between alluvial and non-alluvial reaches do not remain static: these constitute moving boundary which migrates downstream. Figure (5.1) shows the Mississippi delta prograding in the ocean. An example of prograding delta in reservoir or dam is showed (Figure 1.3) lt exemplifies the impact of such prograding delta on the operating system of a small mountain dam.

Figure 5.1: Mississippi River delta (google) NASA's Terra satellite on March 5, 2001

The progradation of deltas into standing water has recently attracted much research attention. It has been studied by Swenson et al. (2000), Muto (2001), Sun et al. (2002), Scott and Parker (2003), Parker and Muto (2003), Kostic and Parker (2003), Bellal et al. (2003, 2005), Toniolo and Schultz (2005), Capart et al. (2007) and Goutière et al. (2009).

In the present chapter, we focus on a situation in which the morphodynamic evolution is driven by a sudden change in the flow regime from supercritical to subcritical, while the sediment supply upstream remains unchanged. From a geomorphological and from an engineering point of view, it is interesting to try to characterise the response of the channel bed to such a transition of flow regime. This transition may take place when a sudden rise of water level generates a subcritical condition in the downstream part of the stream, e.g. resulting from an obstruction, a weir, closing gate on a dam or check dam, placed across the channel Armanini et al. (2001), Busnelli et al. (2001).

From a physical standpoint, the conflict between upstream and downstream boundary conditions is resolved by the presence of a hydraulic jump propagating upstream, associated with a marked drop in bed shear stresses and transport rates, Bellal et al. (2003), Bellal et al. (2005) and Zech et al. (2008). Sieben (1999) proposed some theoretical analyses of similar discontinuous flow over mobile bed, indicating that different types of shocks may develop upon different perturbations, and in particular when the aggradation is driven by backwater as in the present study.

From a mathematical perspective, we focus our attention on semi-infinite channels featuring a single moving boundary: alluvial channels bounded on one end and the other boundary sent to infinity. Only the moving boundary case of the prograding sediment front (delta) into a body of standing water (lake or sea) is concerned by the present study. The alluvial profile is assumed to evolve according to a linear diffusion equation. At the moving boundary, compatibility conditions are then imposed as sketched in Figure (5.8).

Exact self-similar solutions can then be worked out analytically. The approach adopted for this purpose draws upon the work of Voller et al.

(2004) who exploited the symmetry of the diffusion equation to solve a related problem: the progradation of a fluvial delta starting from a channel of zero length. This approach is extended in the present thesis to semi-infinite channels in order to model the prograding sediment front by a novel analytical solution Capart et al. (2007).

In order to deal with the hydraulic jump over mobile bed and the resulted prograding sediment front, the remainder of the chapter is structured as follows: in section (1), the experiments are described in details, along with the measurements performed; then in section (2), the analytical self-similar solution of prograding sediment front is proposed; in section (3), a brief description of the two-layer model used for, the numerical simulation is worked out; and finally, in the last section (4), comparisons among results of the three approaches are given. At last we outline our conclusions.

5.2 Experiments of hydraulic jump and prograding sediment front

5.2.1 Description

The present section focuses on the morphodynamic response of the river bed to the presence of this hydraulic jump, in particular in terms of associated shock wave. Experiments were carried out in the UCL sediment flume designed and constructed in the frame of this thesis, showing that a sedimentation zone occurs in the region of reduced transport underneath the hydraulic jump, and tends to evolve in a steep bore of sediments presenting a front slope that is comparable to the submerged angle of repose. Growing in amplitude when propagating downstream, this bore progressively takes over the transition of flow regime from supercritical to subcritical, and the hydraulic jump vanishes.

This description is illustrated in Fig 5.2. Consider a steep-sloped channel of finite length initially in equilibrium, with constant water and sediment discharges and a uniform bed profile Fig. 5.2a. At reference time $t = 0$, a subcritical condition is imposed downstream by raising the water level. The resulting hydraulic jump and sediment bore are sketched in Figures. 5.2b-c.

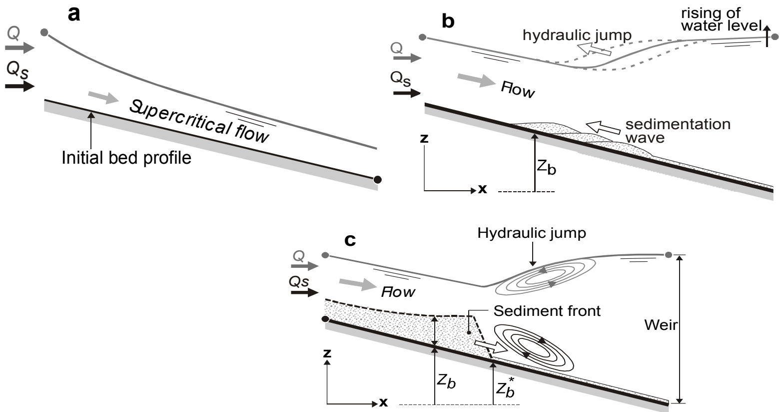

Figure 5.2 a-c*:* Sketch of the morphodynamic response of a steep-sloped supercritical flow to a sudden rise of downstream water level: (a) initial situation; (b) first stage of bed deformation; (c) second stage of bed deformation.

Aggradational shock fronts caused by the presence of transcritical flow are inherently different from those studied by previous authors in fully subcritical or supercritical flow, where the shock front continually strengthens rather than dissipates in time. The fronts are of considerable engineering significance because the arrival of the shock front at the dam corresponds to the near-completion of the process of reservoir sedimentation while in the upstream part of the stream it raises local water levels and increases flood frequency.

5.2.1 Experimental procedure

Experiments were carried out in the sediment flume, Fig 2.1 described in chapter 2, in the following sequence: (1) we start from a uniform supercritical flow fully developed throughout the channel length. The bed profile is in quasi-equilibrium, and a constant sediment supply is furnished upstream; (2) at time t=0, this equilibrium situation is perturbed by the rapid raise of a submerged weir at the downstream end of the flume, imposing a subcritical condition. This generates a hydraulic jump slowly propagating in the upstream direction. As a result, the modified sediment transport capacities initiate morphological evolution of the bed profile; (3) as the water depth above the downstream weir stabilises and the propagation of the hydraulic jump slows down, local deposition of sediments underneath starts to form a bore of sediments growing slowly in amplitude; (4) fed by the constant sediment supply from upstream, the bed further interacts with the hydraulic jump. Continuous deposition at the front of the sediment bore make it grow in amplitude as it migrates downstream; (5) the hydraulic jump noticeable at the free surface decreases in amplitude and progressively vanishes as the sediment front takes over the transition from supercritical to subcritical flow.

Several experiments were performed within the following ranges of parameters see Table 5.1: initial bed slopes from $S_0 = 2$ % to $S_0 = 4$ %; liquid discharges from $Q = 11.5$ to $Q = 15$ l/s; solid discharge $Q_s = 0.196$ l/s; height of the submerged weir raised at time $t = 0$ is $H_{weir} = 15.75$ cm. Initial Froude numbers ranged from $\mathrm{Fr}_0 = 1.88$ to $\mathrm{Fr}_0 = 2.47$; After development of the sediment front, Froude numbers were in the range $\mathrm{Fr} = 0.12$ to $\mathrm{Fr} = 0.28$ in the subcritical part of the flow, and $\mathrm{Fr} = 1.14$ to $\mathrm{Fr} = 1.52$ in the supercritical part.

Run #	S_0 (%)	Q (l/s)	Fr_0	Fr, subcrit.	Fr, supercrit.	Q_s (l/s)	$H_{w,down}$ (cm)
Run 1	3.55	11.5	1.92	0.13	1.14	0.196	20.86
Run 2	3.02	12	1.88	0.12	1.39	0.196	20.93
Run 3	2.74	15	2.47	0.13	1.27	0.196	22.63

Table 5.1: Main experimental parameters

Observation of water and bed levels during the tests were acquired using two different measuring systems: a probe at the axis of the channel, mounted on a trolley and pulled upstream and downstream repetitively, and an imaging system acquiring digital image sequences of the flow through the transparent side-wall. The probe measures alternatively water levels during the upstream translation and bed levels during the return movement, along the full length of the flume. The imaging system consists in a digital camera with a resolution of 1024×1024 pixels $\times$ 256 grey levels, operating at a frame rate of 2 images per second. The viewing window was chosen to observe more in details the formation and initial development of the sediment front, and extends from 2.9m to 3.8m from the upstream end of the flume. The bed elevations were checked to remain always higher than the steel plate at the bottom of the side-wall, allowing full visual access to the bed profile. Special attention was paid to the lighting conditions, in order to ensure good contrast between the sediment, water and air regions on the images. Specific image processing algorithms, involving mainly a combination of low-pass and high-pass filters, were developed to automatically derive the water and bed profiles. Camera calibration allows converting pixel co-ordinates in actual elevations. Overall accuracy of the imaging measurements is in the order of 1.0 mm.

5.2.3 Experimental results

Sample results obtained by the two distinct measuring systems are presented hereafter. Results include evolution of bed levels and water levels in time, evolution of bed slopes and sediment front positions. Sample images and water and bed profiles derived form those images show: (a) the initial conditions (Fig 5.3a-b); (b) the first humps formation (Fig 5.3c-f) and (c), the hydraulic jump and the development of the sediment front (Fig. 5.3g-s).

All figures are plotted with the same conventions: time $t = 0$ corresponds to the abrupt rise of downstream water level; horizontal co-ordinates are in meters, origin placed at the upstream end of the flume; vertical co-ordinates are in meters above the bottom of the flume at the downstream end.

Evolutions of bed and water levels derived from the sidewall digital images during run# 2 are plotted in the following Figures 5.3 at judiciously chosen times. Figs. 5.3a and 5.3b refer to the first instants before rising of downstream water level and generating a subcritical condition, following that the hydraulic jump coming from downstream enters the viewing window of the camera around $t \approx 20$s, and is seen at $t \approx 30$s to be nearly stabilised. On the illustrated corresponding bed profiles, Figs 5.3c to 5.3f it is clear that the bed already undergoes significant modifications during this step of migration and slow-down of the hydraulic jump: small humps of sediments deposit underneath the wave due to the reduced bed shear stresses. When the propagation speed of the wave is still substantial, deposited sediments are very limited and the corresponding sedimentation wave following its movement is limited in amplitude; as it slows down however, more and more sediments come to settle at the toe of the hydraulic jump, and the deposit slowly takes the form of a bore, as can be seen at time $t \approx 50$s in Figs.5.3g and 5.3h. Later configurations are plotted in Figs.5.3i to 5.3r, illustrating the second stage of bed deformation: the front is formed and now starts to slowly migrate downstream as it continues to be fed by deposited sediments. Sedimentation also occurs on the upstream slope of the sediment bore, resulting from the progressive adaptation of the slope to the new equilibrium, an observation that will be made clearer in the context of Fig. 5.5. Overall, the above observations are in line with the theoretical analysis of Sieben (1999) concerning the development of expansion and shock waves in discontinuous flows over mobile beds.

(a) Initial conditions

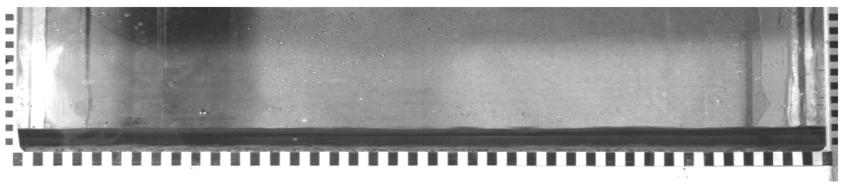

Figure 5.3a: Sample image showing the initial condition. Time t = 0s horizontal and vertical axes are 1cm; camera is set parallel to the initial bed profile.

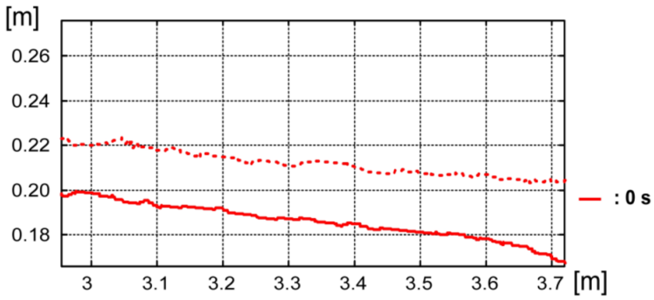

Figure 5.3b: Bed (continuous line) and water (dashed line) profiles derived from the digital images showing the initial water and bed profiles. Time $t = 0$s

(b) First stage: corresponding to sediment humps formation

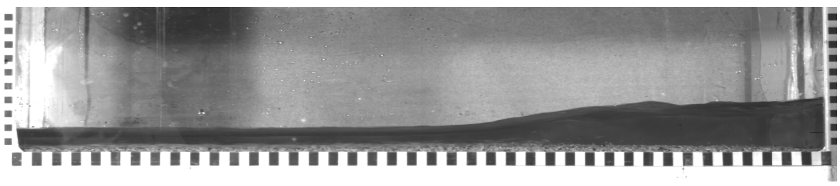

Figure 5.3c: Sample image showing the humps formation. Time t = 20s horizontal and vertical axes are 1cm; camera is set parallel to the initial bed profile.

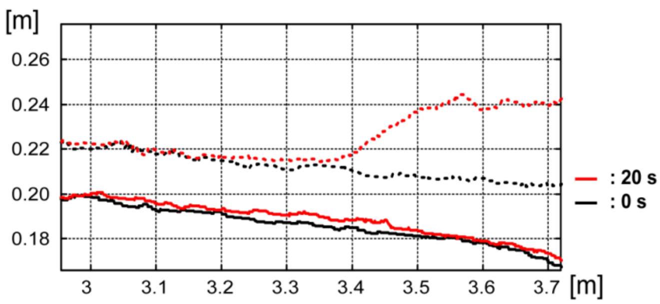

Figure 5.3d: Bed (continuous line) and water (dashed line) profiles derived from the digital images showing the first humps formation. Time t = 20s

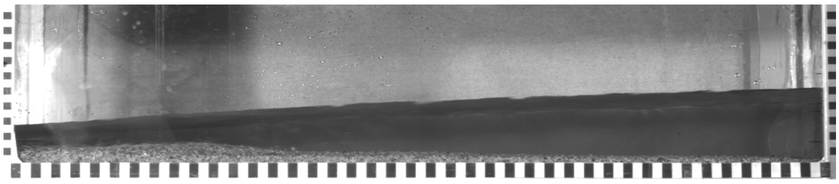

Figure 5.3e: Sample image showing the first humps formation. Time t = 30s horizontal and vertical axes are 1cm; camera is set parallel to the initial bed profile.

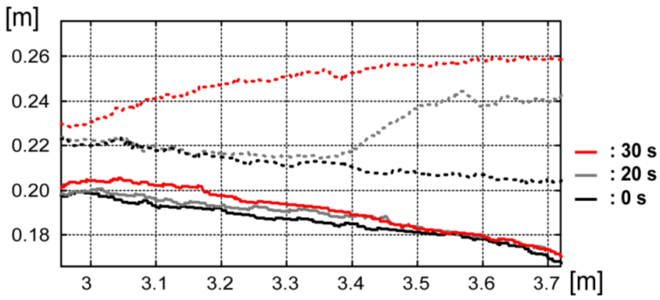

Figure 5.3f: Bed (continuous line) and water (dashed line) profiles derived from the digital images showing the first humps formation. Time t = 30s

(c) Second stage: corresponding to sediment front development

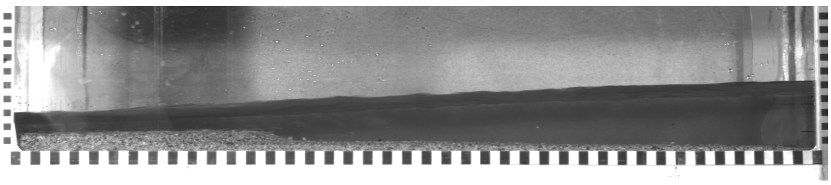

Figure 5.3g: Sample image showing the developing sediment front and vanishing hydraulic jump (upstream on the left side). Time t =50s after rise of downstream weir.

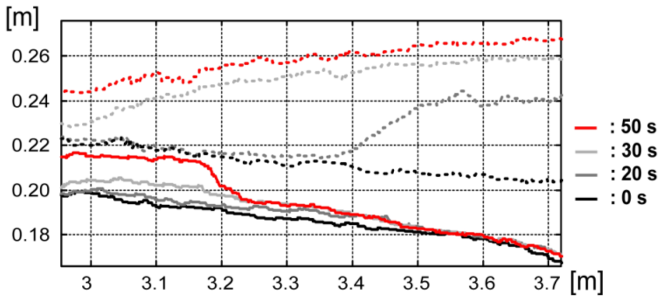

Figure 5.3h:.Bed (continuous line) and water (dashed line) profiles derived from the digital images showing the developing sediment front and vanishing hydraulic jump. Time t = 50s

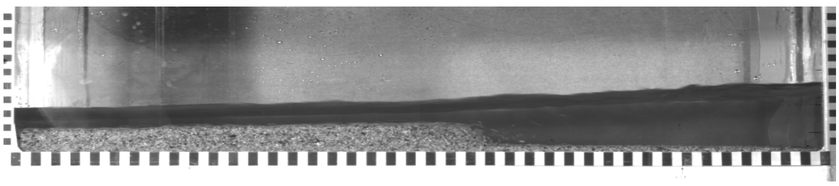

Figure 5.3i.: Sample image showing the developing sediment front and vanishing hydraulic jump (upstream on the left side). Time t =100s after rise of downstream weir, horizontal and vertical axes are 1cm; camera is set parallel to the initial bed profile.

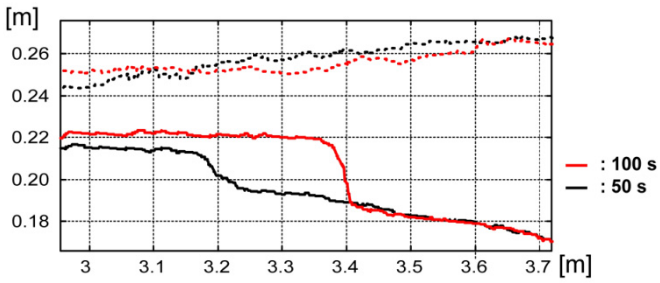

Figure 5.3j: Bed (continuous line) and water (dashed line) profiles derived from the digital images showing the developing sediment front and vanishing hydraulic jump. Time t = 100s

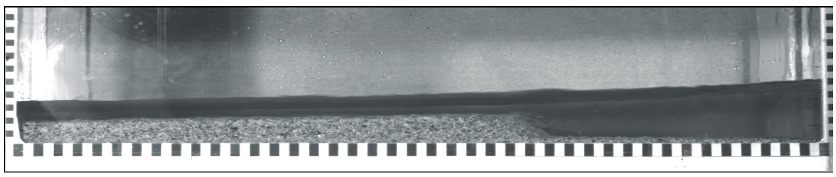

Figure 5.3k: Sample image showing the developing sediment front and vanishing hydraulic jump (upstream on the left side). Time t =135s after rise of downstream weir.

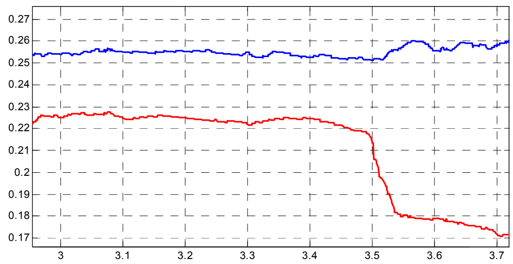

Figure 5.3l: Bed (red line) and water (blue line) profiles derived from the digital images showing the developing sediment front and vanishing hydraulic jump. Time t = 135s

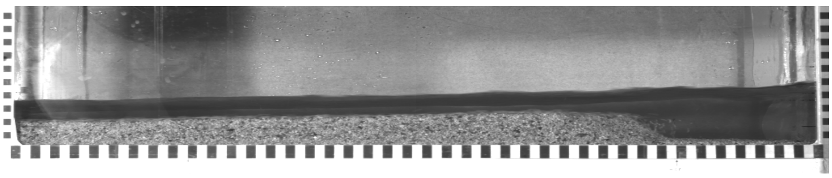

Figure 5.3m: Sample image showing the developing sediment front and vanishing hydraulic jump (upstream on the left side). Time t =150s after rise of downstream weir, horizontal and vertical axes are 1cm; camera is set parallel to the initial bed profile.

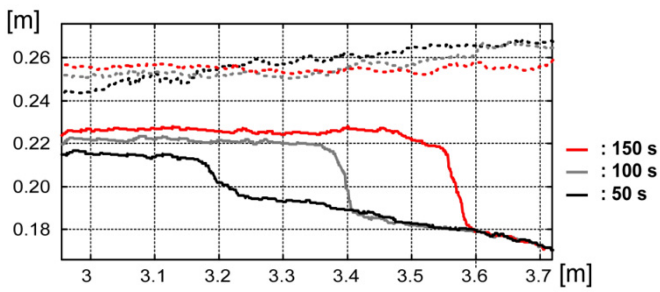

Figure 5.3n: Bed (continuous line) and water (dashed line) profiles derived from the digital images showing the developing sediment front and vanishing hydraulic jump. Time t = 150s

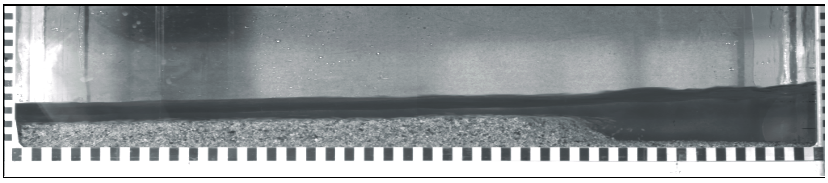

Figure 5.3o:.Sample image showing the developing sediment front and vanishing hydraulic jump (upstream on the left side). Time t =166s after rise of downstream weir, horizontal and vertical axes are 1cm; camera is set parallel to the initial bed profile.

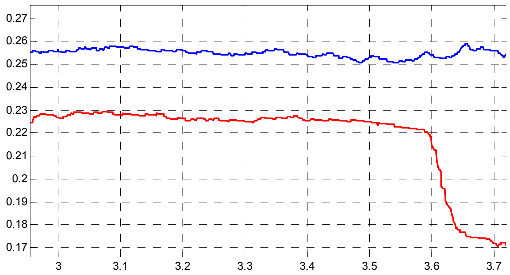

Figure 5.3p: Bed (red line) and water (blue line) profiles derived from the digital images showing the developing sediment front and vanishing hydraulic jump Time t = 166s

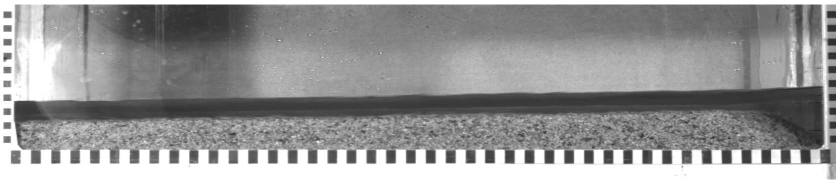

Figure 5.3q: Sample image showing the developing sediment front and vanishing hydraulic jump (upstream on the left side). Time t =200s after rise of downstream weir, horizontal and vertical axes are 1cm; camera is set parallel to the initial bed profile.

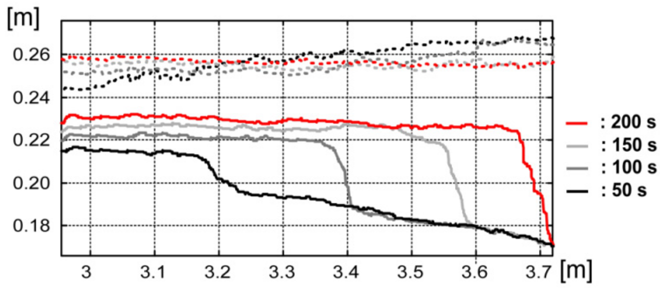

Figure 5.3r: Bed (continuous line) and water (dashed line) profiles derived from the digital images: second stage and front development and propagation while sediment bore takes place and the hydraulic jump collapses at 50s, 100s, 150s and 200s.

Figure.5.4 features similar experimental profiles acquired from the probe at different times for run #3. The initial supercritical flow at $t = 0$, corresponding to $Fr = 2.47$, is seen to be uniform over the whole measuring region. The first stage of bed deformation, featuring one water shock wave and one sediment disturbance moving upstream, is difficult to capture using the probe due to the rapidity of the phenomenon. The second stage, however, may be clearly observed. Besides the downstream-migrating sedimentation shock-wave described previously, a zone of progressive aggradation also extends in the upstream direction, causing further increase of the bed levels in the supercritical reach. As this aggradation develops, the slope of the channel in this region is decreased and tends to reach an equilibrium value at the end of the test. This adaptation of the upstream slope in function of time is illustrated in Fig. 5.5 for the three runs performed. We can distinguish two different stages of bed evolution: (a) the first stage is characterised by a sudden drop in sediment transport capacities under the stabilised hydraulic jump. Large local deposits strongly reduce the bed slope, creating even an adverse slope in the case of the largest discharge; (b) the second stage features an asymptotic evolution of the bed slope towards an equilibrium state in which the final slope is adjusted to the imposed constant sediment supply. Not unexpectedly, the lower discharges require a steeper equilibrium slope in order to increase stream power and be able to carry over all the supplied sediments. For this reason, S_∞ increases with decreasing liquid discharges. It should be noted that the duration of the experiments was restricted to 15-20 minutes due to the limited capacity of the sediment feeder, so no longer experimental observations were possible.

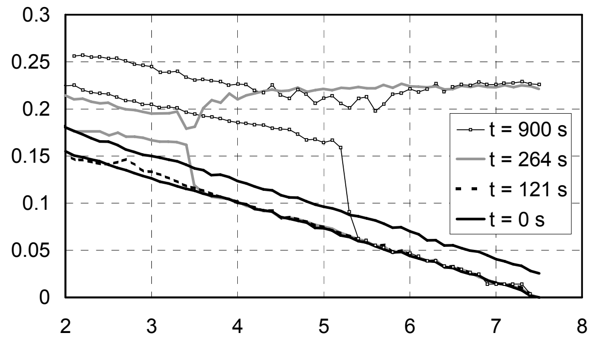

Figure 5.4: Bed and water profiles obtained from the probe at particular instants (run #3).

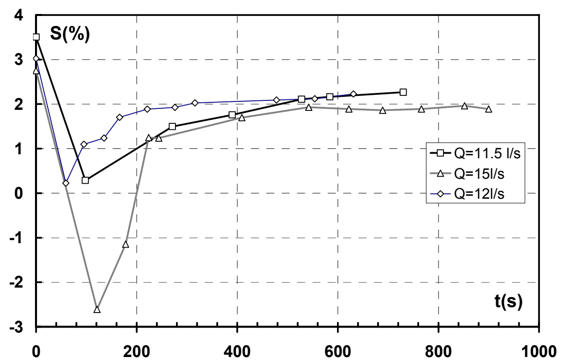

Figure 5.5: Evolution in time of the average bed slope upstream of the sediment front (run#1, run#2 et run#3).

Another feature noticeable in Fig.5.4 is the gradual transition between the supercritical and subcritical regions. Due to the sediment front, the hydraulic jump drastically reduces in amplitude and gets smooth.

Figure.5.6 shows the time evolution of the sediment front position. The propagation speed slowly decreases with time because the aggradational profile needs each time more sediment to form the rising height of the front.

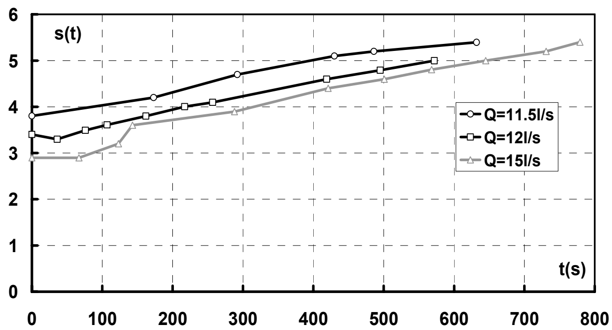

Figure 5.6: Evolution in time of the sediment front position

5.3 Self-similar solution for the prograding sediment front

The problem of the prograding delta considered hereafter is illustrated in Figure 5.7. This is a semi-infinite variant of the prograding delta problem treated earlier by Voller et al. (2004). As sketched in Figure 5.7, an alluvial channel of infinite length and constant slope *S*, is half-submerged at time $t = 0$ by a body of standing water of surface level ζ . If the channel is supplied with sediments, a delta forms, with a submerged foreset of slope R . Assumed constant, this slope corresponds to the angle of repose in the case of a Gilbert delta type (Kostic and Parker, 2003). For example, a mountain river depositing sediment into a freshwater lake would form this kind of delta. To make the problem more general, we let the lake level evolve as a function of time. For similarity to be preserved, however, the time dependence cannot be arbitrary. Instead, it is restricted to be of the form

$$\zeta(t) = \mu\xi(t) = 2\mu\sqrt{Dt} \,, \tag{5.1}$$

where μ is a dimensionless constant which controls the rate of lake level change. Negative values $\mu < 0$ correspond to a falling lake level, while positive values $\mu > 0$ correspond to a rising level. The special case of constant water level can of course be retrieved by setting $\mu = 0$. At first sight, this special type of time dependence may seem artificially contrived. In the next section, however, it will be shown that it arises naturally in certain circumstances.

$$\zeta(t) = \mu\,\xi(t) = 2\,\mu\,\sqrt{D\,t} \tag{5.2}$$

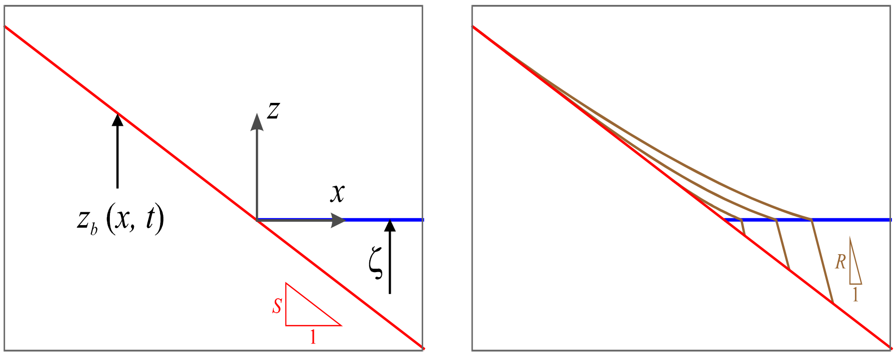

(a) Initial situation (b) Evolving delta

Figure 5.7: Prograding delta: definition sketch

The assumption behind the scheme on Fig.5.7 is that the water depth (assumed as steady uniform) in the upper reach is small enough to be neglected, such that the front head evolves along the horizontal line of the downstream lake level. In order to ensure the similarity, the front head location $s\,(t)$ is assumed to be scaled by the function $\xi\,(t)$, which implies

$$s(t) = \lambda\,\xi(t) = 2\,\lambda\sqrt{D\,t} \tag{5.3}$$

where λ is a scaling constant to be determined as a part of the solution.

The most significant solution idea is of this problem lies in the downstream boundary conditions (5.13). This condition equates the sediment discharge supplied by the alluvial channel at the edge of the water body with the rate of change of the underwater sediment volume. It can be derived hereafter from geometrical arguments (Swenson et al., 2000). Despite its apparent complexity, this condition satisfies the similarity requirements outlined earlier.

The corresponding mathematical problem is formulated as follows:

$$\frac{\partial z_b}{\partial t} - D\,\frac{\partial^2 z_b}{\partial x^2} = 0 \quad -\infty < x < s(t) \tag{5.4}$$

The initial condition is the initial slope *S*:

$$z_b(x) = -S\,x \quad \text{at} \quad t = 0 \tag{5.5}$$

The corresponding boundary conditions are the following

$$\frac{\partial z_b}{\partial x} = -S \quad \text{at} \quad x = -\infty \tag{5.6}$$

$$z_b = 0 \quad \text{at} \quad x = s(t) \tag{5.7}$$

to which it must be added the sediment continuity at the front since the sediment discharge at the front head (point M in Fig. 5.8) supplies in sediments the increase in mass of the delta front. The volume V_1 of this additional mass is the difference between triangles O_1NQ and MNQ.

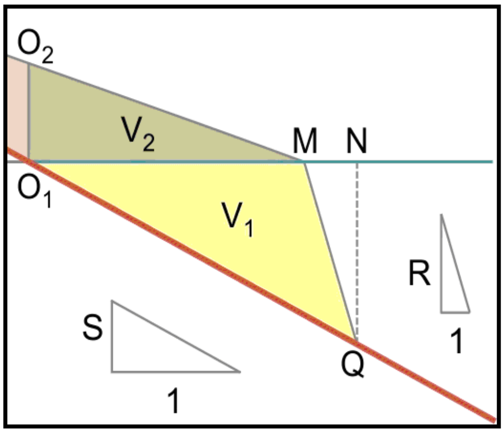

Figure 5.8: Front volume

Knowing that $O_1M = s$, and using the slope definition, the following properties can be derived:

$$\overline{NQ} = \begin{cases} \left(\overline{O_1M} + \overline{MN}\right) S = \left(s + \overline{MN}\right) S \\ \overline{MN}\ R \end{cases} \tag{5.8}$$

$$\left(s + \overline{MN}\right) S = \overline{MN}\ R \quad \Rightarrow \quad \overline{MN} = \frac{S}{R - S}\, s \tag{5.9}$$

$$\overline{NQ} = \overline{MN}\ R = \frac{R\,S}{R - S}\, s \tag{5.10}$$

$$V_1 = \frac{1}{2}\left(s + \overline{MN}\right)\overline{NQ} - \frac{1}{2}\,\overline{MN}\ \overline{NQ} = \frac{1}{2}\, s\ \overline{NQ} = \frac{1}{2}\,\frac{R\,S}{R - S}\, s^2 \tag{5.11}$$

So the mass supply at the front equals to the rate of front mass increase writes, using the property (3.33):

$$q_s\left(s,t\right) = \frac{8\sqrt{g}\,q}{C\left(s-1\right)}\, S = -D\,\frac{\partial z_b}{\partial x} = \frac{d}{dt}\left[\left(1-\varepsilon_0\right) V_1\right] = \frac{d}{dt}\left[\left(1-\varepsilon_0\right)\frac{1}{2}\,\frac{R\,S}{R-S}\, s^2\right] \tag{5.12}$$

leading to the internal boundary condition:

$$-D\frac{\partial z_b}{\partial x}=\frac{d}{dt}\left[\frac{1}{2}\frac{RS}{R-S}s^2\right] \quad \text{at} \quad x=s(t) \tag{5.13}$$

To introduce the boundary conditions, the easiest is using formulation (3.44-3.45)

$$z_b(x,t)=\mathrm{f}(\sigma)\,\xi(t)=2\sqrt{Dt}\;\mathrm{f}(\sigma) \tag{5.14}$$

with $\mathrm{f}(\sigma)$ expressed on the form (3.68) where arbitrary constant C has been chosen equal to 1:

$$\mathrm{f}(\sigma)=-A\sigma+B\left\{e^{-\sigma^2}+\sqrt{\pi}\,\sigma\left[\mathrm{erf}(\sigma)+1\right]\right\}=A\sigma+B\,\psi(\sigma) \tag{5.15}$$

where function $\psi(\sigma)$ has been defined in (3.69).The derivative of $\mathrm{f}(\sigma)$ writes

$$\begin{aligned}\mathrm{f}'(\sigma)&=-A+B\left\{e^{-\sigma^2}(-2\sigma)+\sqrt{\pi}\left[\mathrm{erf}(\sigma)+1\right]+\sqrt{\pi}\,\sigma\left[\frac{\partial}{\partial\sigma}\mathrm{erf}(\sigma)\right]\right\}\\&=-A+B\left\{e^{-\sigma^2}(-2\sigma)+\sqrt{\pi}\left[\mathrm{erf}(\sigma)+1\right]+\sqrt{\pi}\,\sigma\left[\frac{2}{\sqrt{\pi}}e^{-\sigma^2}\right]\right\}\\&=-A+B\sqrt{\pi}\left[\mathrm{erf}(\sigma)+1\right]\end{aligned} \tag{5.16}$$

Since

$$\sigma=\frac{x}{2\sqrt{Dt}} \tag{5.17}$$

$$\frac{\partial z_b}{\partial x}=\frac{\partial}{\partial x}\left[2\sqrt{Dt}\;\mathrm{f}(\sigma)\right]=\frac{\partial}{\partial\sigma}\left[2\sqrt{Dt}\;\mathrm{f}(\sigma)\right]\frac{\partial\sigma}{\partial x}=\mathrm{f}'(\sigma) \tag{5.18}$$

boundary condition (5.6) at $x=-\infty$ yields

$$A=S \tag{5.19}$$

while boundary condition (5.7) at the front head $x = s(t) = 2\lambda\sqrt{Dt}$ writes

$$\frac{z_b(s,t)}{2\sqrt{Dt}} = \mathrm{f}(\lambda) = -S\lambda + B\left\{e^{-\lambda^2} + \sqrt{\pi}\,\lambda\left[\mathrm{erf}(\lambda)+1\right]\right\} = -S\lambda + B\,\psi(\lambda) = 0 \tag{5.20}$$

yielding

$$B = \frac{S\lambda}{e^{-\lambda^2} + \sqrt{\pi}\,\lambda\left[\mathrm{erf}(\lambda)+1\right]} = \frac{S\lambda}{\psi(\lambda)} \tag{5.21}$$

Finally, continuity of sediment (5.13) at the front head $x = s(t) = 2\lambda\sqrt{Dt}$ writes, using (5.21):

$$-D\frac{\partial z_b}{\partial x}(s,t) = -D\,\mathrm{f}'(\lambda) = \frac{d}{dt}\left[\frac{1}{2}\frac{RS}{R-S}\left(2\lambda\sqrt{Dt}\right)^2\right] = 2\frac{RS}{R-S}\lambda^2 D \tag{5.22}$$

$$\mathrm{f}'(\lambda) = -2\frac{RS}{R-S}\lambda^2 \tag{5.23}$$

Using (5.16), (5.19) and (5.21) this equation (5.23) writes:

$$\begin{aligned}\mathrm{f}'(\lambda) &= -A + B\sqrt{\pi}\left[\mathrm{erf}(\lambda)+1\right] \\ &= -S + \frac{S\lambda}{e^{-\lambda^2} + \sqrt{\pi}\,\lambda\left[\mathrm{erf}(\lambda)+1\right]}\sqrt{\pi}\left[\mathrm{erf}(\lambda)+1\right] = -2\frac{RS}{R-S}\lambda^2\end{aligned} \tag{5.24}$$

Finally, the compatibility condition (5.24) leads to the following transcendental equation for the scaling constant λ :

$$2\frac{R}{R-S}\lambda^2 + \frac{\sqrt{\pi}\,\lambda\left[\mathrm{erf}(\lambda)+1\right]}{e^{-\lambda^2} + \sqrt{\pi}\,\lambda\left[\mathrm{erf}(\lambda)+1\right]} - 1 = 0 \tag{5.25}$$

Knowing λ, it is now possible to compute $z_b(x,t)$ from (5.14), (5.15), (5.19) and (5.21):

$$
\begin{aligned}
z_b(x,t) &= 2\sqrt{Dt}\ \mathrm{f}(\sigma) \\
&= -2\sqrt{Dt}\ A\,\sigma + 2\sqrt{Dt}\ B\left\{e^{-\sigma^2} + \sqrt{\pi}\,\sigma\left[\mathrm{erf}(\sigma)+1\right]\right\} \\
&= -S\,x + 2\,S\sqrt{Dt}\ \lambda\,\frac{e^{-\sigma^2} + \sqrt{\pi}\,\sigma\left[\mathrm{erf}(\sigma)+1\right]}{e^{-\lambda^2} + \sqrt{\pi}\,\lambda\left[\mathrm{erf}(\lambda)+1\right]}
\end{aligned}
\tag{5.26}
$$

with $$\sigma = \frac{x}{2\sqrt{Dt}} \tag{5.27}$$

The solution illustrated in Figure 5.11 is similar to the solution of Voller et al. (2004) depicted earlier in Figure 3.11b The key difference is that here a semi-infinite channel is considered, hence the depositional topset extends inland upstream of the origin. In practical applications, the solution could be used to predict the deposit volumes emplaced in three different locations: (1) into the lake and under water V_1; (2) into the lake but above the water level V_2 and (3) inside the alluvial channel upstream of the initial water edge V_3 for a length of channel L_c Fig 5.12.. Those three volumes are given respectively by the following expressions derived from geometric considerations:

The sediment volumes into the lake and under the water are given by

$$V_1 = 2\frac{RS}{R-S}\lambda^2\,Dt\ ,\ V_2 = 2\int_{o_1=0}^{s(t)}\sqrt{Dt}\,f(\sigma)\,dt\ , \tag{5.28a-b}$$

$$V_3 = 2\int_{-L_c}^{o_1=0}\sqrt{Dt}\,f(\sigma)\,dt - \frac{1}{2}L_c^2 S \tag{5.28c}$$

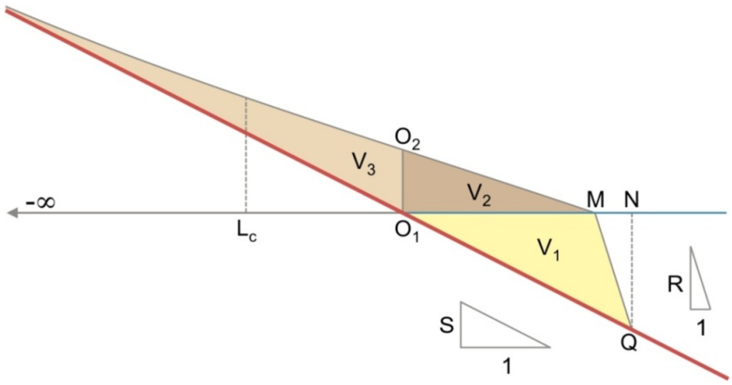

Figure 5.9: Similarity solution sediment volume: (V_1) sediment volume into the lake under the water level, (V_2) sediment volume into the lake above the water level and (V_3) sediment volume inside the channel.

In field conditions, however, various difficulties can be expected to arise. First, even when the valley is narrow and constrained laterally by bedrock walls, three dimensional patterns of water and sediment motion will influence the deposit shape. The photograph of Figure 1.3, for instance, showed an oblique delta front which will only be roughly approximated by the one dimensional theory. Natural deltas will further feature more complicated forests and bottomsets, alimented by richer process than the angle of repose avalanching assumed here (see e.g. Kostic and Parker, 2003).

5.4 Finite difference solution

To validate numerically the self-similar solution for the prograding sediment front in the flume, a simple finite difference method has been used. As this scheme is explicit, the well known CFL stability condition has been used with adaptation to the present case. The used method (Lai, 2006), is briefly described as follows:

First, the spatial domain $x_L \le x \le x_R$ is discretized into series of equally sized cells, at the limits of the cells bed elevations $z_{b_i}(t) = z_b(x_i, t)$ are sampled.

$$x_i = x_L + (i\text{-}1/2)\Delta x,\ i = 1,\ldots\ldots,\mathrm{I}, \qquad \mathrm{I} = \frac{x_R - x_L}{\Delta x} \tag{5.29}$$

Starting from imposed initial data, the bed elevation evolves in time using the explicit difference statement

$$z_{bi}(t+\Delta t) = z_{bi}(t) + \frac{1}{1-\varepsilon_0}\frac{\Delta t}{\Delta x}\left\{q_{s_{i-1/2}}(t) + q_{s_{i+1/2}}(t)\right\} \tag{5.30}$$

where $q_{s_{i+1}}$ is the bedload flux between cell *i* and cell *i+1*. This flux is determined using the following approximation (see relation 5.12)

$$q_{s_{i+1/2}} = D\, S_{i+1/2} \tag{5.31}$$

where

$$S_{i+1/2} = \frac{z_{b_i} - z_{b_{i+1}}}{\Delta x}, \tag{5.32}$$

The boundary conditions treatment is standard. Because the time-stepping is explicit, stability requires the adapted CFL conditions (Lai, 2006).

$$\Delta t \le \frac{(\Delta x)^2}{2\,D} \tag{5.33}$$

This limits the spatial resolution that can be attained at reasonable computational cost. In one spatial dimension, however, this limitation is not too severe and good accuracy is attained even with relatively coarse discretisation Δt = 0.0002s and Δx =1 cm.

Application example

Results of such analytical computation of prograding delta for a lake of constant level ($\mu = 0$) are plotted in Figures (5.11) and (5.12). The data are the following: unit discharge q = 0.027 m^3/s/m; Chezy coefficient $C = 50$; sediment density $s = 2.65$; porosity $\varepsilon_0 = 0.40$; initial slope $S = 0.0302$ and sediment front slope $R = 0.0005$.

It is possible to compute the solid discharge q_s according to (3.33), the diffusion coefficient D according to (3.35) and the scaling factor λ from the iterative formula (5.25) Fig.5.10:

-unit sediment discharge $q_s = 0.00021868$ m^3/s/m

-diffusion coefficient $D = 0.1214872$

-scaling factor $\lambda = 0.3255$

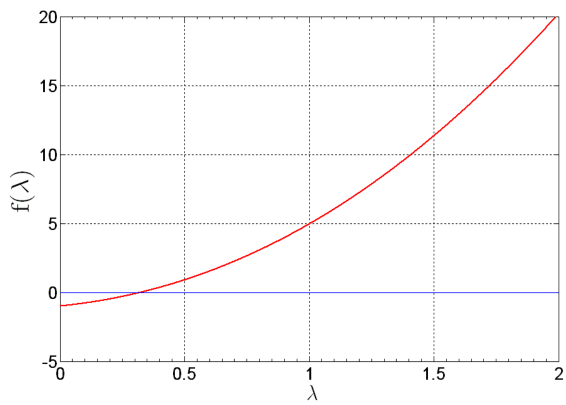

Figure 5.10: Transcendental equation for scaling factor vs scaling factor

The following Figure 5.11 presents the results of the analytical computation validated by a simple finite difference method, at times $t = 1$, 100, 200, 300, 400, 500 and 600s, the first one representative of the initial conditions.

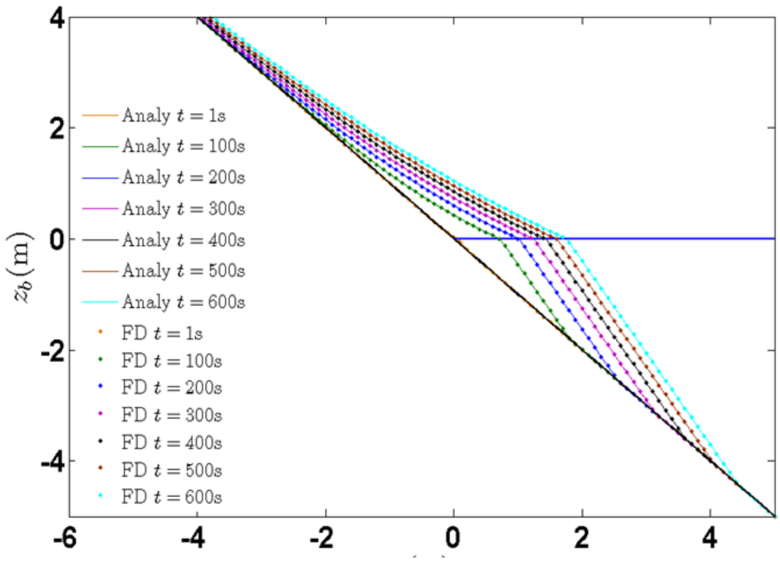

Figure 5.11: Prograding delta: analytical and finite differences results

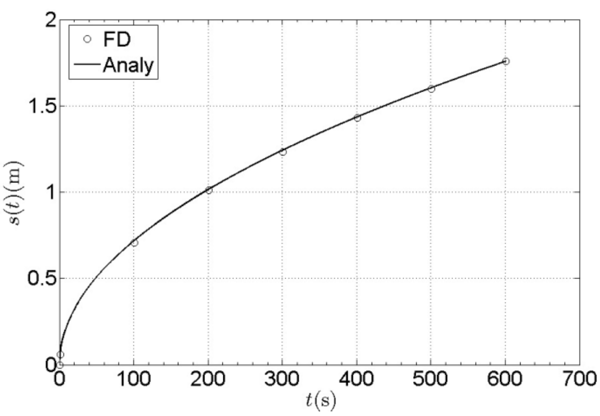

Figure 5.12: Path of prograding sediment front analytical (tick curve) and finite difference results (circles)

5.5 Numerical simulations

It has been seen that the SedRiv numerical model based on the implicit four-point scheme, used in chapter 4, to simulate the morphodynamics of steep sloped river beds in uniform supercritical flow, is not suitable for trancritcal flow. Then, a two-layer model developed by Capart (2000) and improved by Capart & Young (2002). Recently, accurate treatment of boundary conditions has been introduced by Savary (2007) in this model to simulate such transient fluvial flows.

5.5.1 Two-layer model

The flow is divided into two moving layers constituted of clear water and of a mixture of water and sediments respectively, (Figure 5.13). The main variables are the thickness of the water layer h_w and of the transport layer h_s, the velocities u_w and u_s in each layer, and the level of the interface between the transport layer and the fixed bed z_b. The transport layer and the fixed bed are constituted of a water-sediment mixture with sediment concentrations C_s and C_b respectively, assumed as constant in time and space. The volumetric density ρ_s' of this transport layer is $\rho_s' = (1 - C_s)\, \rho_w + C_s \rho_s$, where ρ_w and ρ_s are the water and grain density, respectively. The velocity in the transport layer u_s is allowed to be distinct from the velocity in the water layer u_w, both assumed to be uniform in their layer. Assuming a shallow-water hydrostatic pressure distribution, the two-layer model equations can be derived from mass (5.34 and 5.35) and momentum (5.37 and 5.38) conservation in each layer and from the definition of the erosion rate e_b (5.36). These equations read, in one-dimensional form:

$$\frac{\partial h_w}{\partial t} + \frac{\partial h_w u_w}{\partial x} = e_s \tag{5.34}$$

$$\frac{\partial h_s}{\partial t} + \frac{\partial h_s u_s}{\partial x} = e_b - e_s \tag{5.35}$$

$$\frac{\partial z_b}{\partial t} = - e_b \tag{5.36}$$

$$\frac{\partial h_w u_w}{\partial t}+\frac{\partial}{\partial x}\left(h_w u_w^2+\frac{1}{2}gh_w^2\right)+gh_w\frac{\partial(z_b+h_s)}{\partial x}=u_w e_s-\frac{\tau_{ws}}{\rho_w}$$

(5.37)

$$\frac{\partial h_s u_s}{\partial t}+\frac{\partial}{\partial x}\left(h_s u_s^2+\frac{1}{2}gh_s^2\right)+gh_s\frac{\partial}{\partial x}\left(z_b+\frac{\rho_w}{\rho_s'}h_w\right)=-\frac{\rho_w}{\rho_{s'}}u_w e_s+\frac{\tau_{ws}}{\rho_s'}-\frac{\tau_b}{\rho_s'}$$

(5.38)

where $e_b = -\partial z_b/\partial t$ and $e_s = -\partial(z_b + h_s)/\partial t$ depend on the shear stresses on both sides of the respective interface z_b and z_s and are related to each other:

$$e_b=\frac{\tau_s-\tau_b}{\rho'_s u_s} \tag{5.39}$$

The shear stress between the water and the transport layer τ_w and the shear stress applied on the fixed bed τ_s are assumed to follow a Chézy-like friction law:

$$\tau_w=\rho_w C_{f,w}\left|u_w-u_s\right|\left(u_w-u_s\right) \tag{5.40}$$

$$\tau_s=\rho'_s C_{f,s}\left|u_s\right|u_s \tag{5.41}$$

where $C_{f,w}$ and $C_{f,s}$ are water and sediment friction coefficients. These coefficients can be calibrated in uniform flow conditions for which the sediment discharge is in equilibrium (Zech et al., 2006).

The resistance shear stress to the flow, exerted by the fixed bed, is expressed by a Mohr–Coulomb relation.

$$\tau_b=\tau_{crit}+tg\varphi(\rho'_s-\rho_w)g\,h_s \tag{5.42}$$

where τ_{crit} is the threshold value of τ_s allowing erosion and φ is the angle of repose of the soil. A finite-volume approach is adopted to discretise the system. The proposed numerical results for comparison are inspired from Savary et al. (2006) and Goutière et al. (2009).

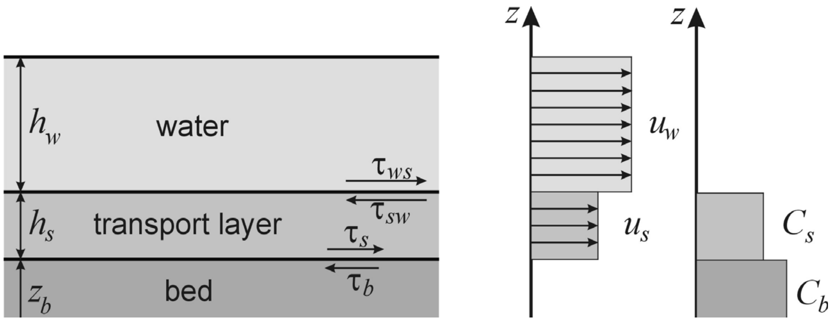

Figure 5.13: Two-layer model scheme

Results of the numerical computation of prograding sediment front for run#2, are obtained for the main parameters summarised in Table 5.1. Beside those parameters, the following data, Savary (2007), were necessary for the simulations: numerical domain length L = 6.9m; the water depth h_w= 0.031m; the friction coefficients C_{fw} = 0.015 and C_{fs} 0.11; the sediment concentration C_S and C_b =0.57.

The initial bed level $z_b(x, 0)$ is taken as the regression straight line through the experimental bottom level measurements, Fig. 5.14. A set of comparison results is given henceforward in Figs. 5.15 to 5.21.

5.6 Comparisons

The same conventions are adopted for plotting all Figures: time $t = 0$ corresponds to the abrupt rise of downstream water level; horizontal co-ordinates are in metres, origin placed at the upstream end of the flume; vertical co-ordinates are in metres above the bottom of the flume at the downstream end.

Example of measurement results are compared to self-similar and numerical results and are presented hereafter. Results include time evolution of water and bed prograding delta profiles and evolution in time of delta front position.

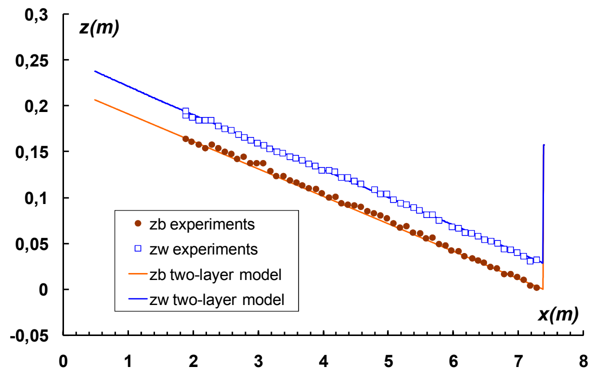

Figure 5.14: Experimental and two–layer model water and bed profiles (run #2) at time t=0s.

The conflict between the imposed subcritical condition downstream of the initial situation Fig 5.14 generates in the first stage a surge propagating upwards accompanied by humps as shown from the numerical simulation plotted in Figure 5.16.

The qualitative and quantitative comparisons between the numerical simulation and the few experimental results, Fig.5.16, obtained by digital imagery show their good agreement. Unfortunately, the analytical self-similar solution is not able to track the propagating wave of the first humps and therefore, comparisons are not of benefit. As mentioned already, the first stage of humps formation is relatively rapid and few bed profiles obtained by digital imagery are available. Those few measurements represent the existence of the deposition area under the surge Figs 5.3c to 5.3h.

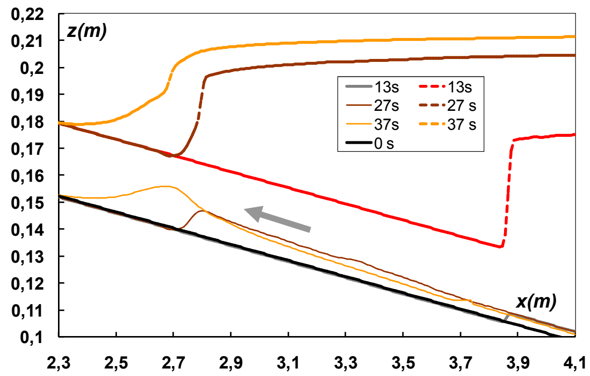

Figure 5.15: Humps propagations (run#2) two-layer results from Savary (2007)

Once the surge gets stabilized, all the sediments depose at the same place and form the sediment front propagating downwards. The experimental measurements of the sediment front are compared to the numerical results and to the present self-similar solution; Fig. 5.16 illustrates their good accordance. The experimental results are issued from digital imaging, explaining why they are limited to a window of 0.9 m.

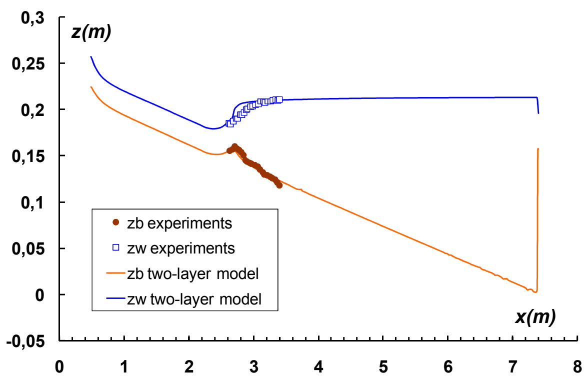

Figure 5.16: Comparison of measurements (from digital imagery) and two-layer water and bed profiles at time t=40s.

The results of the numerical modelling, Savary (2007), outline: (a) the first stage of bed deformation corresponding to the formation and propagation upwards of the humps is reproduced accurately Fig 5.15. Contrariwise to the self similar solution which is incapable to handle the wave of the humps; (b) for the second stage, corresponding to the sediment front formation, the two-layer model somewhat underestimates the height of the sediment front and overestimates its celerity of propagation comparatively to the experiments and the self-similar solutions. However, far upstream of the sediment front, the two-layer model seems to reproduce the experimental bed level better than the self-similar solution (Figs 5.17-5.20) and (c) the water level out of the transition area is also well reproduced by the numerical two-layer model.

In the transition region, the numerical hydraulic jump is sharper than the reality. This is caused by the limitation of a shallow-water model in handling the complex velocity distribution of a recirculation zone as shown in Figure 5.21.

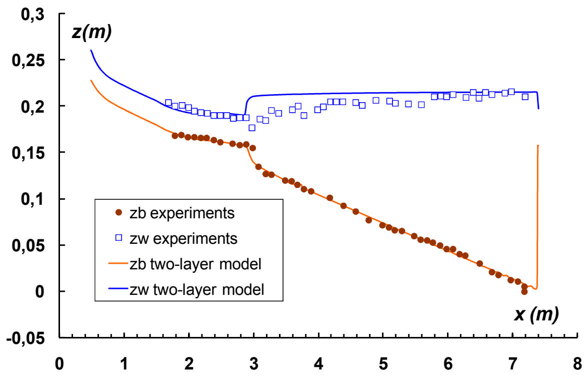

Figure 5.17: Comparison of measurements (run# 2) and numerical water and bed profiles at time t=65s.

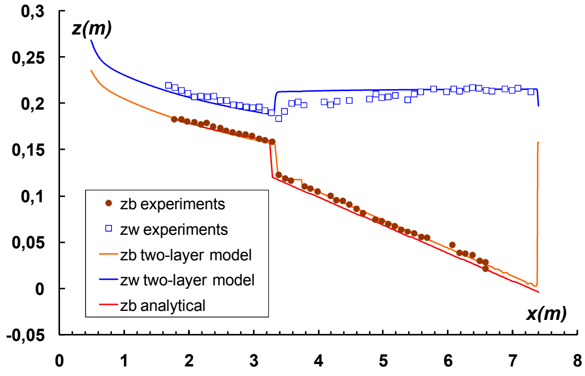

Figure 5.18: Comparison of measurements (run #2), two-layer and analytical water and bed profiles at time t=135s.

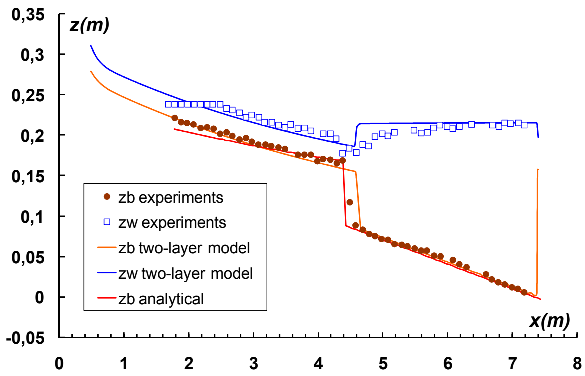

Figure 5.19: Comparison of measurements (run #2), two-layer and analytical water and bed profiles at time t=545s.

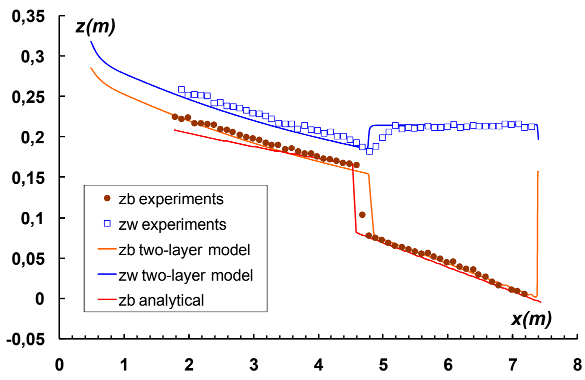

Figure 5.20: Comparison of measurements (run# 2) numerical and analytical water and bed profiles at time t=630s.

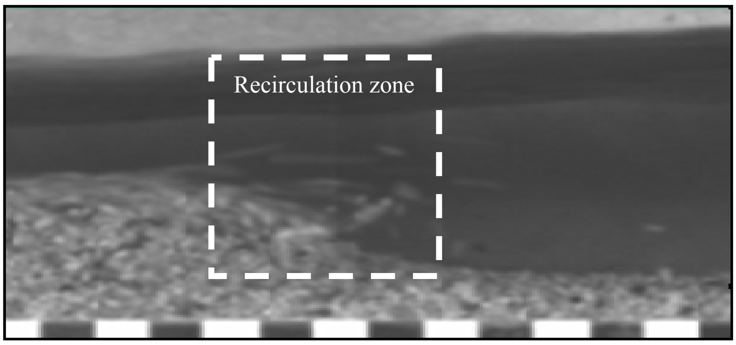

Figure 5.21: Sample image showing the recirculation zone in the transition near the sediment front (run # 2).

Previous comparaisons, Bellal et al. (2003), between a measured water profile at a particular instant 221s of run #2 were made with the theoretical water profiles obtained separately in the subcritical and supercritical regions, using a basic steady flow profile computation software AxeRiv and the measured bed elevations. Theoretical profiles compare favourably with the measurements except in the transition region. It can be observed that the formation of the sediment front influences the hydrodynamic evolution of the system in the following way: upstream of the sediment front, the S2 profile becomes a Su uniform profile and downstream of the front, a S1 profile develops. The junction between these two profiles is completed through a kind of inverse jump that propagates downwards with the sediment front. The transition of flow regime, initially beard by the hydraulic jump, is thus progressively taken over by the bed profile.

The presented experiments were also simulated by means of another numerical model developed by Leopardi (2001). It is based on an explicit predictor/corrector MacCormak scheme for the coupled resolution of the Saint-Venant-Exner equations. A part of these results is exposed in Bellal et al. (2005), but then, supplementary instabilities occur and the results are less convincing.

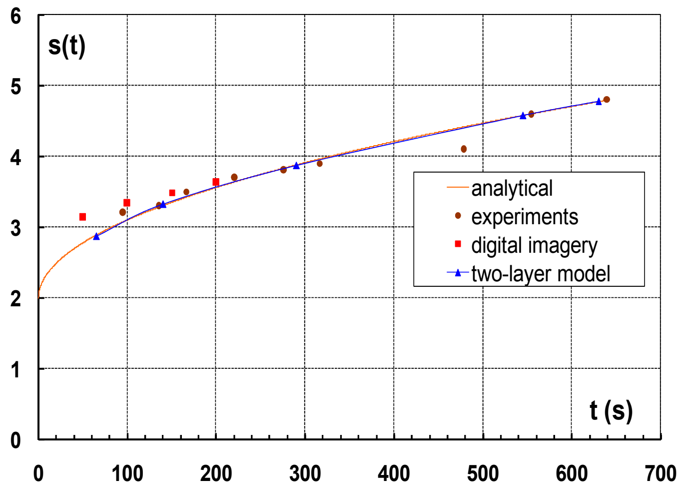

Figure 5.22: comparison of time evolution of sediment front path

Figure 5.22 shows the time evolution of the sediment front path. The propagation speed decreases slowly with time because the aggradational profile needs, each time, more sediment to form the rising height of the front. The comparisons illustrate a relative good agreement of measurements (obtained by a probe and digital imagery), with analytical and numerical computation, except in the early stage at t=50s, where the path deduced visually from the digital imagery profile, (Figure 5.3h), points up a small divergence with the self-similar and numerical paths.

5.7 Conclusions

Experiments were carried out in a laboratory flume to study the morphodynamic evolution of steep-sloped channels in the presence of a hydraulic jump created by a sudden rise of water level in the downstream section. Digital image sequences of the flow were acquired through the flume sidewalls, and probe measurements were performed to track the evolution of bed and water elevations with time. Two distinct stages of the bed evolution were identified: (1) propagation of a small sedimentation shock wave upstream at approximately the same speed than the hydraulic jump, and conversion of this wave into a steep sediment bore due to local deposits when the hydraulic jump stabilises; (2) development of the sediment bore in the downstream direction, associated with a progressive driving back and decrease in intensity of the hydraulic jump. The bed profile then progressively takes over the transition from supercritical to subcritical flow in a kind of inverse hydraulic jump.

A mathematical solution was derived for prograding sediment front. Although the proposed analysis reduces these phenomena to drastically simplified problem, the approach yields a number of benefits. First, an exact self-similar solution is obtained, free from the accuracy limitations of numerical calculations. Because the solution comes from a transparent analytical procedure instead of an algorithmic black box, it also provides a clearer view of the role of various boundary conditions and control parameters. Alternatively, the solution itself could be helpful for field events analyses, yielding typical time scales, modes of evolution, and distributions of deposit volumes once rough estimates of slopes and diffusion coefficients are available.

Results of simulations from Savary (2007) obtained by the two-layer model are used to illustrate the humps formation, their propagations and the prograding sediment front. The two-layer model confirmed the theoretical analysis of Sieben (1996) and our experimental observations, Bellal et al. (2003).

In general, the comparisons between experimental, analytical and numerical approaches show their satisfactorily agreement.

Chapter 6

Fluvial morphodynamics in transcritical flow over mobile bed: Knickpoint and critical section

6.1 Introduction

Knickpoints are sections of longitudinal profile of streams, at which the slope abruptly increases. Field observations and laboratory experiments (Brush and Wolman, 1960) suggest that these sharp slope breaks can preserve their identity even as they migrate upstream under retrogressive erosion. The resulting river profile evolution is important to engineers because incision can destabilize bridge piers or other structures.

Several knickpoint configurations exist in nature (Brush and Wolman, 1960) and are controlled mainly by the bed erodibility and hydraulic conditions. Erodibility defines the resistance of the soil to detachment and transport. It depends to some extent on hydraulic conditions, slope steepness, sediment characteristics, etc. So, a knickpoint in a channel in which no material is being transported remains fixed indefinitely. In a stream with easily erodible material, the knickpoint will be obliterated rapidly. In the field (Fig. 6.1), knickpoints exist at all stages between these extremes.

Figure 6.1: Knickpoint migration in a long channel

In the present study, we consider the simplified case of a channel bed composed of cohesionless sand, where the bed slope evolves from mild to steep, with a corresponding transition in the flow regime from subcritical to supercritical flow. From a morphodynamic perspective, this corresponds to a “control section” propagating upstream due to regressive erosion (Fig. 6.9).

Brush and Wolman (1960) explained the migration of the knickpoint as a result of the increased erosion potential at the slope break. On the upstream side of the knickpoint, where the energy grade line flattens, the bed shear stress is low although the flow depth is higher. Then, at the slope break, the bed shear stress increases rapidly. Since the sediment transport is directly proportional to the bed shear stress, it results in more material being carried downstream than supplied upstream. Therefore, the knickpoint migrates upstream, the eroded material is carried out downwards, and finally the steep sloped reach flattens.

The knickpoint study has long been of interest to engineers and geologists. Numerous field observations have been made on position and geological environment of knickpoints. From an engineering standpoint, it is interesting to attempt to well understand the transition of the flow regime and the related propagation of the erosion front. In previous work (Savary et al., 2006), knickpoint migration has been simulated using a two-layer shallow water numerical model. In the present chapter, we test whether the phenomenon could be modelled also using a simpler diffusion approach, treating the knickpoint as a moving internal boundary. For problems with fixed boundaries, the diffusion approach was pioneered by de Vries (1973), Soni et al. (1980) and Begin et al. (1981). More recently, moving boundary problems have been solved analytically for various alluvial phenomena, including prograding deltas (Voller et al., 2004, Lai and Capart, 2007), migrating bedrock-alluvial transitions (Capart et al., 2007, Lai and Capart, 2009) and the formation of tributary-dammed lakes (Hsu and Capart, 2008). Governing equations similar to those adopted here to treat terrestrial knickpoints were earlier applied by Mitchell (2006) to knickpoints in submarine canyons.

The analytical self-similar solution of the diffusion equation presented in this chapter is compared to experimental measurements, a finite-difference discretization of the diffusion equation and two-layer model simulations.

6.2 Experiments of knickpoint and critical section

6.2.1 Description

A control section over an erodible bed with slope discontinuity has been experimented using a sediment flume facility built at the Civil Engineering Laboratory of the Université Catholique de Louvain. The experiments represent the transition from subcritical flow (water profile M2) over mild bed slope to supercritical flow (water profile S2) over steep slope through a control section. Figs. 6.9a. and 6.9b. The experimental set-up is represented in (Fig. 2.1).

6.2.2 Experimental procedure

Experiments were carried out in the following sequence (Bellal et al., 2004):

(1) The knickpoint is pre-formed, with a slope transition from mild to steep. The initial position is located about 100cm from downstream; the upstream and downstream initial slopes are S_1 and S_2 respectively;

(2) The sediment bed is saturated with a small liquid discharge;

(3) Afterwards, the liquid discharge is increased progressively up to the expected value; no sediment supply is provided upstream.

An erosion recession propagates upwards, starting from the initial knickpoint location. As a result, the modified sediment transport capacities initiate morphological evolution of the bed profile. The downstream bed level is assumed to be fixed. The knickpoint decreases in amplitude and progressively vanishes as the supercritical flow takes place over subcritical flow.

The measurement of the water surface and bed profiles has been done at regular time intervals by means of two probes mounted on a trolley pulled alternately in the upstream and downstream directions. Several experiments were performed within the following ranges of initial parameters reported in Table 6.1.

Test #	Q(l/s)	S_1^{ini} %	S_2^{ini} %
Run 1	4.90	0.4	2.02
Run 2	6.15	0.47	2.03
Run 3	7.33	0.45	2.00
Run 4	5.01	0.42	3.02
Run 5	6.18	0.44	5.03
Run 6	4.97	0.10	5.00
Run 7	7.33	0.40	3.00
Run 8	5.00	0.40	5.00
Run 9	6.00	0.40	3.00
Run 10	7.00	0.40	3.00
Run 11	7.00	0.40	5.00

Table 6.1: Main experimental initial parameters

It can be seen that upstream slope S_1 ranged around 0.4%, while downstream slope S_2 from 2% to 5%, liquid discharge from 4.9 to 7.50 l/s. The other parameters for the tests are the following: channel length $L = 6.90$ m; width $b = 0.50$ m; bed roughness $n_b = 0.0165$; wall roughness $n_w = 0.0195$.

Initial Froude numbers ranged from $\mathrm{Fr}_0^{up} = 0.7$ to 0.9 (upstream of the knickpoint) and $\mathrm{Fr}_0^{dwn} = 1$ to 1.24 (downstream of the knickpoint); after the development of the erosion front and a total migration of the knickpoint, Froude numbers became close to the unity.

For qualitative illustration, the sidewall digital images during run#1 are plotted in the following Figures at various times. Fig. 6.2 refers to the initial conditions: (i) preformed knickpoint and (ii) regime flow. The erosion front and the upwards knickpoint migration is depicted in Fig 6.3.

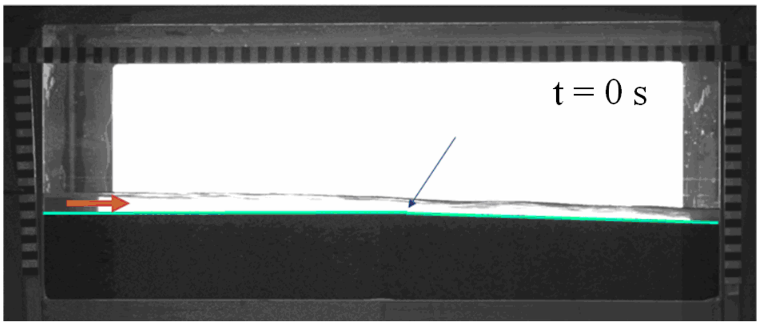

Figure 6.2: Sample digital image showing the initial bed profile with a Knickpoint (upstream on the left side). Time t = 0 s (run #1, intervals on horizontal and vertical axes are 1cm.

(a)

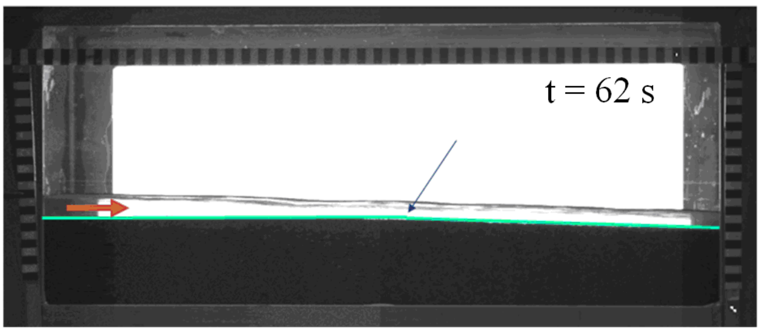

(b)

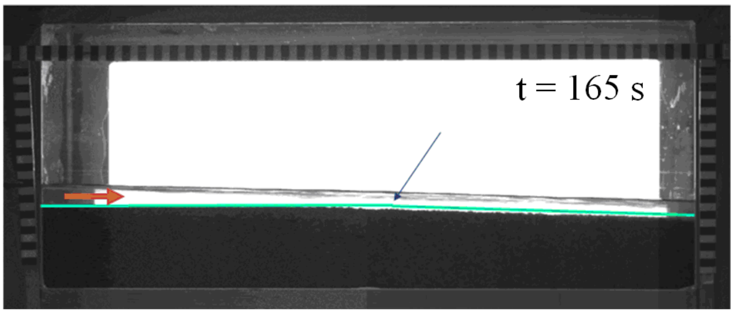

(c)

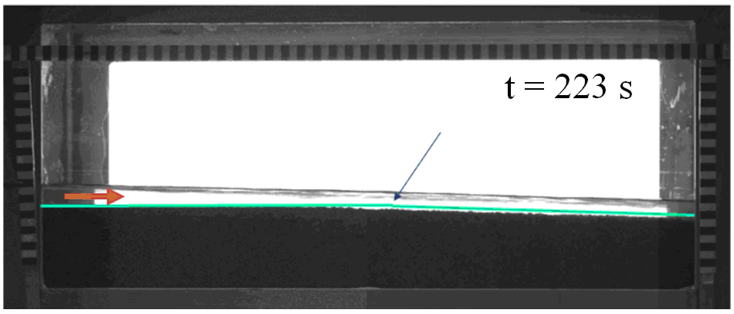

(d)

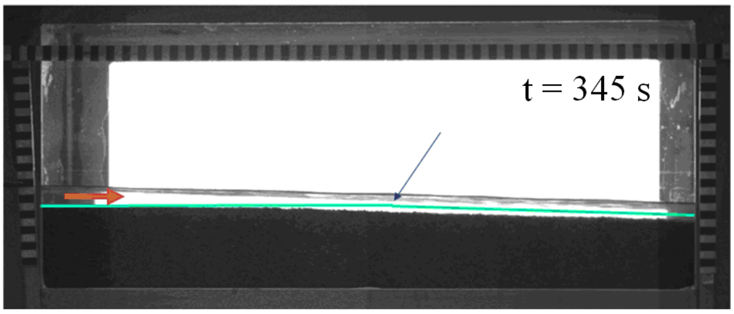

Figure 6.3: Sample digital images showing the initial bed profile with a knickpoint (upstream on the left side). Time evolution (t = 62 s-345 s) (run# 1), intervals on horizontal and vertical axes are 1cm.

Figs. 6.5 and 6.6 show an example of water and bed profile evolution. The regressive erosion is starting from the initial situation Fig. 6.4 is clearly visible. The downstream end of the upstream reach is receding while the upstream reach seems unaffected. The water profile confirms the control exerted by the knickpoint on the flow regime.

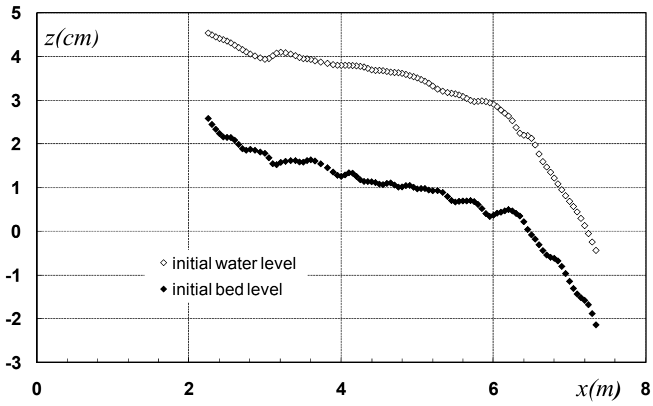

Figure 6.4: Initial experimental water and bed profiles

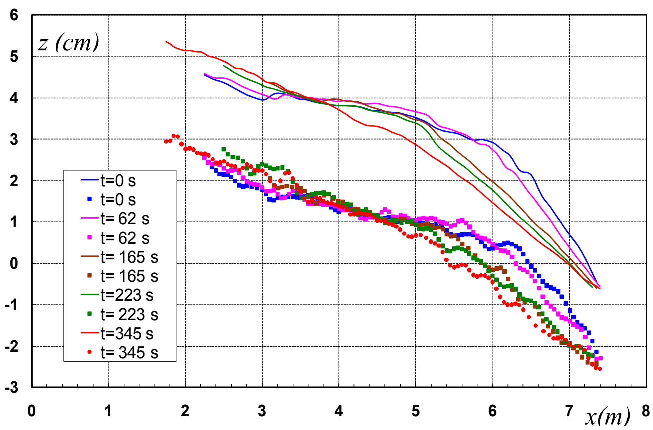

Figure 6.5: Experimental knickpoint evolution(run #1).

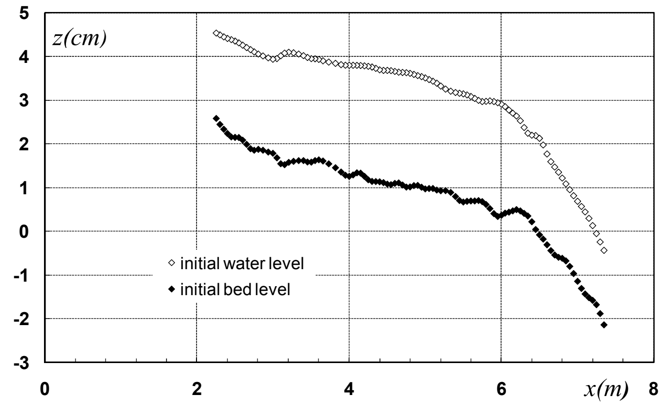

Figure 6.6: Final stage: water and bed profiles at 2733s(run #1)

The bed slope evolution downstream and upstream of the knickpoint, as a function of time for three performed runs (run# 1, run# 3 and run# 4), is illustrated in Fig. 6.7. The average bed slope upstream the knickpoint is still unchanged, except a slight adaptation in the beginning of the tests, while the bed slope downstream of the knickpoint was subject of substantial changes. The progressive knickpoint propagation may be clearly observed. Progressive degradation wave described previously extends in the upstream direction, causing further decrease of the bed levels in the supercritical reach, while the average upstream bed slope is still unaffected. As this degradation develops, the slope of the channel in this region is reduced and tends to an equilibrium value at the end of the test.

In our experimental tests, we can distinguish two different stages of bed evolution: the first stage is characterized by a progressive knickpoint migration accompanied with the critical section and the increase in sediment transport during the migration of the knickpoint, once the knickpoint collapses; the second stage is a simple degradation front and features an asymptotic evolution of the bed slope towards an equilibrium state in which the final slope S^{∞} is adjusted to the stream power. From the comparison of the various runs, we can monitor that both water discharge and the initial bed slope downstream of the knickpoint have significant effect on the bed slope evolution, while the initial upstream slope has more effect on the first stage of the downstream bed slope evolution. As expected the increase of liquid discharge from 4.9 (l/s) run #1 to 7.33 (l/s) run #3 produces more effect on bed slope evolution downstream.

This evolution is well marked when the initial bed slope is increased from 2.00 (%) run #3 to 3.02 (%) run #4. In spite of that, the liquid discharge is decreased to 5 (l/s). Finally, we notice that the downstream bed slope decrease rapidly in the beginning of the tests and the possible use of the digital imaging system to monitor this first stage would be an advantage.

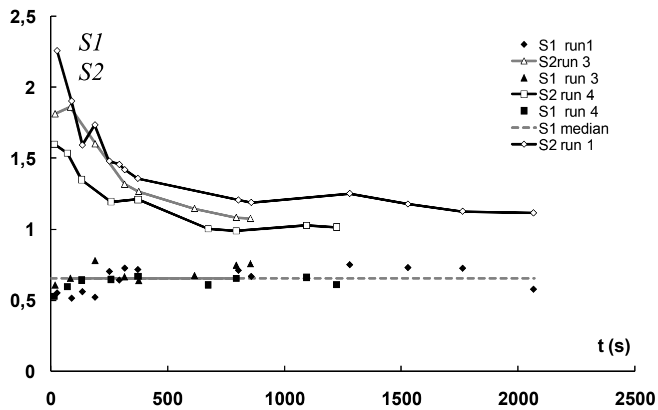

Figure 6.7: Time evolution of average bed slope upstream and downstream of the knickpoint (run #1, 3 and 4)

Fig.6.8 highlights the time evolution of the knickpoint position of different runs # 1, 2, 3 and 4. The propagation speed slowly decreases with time because the slope downstream of the knickpoint decreases and thus the bed shear stress and the solid discharge at the knickpoint decreases too.

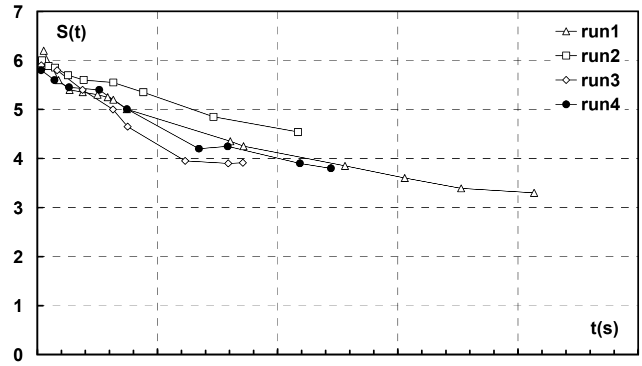

Figure 6.8: Time evolution of knickpoint position. (runs #1,2,3 and 4)

6.3 Self-similar solution for knickpoint migration

Based on the recent work of Capart et al. (2007), the present chapter proposes an analytical solution to the migrating knickpoint, treated as a moving boundary problem (Bellal et al., 2009). Hereafter, the idealized case of an infinite channel is first considered. Then the solution is particularized to a channel of fixed length, i.e. a more realistic case with fixed upstream and downstream boundary conditions.

6.3.1 Kinckpoint migration in infinite channel

Refer to Fig. 6.9: an alluvial channel of infinite length with initial slopes S_1 upstream and S_2 downstream:

$$z_b(x,0) = \begin{cases} -S_1 x, & -\infty < x < 0 \\ -S_2 x, & 0 \le x < \infty \end{cases} \tag{6.1}$$

the origin of co-ordinates x and z being the initial position of the knickpoint.

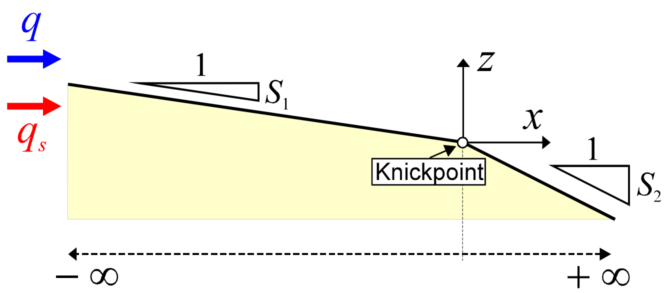

Figure 6.9a: Knickpoint in infinite channel: initial condition

Assume that the initial upstream and downstream slopes are respectively milder and steeper than the slope threshold, i.e:

$$S_1 < S_{\min} < S_2 \tag{6.2}$$

where $S_{\min}$ is the minimum bed slope where sediment transport initiates. So, the downstream reach is erodible while the upstream reach not. An erosion front forms at the change in slope and propagates upwards. Due to regressive erosion (Fig. 6.9b.), the knickpoint moves upwards at the position $x = s(t) < 0$. The upstream slope does not evolve as long as the regressive erosion has not reached the considered section. So, the diffusion equation (3.34) has to be solved only downstream of the knickpoint:

$$\frac{\partial z_b}{\partial t} = D\,\frac{\partial^2 z_b}{\partial x^2}\,,\ \text{for}\ x \geq s(t) \tag{6.3}$$

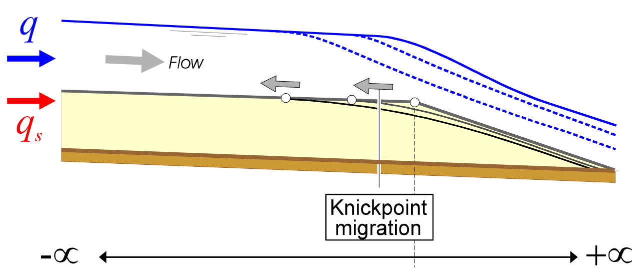

Figure 6.9b.: Knickpoint migration

It is assumed that the water depth (assumed as steady uniform) in both reaches is small enough to be neglected, such that water profile is assumed to coincide with bottom profile. In order to ensure the similarity, the knickpoint location $s(t)$ is assumed to be scaled by the function $\xi(t)$, which implies

$$s(t) = \lambda\, \xi(t) = 2\, \lambda \sqrt{D\, t} \tag{6.4}$$

where λ is a scaling constant to be determined as a part of the solution.

The boundary conditions are the following. Far downstream, the profile slope must converge to the initial downstream slope S_2. At the migrating knickpoint $x = s(t)$, two conditions must be met. First, the profile elevation must be continuous across the knickpoint. Secondly, the slope immediately downstream of the knickpoint must reach S_{min} for initiating sediment transport and diffusion to become activated. Translated in mathematical form, these three conditions yield

$$\frac{\partial z_b}{\partial x} = -S_2 \quad \text{at} \quad x = +\infty \tag{6.5}$$

$$z_b\left[s(t), t\right] = -S_1\, s(t) \quad \text{at} \quad x = s(t) \tag{6.6}$$

$$\frac{\partial z_b}{\partial x}\left[s(t), t\right] = -S_{\min} \quad \text{at} \quad x = s(t) \tag{6.7}$$

Using the formulation (3.44-3.45)

$$z_b(x, t) = \mathrm{f}(\sigma)\, \xi(t) = 2\sqrt{Dt}\; \mathrm{f}(\sigma) \tag{6.8}$$

with $\mathrm{f}(\sigma)$ expressed on the form (3.71) where arbitrary constant C of (3.68) has been chosen equal to –1:

$$\mathrm{f}(\sigma) = A'\sigma + B'\left[\frac{e^{-\sigma^2}}{\sqrt{\pi}} + \sigma\left[\operatorname{erf}(\sigma) - 1\right]\right] \tag{6.9}$$

The derivative of $\mathrm{f}(\sigma)$ writes

$$f'(\sigma) = A' + B'\left\{ \frac{e^{-\sigma^2}}{\sqrt{\pi}}(-2\sigma) + \left[\operatorname{erf}(\sigma) - 1\right] + \sigma\left[\frac{\partial}{\partial\sigma}\operatorname{erf}(\sigma)\right]\right\}$$

$$= A' + B'\left\{ \frac{e^{-\sigma^2}}{\sqrt{\pi}}(-2\sigma) + \left[\operatorname{erf}(\sigma) - 1\right] + \sigma\left[\frac{2}{\sqrt{\pi}}e^{-\sigma^2}\right]\right\}$$

$$= A' + B'\left[\operatorname{erf}(\sigma) - 1\right] \tag{6.10}$$

Since

$$\sigma = \frac{x}{2\sqrt{Dt}} \tag{6.11}$$

$$\frac{\partial z_b}{\partial x} = \frac{\partial}{\partial x}\left[2\sqrt{Dt}\ f(\sigma)\right] = \frac{\partial}{\partial \sigma}\left[2\sqrt{Dt}\ f(\sigma)\right]\frac{\partial\sigma}{\partial x} = f'(\sigma) \tag{6.12}$$

boundary condition (6.5) at $x = +\infty$ yields

$$A' = -S_2 \tag{6.13}$$

while boundary condition (6.6) at the knickpoint $x = s(t) = 2\lambda\sqrt{Dt}$ writes

$$\frac{z_b(s,t)}{2\sqrt{Dt}} = f(\lambda) = -S_2\,\lambda + B'\left\{\frac{e^{-\lambda^2}}{\sqrt{\pi}} + \lambda\left[\operatorname{erf}(\lambda) - 1\right]\right\} = -S_1\frac{s}{2\sqrt{Dt}} = -S_1\,\lambda \tag{6.14}$$

yielding

$$B' = \frac{\sqrt{\pi}\,\lambda\,(S_2 - S_1)}{e^{-\lambda^2} + \sqrt{\pi}\,\lambda\left[\operatorname{erf}(\lambda) - 1\right]} \tag{6.15}$$

Using (6.10) and (6.12) and introducing the results (6.13) and (6.15), the third condition (6.7) writes

$$\frac{\partial z_b}{\partial x}\left[s(t),t\right] = A' + B'\left[\operatorname{erf}(\lambda)-1\right]$$

$$= -S_2 + \frac{\sqrt{\pi}\,\lambda\,(S_2 - S_1)}{e^{-\lambda^2} + \sqrt{\pi}\,\lambda\left[\operatorname{erf}(\lambda)-1\right]}\left[\operatorname{erf}(\lambda)-1\right]$$

$$= -S_{\min} \tag{6.16}$$

yielding a transcendental equation for the scaling constant λ:

$$\frac{\sqrt{\pi}\,\lambda\left[\operatorname{erf}(\lambda)-1\right]}{e^{-\lambda^2} + \sqrt{\pi}\,\lambda\left[\operatorname{erf}(\lambda)-1\right]} = \frac{S_2 - S_{\min}}{S_2 - S_1} \tag{6.17}$$

Knowing λ, it is now possible to compute $z_b(x,t)$ from (6.8), (6.9), (6.13) and (6.15):

$$z_b(x,t) = 2\sqrt{Dt}\ \mathrm{f}(\sigma)$$

$$= 2\sqrt{Dt}\left\{A'\sigma + B'\left[\frac{\mathrm{e}^{-\sigma^2}}{\sqrt{\pi}} + \sigma\left[\operatorname{erf}(\sigma)-1\right]\right]\right\}$$

$$= 2\sqrt{Dt}\left\{-S_2\,\sigma + \frac{\sqrt{\pi}\,\lambda\,(S_2 - S_1)}{e^{-\lambda^2} + \sqrt{\pi}\,\lambda\left[\operatorname{erf}(\lambda)-1\right]}\left[\frac{\mathrm{e}^{-\sigma^2}}{\sqrt{\pi}} + \sigma\left[\operatorname{erf}(\sigma)-1\right]\right]\right\}$$

$$= 2\sqrt{Dt}\left\{-S_2\,\sigma + (S_2 - S_1)\lambda\ \frac{\mathrm{e}^{-\sigma^2} + \sqrt{\pi}\,\sigma\left[\operatorname{erf}(\sigma)-1\right]}{e^{-\lambda^2} + \sqrt{\pi}\,\lambda\left[\operatorname{erf}(\lambda)-1\right]}\right\}$$

$$= -S_2\,x + 2\sqrt{Dt}\,(S_2 - S_1)\lambda\ \frac{\mathrm{e}^{-\sigma^2} + \sqrt{\pi}\,\sigma\left[\operatorname{erf}(\sigma)-1\right]}{e^{-\lambda^2} + \sqrt{\pi}\,\lambda\left[\operatorname{erf}(\lambda)-1\right]} \tag{6.18}$$

with

$$\sigma = \frac{x}{2\sqrt{Dt}} \tag{6.19}$$

Application example

Fig. 6.10 presents the result of such a computation of knickpoint migration in an infinite channel. The data are the following: unit discharge q = 0.0098 m^3/s/m; Chezy coefficient $C = 50$; sediment density $s = 2.65$; porosity $\varepsilon_0 = 0.40$; initial slope upstream $S_1 = 0.005526$; initial slope downstream $S_2 = 0.022588$ and slope corresponding to initiation of movement: $S_{min} = 0.01$.

It is possible to compute the solid discharge q_s according to (3.33) and the diffusion coefficient D according to (3.35), the scaling factor λ of the similarity solution from the iterative formula (6.17), and the constants A' and B' from (6.13) and (6.15):

-unit sediment discharge q_s = 0.0000673 m^3/s/m

-diffusion coefficient D = 0.00496 m²/s

-scaling factor $\lambda = -0.642240842$

-constants $A' = -0.022588$ and $B' = -0.00769314$

Fig. 6 presents the results at times t = 1, 100, 200 and 400 s, the first one representative of the initial conditions.

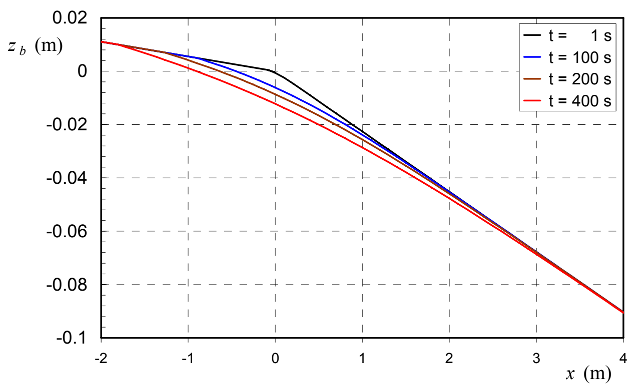

Figure 6.10: Knickpoint migration in an infinite channel: analytical results

6.3.2 Knickpoint migration in finite channel

The knickpoint will occur now in a channel of finite extent $x \le x_R$, where x_R is the position of the right boundaries (Fig. 6.11). In that case, let us assume that the channel starts from the following initial conditions:

$$z_b(x,0) = \begin{cases} z_0 - S_1\,(x - x_0), & x \le x_0 \\ z_0 - S_2\,(x - x_0), & x_0 < x \le x_R \end{cases} \tag{6.20}$$

where (x_0, z_0) is the initial position of the knickpoint and where we assume like before, that the initial upstream and downstream slopes are respectively milder and steeper than the slope threshold S_{min}:

$$S_1 < S_{\min} < S_2 \tag{6.21}$$

Unlike the previous infinite channel case, we assume that the bed elevation downstream is controlled by a rigid sill at (x_R, z_R), where the elevation is

$$z_R = z_0 - S_2\,(x_R - x_0) \tag{6.22}$$

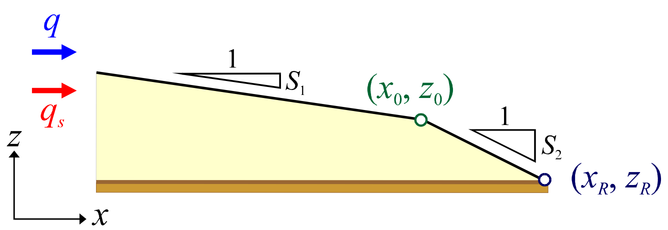

Figure 6.11: Knickpoint in finite channel: initial condition

An inner boundary condition has to be imposed at the knickpoint location $x = x_0 + s(t)$, $s(t)$ being the knickpoint (negative) shifting from its initial location. At this point, the same two conditions as formerly must be met. First, the profile elevation must be continuous across the knickpoint. Secondly, the slope immediately downstream of the knickpoint must reach $S_{\min}$ for diffusion to become activated:

$$z_b\left[x,t\right] = z_0 - S_1\left(x - x_0\right) = z_0 - S_1\,s(t) \quad \text{at} \quad x = x_0 + s\left(t\right) \tag{6.23}$$

$$\frac{\partial z_b}{\partial x}\left[x,t\right]=-S_{\min} \quad \text{at} \quad x=x_0+s\left(t\right) \tag{6.24}$$

As formerly, in order to ensure the similarity, the knickpoint displacement $x - x_0 = s(t)$ is assumed to be scaled by the function $\xi\,(t)$, which implies

$$s(t)=\lambda\,\xi\left(t\right)=2\,\lambda\sqrt{D\,t} \tag{6.25}$$

where λ is the scaling constant.

The proposed strategy is the following:

Step 1*:* starting from the similarity solution of infinite-channel case, which satisfies the conditions (6.23) and (6.24) at the knickpoint but not the downstream condition (6.22);

Step 2: correcting this solution in such a way that the downstream condition (6.22) be fulfilled, but with a slight deterioration of conditions (6.23) and (6.24) at the knickpoint;

Step 3: forcing the knickpoint continuity (6.23) by cutting the solution of the former step with a minimum function.

For very short times, the influence of the outer boundaries will not yet have been felt in the vicinity of the initial knickpoint position and the similarity solution of the previous section can be applied ***(step 1).***

Gradually, however, this similarity solution will cause a downstream channel incision that is incompatible with the rigid control at $x = x_L$. This is illustrated in Fig. 6.12a where the blue curve is the bed profile computed from the similarity solution of the infinite-length case. This profile reaches the downstream end of the channel below the weir crest elevation.

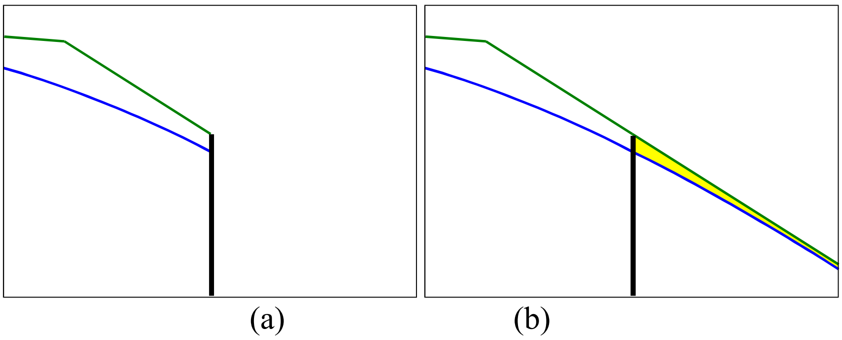

Figure 6.12: Knickpoint in finite channel: computation according to infinite-length case

If we now extend the computation over the downstream end of the channel Fig. 6.12b., the erosion profile represented in yellow features on the left an incision equal to the over-deepening at the sill and on the right, an incision close to zero.

If we draw the mirrored incision profile Fig. 6.13 centered about an imaginary second knickpoint located on the other side of the sill (using the image method), the orange erosion depth could be considered as an adequate correction to the similarity solution, moving the blue profile to the red one Fig. 6.14, which reaches the downstream end of the finite channel at the right level, the weir crest level (step 2).

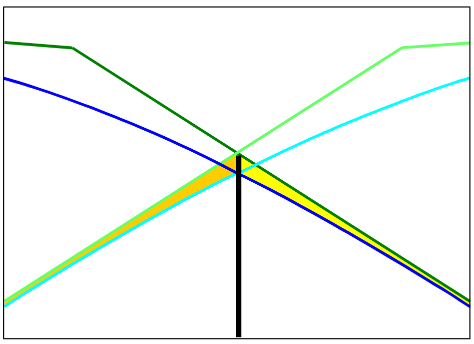

Figure 6.13: Knickpoint in finite channel: mirrored similarity solution

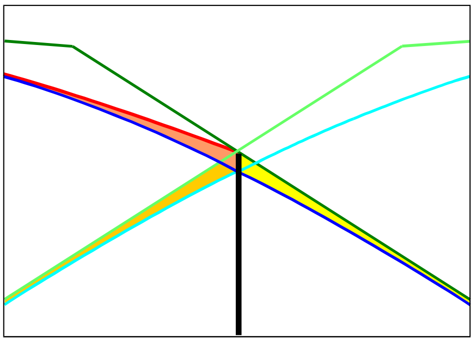

Figure 6.14: Knickpoint in finite channel: corrected solution

The similarity solution of step 1 $z_{b,1}$ (the dark blue curve of (Fig. 6.12) is similar to (6.18) with the difference that the initial knickpoint location is now (x_0, z_0), which implies to replace x by $(x - x_0)$ and z by $(z - z_0)$:

$$\begin{aligned} z_{b,1}(x,t) - z_0 &= 2\sqrt{Dt}\ \mathrm{f}(\sigma) \\ &= 2\sqrt{Dt}\left\{A'\sigma + B'\left[\frac{\mathrm{e}^{-\sigma^2}}{\sqrt{\pi}} + \sigma[\mathrm{erf}(\sigma) - 1]\right]\right\} \\ &= -S_2(x - x_0) + 2\sqrt{Dt}\ B'\ \mathrm{ierfc}(\sigma) \\ &= -S_2(x - x_0) + 2\sqrt{Dt}\,(S_2 - S_1)\,\lambda\,\frac{\mathrm{e}^{-\sigma^2} + \sqrt{\pi}\,\sigma[\mathrm{erf}(\sigma) - 1]}{e^{-\lambda^2} + \sqrt{\pi}\,\lambda[\mathrm{erf}(\lambda) - 1]} \end{aligned} \tag{6.26}$$

with
$$\sigma = \frac{x - x_0}{2\sqrt{Dt}} \tag{6.27}$$

and the function ierfc as defined in (3.72).

The last term of (6.26) $2\sqrt{Dt}\ B'\ \mathrm{ierfc}(\sigma)$ is negative ($B' < 0$, $\mathrm{ierfc} \geq 0$) and represents the incision depth of the similarity solution, the yellow area of Fig. 6.14.

The initial position of the fictitious symmetrical knickpoint O' is the following:

$$x_{0'} = x_R + (x_R - x_0) = 2\,x_R - x_0 \tag{6.28}$$

So the incision due to this imaginary knickpoint (the difference between the light green initial position and the light blue similarity solution in Fig. 6.14) reads

$$\begin{aligned}\Delta z_b(x,t) &= 2\sqrt{Dt}\;B'\left[\frac{\mathrm{e}^{-(\sigma')^2}}{\sqrt{\pi}} + \sigma'[\operatorname{erf}(\sigma')-1]\right]\\ &= 2\sqrt{Dt}\;B'\;\operatorname{ierfc}(\sigma')\\ &= 2\sqrt{Dt}\;(S_2 - S_1)\lambda\;\frac{\mathrm{e}^{-(\sigma')^2} + \sqrt{\pi}\,\sigma'[\operatorname{erf}(\sigma')-1]}{e^{-\lambda^2} + \sqrt{\pi}\,\lambda\,[\operatorname{erf}(\lambda)-1]}\end{aligned} \tag{6.29}$$

with $$\sigma' = \frac{x_{0'} - x}{2\sqrt{Dt}} = \frac{2\,x_R - x_0 - x}{2\sqrt{Dt}} \tag{6.30}$$

Subtracting (6.29) from (6.26) yields the corrected solution of *step 2*:

$$\begin{aligned}z_{b,2}(x,t) &= z_{b,1}(x,t) - \Delta z_b\\ &= z_0 - S_2(x-x_0) + 2\sqrt{Dt}\,B'\;\operatorname{ierfc}\left(\frac{x-x_0}{2\sqrt{Dt}}\right) - 2\sqrt{Dt}\,B'\;\operatorname{ierfc}\left(\frac{2x_R - x_0 - x}{2\sqrt{Dt}}\right)\end{aligned} \tag{6.31}$$

This solution, for $x = x_R$ leads to

$$z_{b,2}(x_R,t) = z_0 - S_2(x - x_0) = z_0 - S_2(x_R - x_0) \tag{6.32}$$

as $\sigma = \sigma'$ for $x = x_R$. Relation (6.32) is nothing else than the downstream boundary condition (6.22) imposing the weir crest as downstream level. On the other hand, for $x = x_0 + s(t)$, at the knickpoint, the continuity equation condition (6.23) is not anymore fulfilled, since the similarity solution $z_{b,1}$ matched this condition (6.23) and correction (6.29) is not zero and thus spoils this fulfilment. However, as Δz_b is rather small for higher values of σ', it seems sufficient to cut this correction where this would lead to a higher value than the upstream initial slope. So the final (step 3) value reads

$$z_{b,3}(x,t) = \min\left\lfloor z_{b,2}\,,\, z_0 - S_1(x - x_0)\right\rfloor \tag{6.33}$$

which automatically fulfils the continuity (6.23) at the knickpoint, but slightly violate the slope condition (6.24). Also the knickpoint location

$$x = x_0 + s(t) = x_0 + 2\,\lambda\sqrt{D\,t} \tag{6.34}$$

is only an approximation of the actual location. The accuracy gradually deteriorates with time advance.

Application example

An example of such a computation of knickpoint migration in a finite channel is presented hereafter. The data are the following: unit discharge q = 0.0098 m^3/s/m; Chezy coefficient $C = 50$; sediment density $s = 2.65$; porosity $\varepsilon_0 = 0.40$; initial slope upstream $S_1 = 0.005$; initial slope downstream $S_2 = 0.05$; slope corresponding to initiation of movement: $S_{\min} = 0.01$; initial position of the knickpoint $(x_0, z_0) = (4, 0)$ and position of the downstream weir crest $(x_R, z_R) = (7, -0.15)$.

It is possible to compute the solid discharge q_s according to (3.33) and the diffusion coefficient D, according to (3.35), the scaling factor λ of the similarity solution from the iterative formula (6.17), and the constants A' and B' from (6.13) and (6.15):

-unit sediment discharge q_s = 0.0001488 m^3/s/m

-diffusion coefficient $D = 0.00496$ m²/s

-scaling factor $\lambda = -0.967445$

-constants $A' = -0.05$ and $B' = -0.0218715$

Fig. 6.15a presents the results at times $t = 1$, 200, 400 and 800 s, the first one representative of the initial conditions.

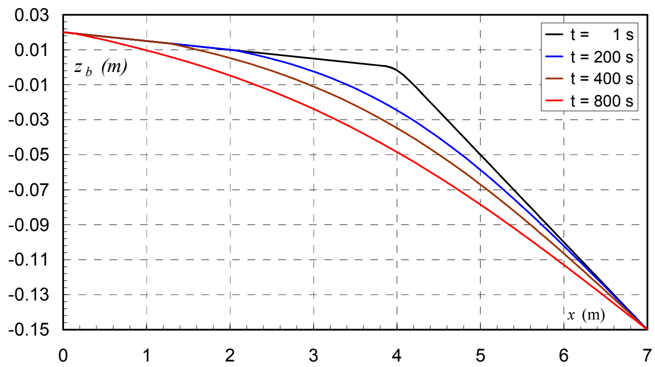

Figure 6.15a: Finite-channel example

Fig. 6.15b presents the results at times $t = 1$, 1800s, the first one representative of the initial conditions. The initial position of the fictitious symmetrical knickpoint is located at $x_{o'}$ =10 m

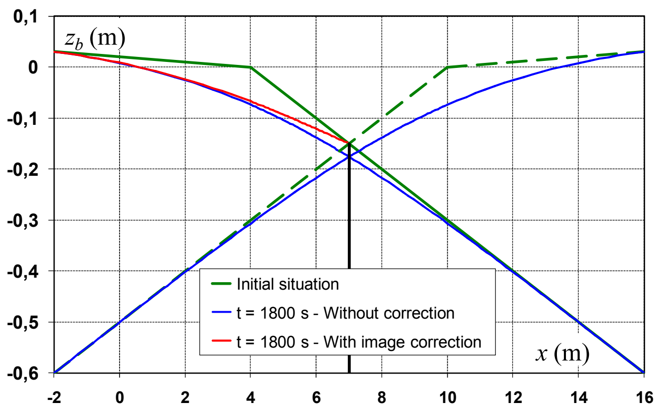

Figure 6.15b: Finite-channel example with image correction

The analytical solution for the case an infinite channel is compared to a finite-difference discretization (see section 5.4) of the diffusion equation (6.3). Results are shown in Fig. 6.16, for case where $S_1 = 0.5$ %, $S_2 = 5$ %, $D = 0.4$ m^2/s and $\lambda = -0.9676$.

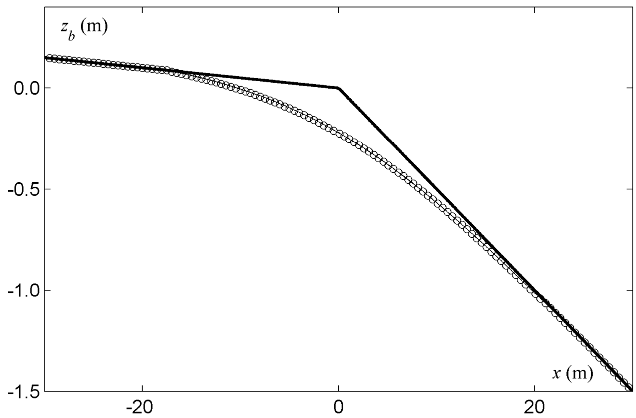

Figure 6.16: Infinite channel: analytical (thin continuous line) and numerical (dots) solution after $t = 500$ s. The initial conditions indicated by a thick black line.

6.4 Numerical simulations

For the same reasons expressed previously in section 5.5, we will not use the SedRiv numerical model based in the implicit four point scheme. A two-layer model described briefly in section 5.5.1 will be used to simulate a transcritical flow over finite mobile bed induced by the presence of a knickpoint (Savary et al., 2006).

6.4.1 Two-layer model

Results of the numerical computation of knickpoint migration for run #1 are obtained for the main parameters summarised in Table 6.1. Beside those parameters, the following data (Savary, 2006) were necessary to work out the simulations: numerical domain length $L = 6.9$m; the friction coefficients C_{fw} =0.025 and C_{fs}= 0.079; the sediment concentration CS=0.22; spatial mesh size is fixed in 1cm-long cells, and the time step is calculated according to the well known Courant-Friedrich-Levy condition (CFL) with a CFL number of 0.7.

The initial preformed knickpoint is presented in Fig. 6.17 where the non-erodible bed, corresponding to the bottom of the flume, is fixed at 0.11 m.

The initial bed level $z_b(x,0)$ is supposed as the regression straight line through the experimental bottom level measurements. Fig. 6.18 depicts a comparison between the initial experimental and numerical water and bed profiles. A set of comparison results is given henceforward in Fig. 6.19.

a)

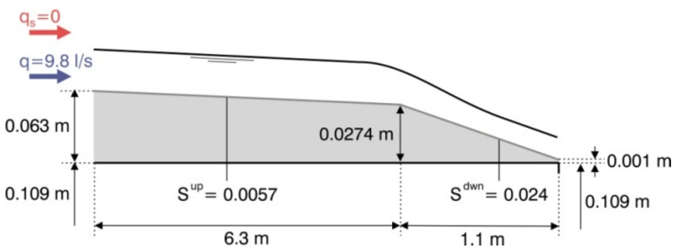

Figure 6.17: Initial conditions (data of the Figure from Savary et al., 2006)

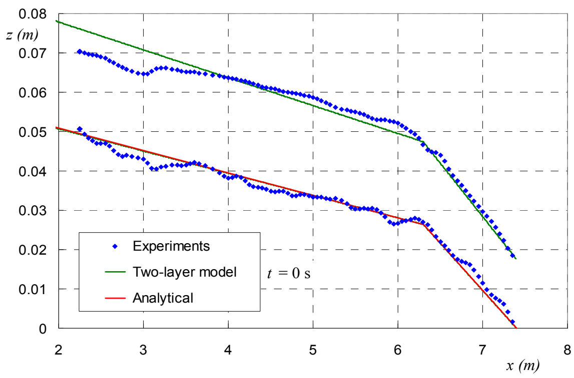

Figure 6.18: Comparison between experimental, analytical and computed levels: initial conditions

6.5 Comparisons

Sample results (run #1) corresponding to experimental, analytical and numerical approaches are presented and compared hereafter. The comparison concerns only the time evolution of bed and free surface.

All the Figures are plotted with the same conventions: time $t = 0$ corresponds to time once the experimental conditions were reached; horizontal co-ordinates are in meters, origin is placed at the upstream end of the flume; vertical co-ordinates are in metres above the bottom of the flume at the downstream end.

Numerical and experimental profiles of run # 1 compare favourably, as it can be seen in Fig. 6.19. It can be observed that the formation of the knickpoint influences the hydrodynamic evolution of the system in the following way: upstream of the knickpoint, a M_2 profile exists, while downstream of the knickpoint, a S_2 profile develops. The junction between these two profiles defines a critical section corresponding to the knickpoint location where the abrupt growing of a bed shear stress creates an erosion front propagating upwards (Bellal et al., 2004) and causing the erosion of sediment in the flume. Thus, the bed transforms progressively to one bed slope leading the knickpoint and the control section to disappear.

At the downstream end, the bed level remains unchanged during the entire experiment and the computation. The downstream slope decreases, taking this fixed boundary condition as tilting point. Given that there is no sediment furnished upstream, the computed flow consequently erodes a part of the bed at the upstream end to make up a transport layer. This erosion area expands downwards with time. In the downstream part, the computed bed level is a little higher than the experimental one from $t = 465$ s.

On the same Figures, we can observe that the analytical self-similar solution for the case of a finite channel is compared with both experimental and numerical approaches. Upon computation of the diffusion coefficients D from (3.35) and calibration of S_{min} (the slope threshold), it is seen that the solution is in good agreement with the measured and computed profiles.

Despite the simpler governing equations used, the quality of the agreement is similar to that reached using a more complicated two-layer shallow water numerical model.

(a)

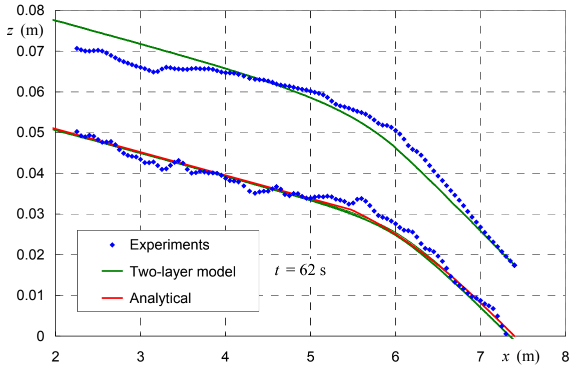

(b)

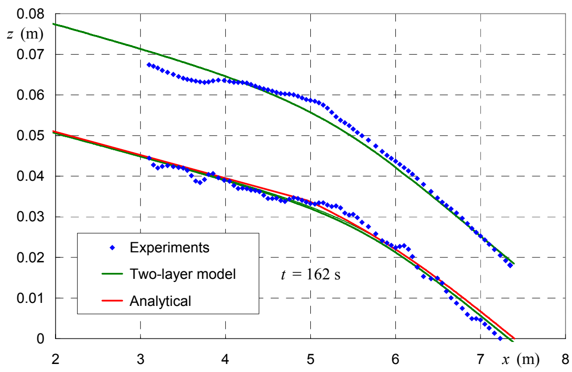

(c)

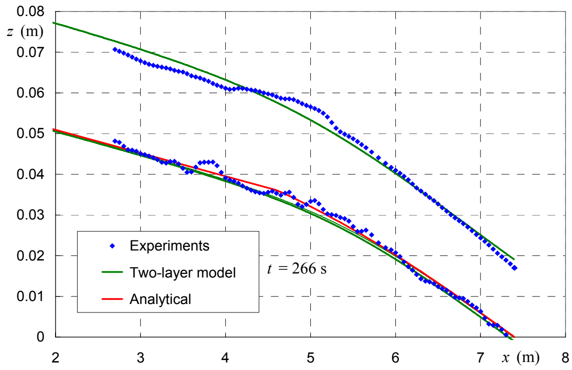
0.08
z (m)
0.07
0.06
0.05
0.04
0.03
0.02
0.01
0
2
3
4
5
6
7
x (m)
8
Experiments
Two-layer model
Analytical
t = 266 s

(d)

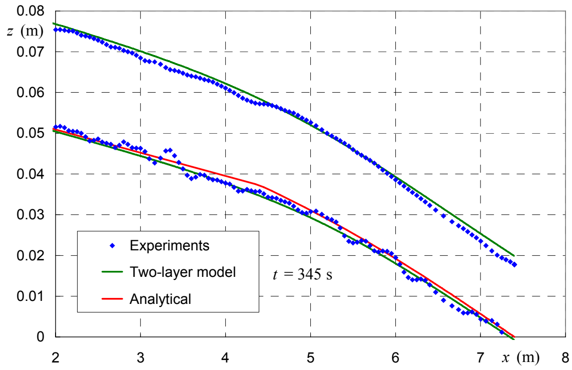
0.08
z (m)
0.07
0.06
0.05
0.04
0.03
0.02
0.01
0
2
3
4
5
6
7
x (m)
8
Experiments
Two-layer model
Analytical
t = 345 s

(e)

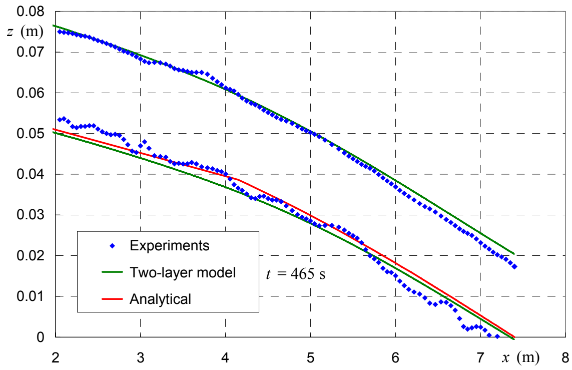
0.08
z (m)
0.07
0.06
0.05
0.04
0.03
0.02
0.01
0
2
3
4
5
6
7
x (m)
8
Experiments
Two-layer model
Analytical
t = 465 s

(f)

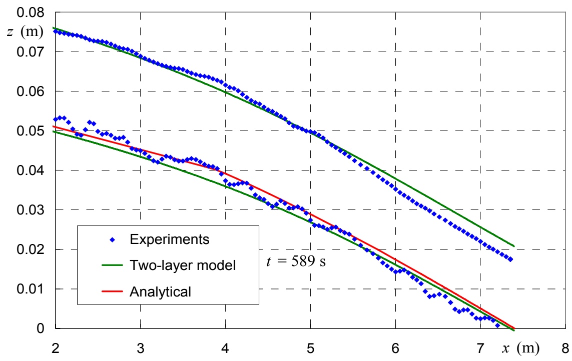

(g)

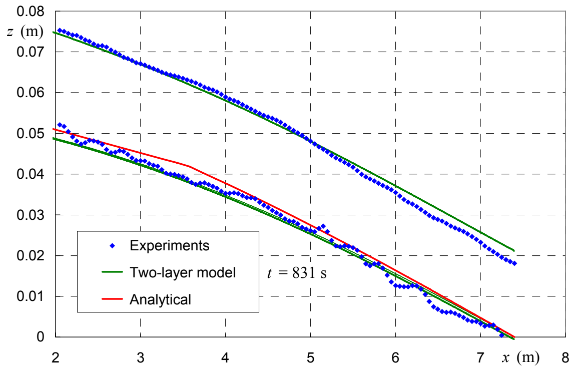

Figure 6.19: Comparison between experimental and numerical levels: time-evolution (62 s – 831 s)

The presented experiment was also simulated by means of another numerical model developed by Leopardi (2001). It is based on an explicit predictor/corrector MacCormak scheme for the coupled resolution of the Saint-Venant-Exner equations. A part of these results is exposed in Bellal et al. (2004), but therefore, supplementary instabilities occur and the results are less convincing.

6.6 Conclusions

Experiments were carried out in the UCL laboratory flume to study the morphodynamic evolution of rivers with the presence of a knickpoint and critical section created by a sudden change in bed slope from mild to steep slope. This transition of regime is a consequence of upstream and downstream boundary conditions which induce an important change in flow, bed evolution and bedload transport. To give an idea on the intensity of bedload transport upstream and downstream of the critical section, we note, for example, that for run#2 at 27 s during the initial stage, the bed shear stress downstream of the knickpoint is three times higher than the bed shear stress upstream, Bellal et al. (2004).

Two distinct stages of the bed evolution were identified: (a) propagation of an erosion wave upstream at approximately the same speed than the critical section and conversion of this wave into simple erosion wave when the critical section reaches the upstream section; (b) the supercritical flow takes over the whole reach; then the erosion wave propagates downward as simple degradation front. This behaviour is governed by downstream boundary conditions (a fixed bed level). From the comparison of the various runs, we can observe that both water discharge and the initial bed slope downstream of the knickpoint have substantial effect on the downstream bed slope evolution.

An analytical solution for the case of a migrating knickpoint in an erodible channel was presented. The analytical solution is derived from a diffusion equation first to model the knickpoint migration process in an infinite channel. The solution was then particularized to finite-length channels, corresponding to more realistic situations where boundary conditions exist. Laboratory measurements of such a migrating knickpoint are used to validate the analytical solution after adequate calibration of the two parameters governing the diffusivity and the slope threshold. Further work should be devoted to a sensitivity analysis of the analytical solution to these parameters with the aim of providing some guidance in the choice of the values.

The results of the simulations by a two-layer model are compared to the experiments and the analytical self-similar solution in finite channel. The comparison gave overall satisfactory results.

Chapter 7

Conclusions

In the nature, super-and transcritical flows can occur in lowland as in mountainous rivers and have a significant impact on the bed morphology. This type of flow may modify the mechanism of sediment transport and consequently the valley morphology. For example, in the transition from super- to subcritical flow regime through a hydraulic jump, the discontinuities in water levels and velocities between both regimes change the sediment transport capacity. This modification generates a sediment deposition which progressively turns into a sediment front that replaces the discontinuity in the water level.

To understand this mechanism in both super-and transcritical flows, experimental and analytical approaches were used and confronted to numerical simulations. The SedRiv model based on the implicit Preissmann scheme has been used to model the morphological evolution under supercritical flow, and a finite-volume two-layer model has been used to model the moprhodynamics of transcritical flow.

First, the experimental set-up has been designed and constructed with success since it allows conducting various kinds of experiments in adapted conditions (Chapter 2). In the framework of this thesis, three kinds of experiments have been conducted for various range of hydraulic and sediment parameters: (i) aggradation and degradation in supercritical flow; (ii) prograding sediment front and hydraulic jump and (iii) knickpoint migration and associated migration of control section.

Regarding the numerical approach, a classical eigenvalues analysis of the Saint-Venant–Exner equations has been operated by mean of the partial derivatives method. This analysis leads to three characteristics celerities, which constitute a guide for specification of the boundary conditions in super- and transcritical flows (Chapter 3).

(1) Morphodynamics of supercritical flow

For channels of infinite length, analytical solutions based on the linear diffusion model of de Vries (1973) are known to compare reasonably well with experimental measurements. Analytical solutions have been derived as well for channels of finite length (Gill, 1983) but do not appear to have been confronted with experimental data. In the present work (Chapter 4):

• We showed how the analytical solutions of Gill (1983) compare with full numerical results and with new measurements obtained in a steep-sloped laboratory flume.

• From the theoretical analysis, we obtained an explicit expression for the response time and also compared this with the empirical response times from our own data and from data of other investigators (Yen et al., 1992; Bianco et al., 1994).

(2) Morphodynamics of prograding sediment front and hydraulic jump.

Thanks to non-intrusive digital imagery methods, experiments concerning the prograding sediment front induced by the presence of a hydraulic jump permitted us to detect two stages of bed deformation, non perceivable with common bed profilers: (a) the appearance of small humps at the jump, propagating upwards, and (b) the development of a sediment bore, progressively substituting to the hydraulic jump. The humps propagation was described theoretically by different authors such as Sieben (1999) but not captured experimentally before the present work. This early stage was compared to a finite-volume two-layer model (Chapter 5).

Based on the analytical work of Voller (2004) developed for a zero channel length, the present work illustrates at the theoretical level the existence of a general mathematical structure shared by several sedimentary problems featuring semi-infinite channels evolving under diffusional sediment transport in case where moving boundaries are considered at one end of the channels. In the case of a prograding delta into a body of standing water (lake or sea), the compatibility condition consists in equating the rate of variation of the underwater sediment volume with the solid discharge furnished by the alluvial channel at the edge of the water body.

This new analytical solution related to prograding sediment front has been compared to experimental data and to results of two-layer numerical model. The comparison showed a good agreement but unsurprisingly, the analytical solution is not able to address the propagation of the first humps.

(3) Morphodynamics of Knickpoint migration and control section

Our experiments on the knickpoint migration exhibit two distinct phases of the bed evolution: (a) propagation of an erosion wave upstream at approximately the same speed as the associated control section and (b) conversion of this wave into simple erosion wave when the critical section reaches the upstream section. This wave propagates downward as a simple degradation front. The fixed bed level at the downstream end controls this behaviour (Chapter 6).

The linear diffusion equation, which rapidly eliminates slope discontinuities, would therefore appear to be a poor candidate to model the corresponding profile evolution. The survival of sharp knickpoints, however, can be achieved within a diffusion description by treating the knickpoints as migrating internal boundaries. Using this approach, we show that analytical solutions can be found for evolving profiles with migrating knickpoints (Chapter 6).

• We derive an exact solution for channel reaches of semi-infinite extent on both sides of the knickpoint and use it to construct an approximate solution for the more realistic case of a finite channel.

• The analytical self-similar solution of the diffusion equation presented in this work is compared to experimental measurements and results from the two-layer model. This comparison showed their good concordance.

One of the major goals of the present work was to develop the self-similar analytical solutions before discussing the advantage and possible uses of the derived analytical solutions. The rather drastic assumptions needed to derive them must again be recalled:

• Surface water is reduced to a diffusion agent (in active alluvial reaches) or to a boundary condition (at the edge of the body of standing water)

• Simple initial profile

• Constant channel width

• Steady supply of water and sediment

Considering those restrictions are accepted, however, the approach leads to a number of advantages:

• Exact solutions are obtained, free from the accuracy limitations of numerical calculations, as the solutions come from a transparent analytical procedure instead of an algorithmic black box.

• They also provide a clearer view of the role of various boundary conditions and control parameters.

• Most importantly, the solutions highlight the common mathematical structure underlying geomorphic problems as diverse as prograding deltas and knickpoint.

It is hoped that the proposed solutions will be helpful for various purposes. Comparison of their predictions with laboratory data could allow a better appraisal of the diffusional theory of fluvial morphodynamics. The solutions may also be used to validate numerical methods before applying the latter to more realistic problems. Alternatively, the solutions themselves could be helpful for analysing of field events, yielding typical time scales, modes of evolution, and distributions of deposit volumes once rough estimates of slopes and diffusion coefficients are available. Finally, the existence of these solutions in addition to the previously known results suggests that the family of explicit analytical solutions may be larger than expected, and that further research should be worthwhile.

Obviously, the present research treats only an isolated aspect of the morphodynamics of super- and transcritical flows and many improvements are still to be undertaken. In this ultimate section we do some suggestions for future investigations:

• Exploring prograding delta in 2D situation induced by sudden or progressive cross section enlargement downstream

•Considering non uniform sediment size distribution and various soil erodibility.

On the other hand, another analytical approach could be undertaken to model the prograding delta at the downstream boundary condition, using the rate of the discontinuity propagation obtained from the Rankine-Hugoniot shock relations (Sieben, 1999).

References

ABBOTT, M.B. (1979). *Computational hydraulics. Elements of the theory of free-surface flows*. Pitman, London.

ACKERS, P., WHITE, W.R. (1980). "Bed material transport: a theory for total load and its verification". *International Symposium on River Sedimentation, Beijing, China, March 1980*, *pp. 249-268*.

ARMANINI, A., DI SILVIO, G. (1988). "A one-dimensional model for the transport of a sediment mixture in non-equilibrium conditions". *Journal of Hydraulic Research*, 26, *pp. 275-292.*

ARMANINI, A., LARCHER, M. (2001). "Rational Criterion for Designing of Slit-Check Dam*". Journal of Hydraulic Research, IAHR, 127(2), pp. 94-104.*

BATHURST, J, C, GRAF, W; CAO, H, H. (1987) " *Bed load discharge equations for steep mountain rivers", in " Sediment transport in gravel-bed rivers*", John Wiley & Sons Ltd, *pp.453-477*.

BARRY, Y., BULTOT, F. (1996) "Conception et Construction d'un Canal à Forte Pente de Fond Hydraulique", Travail de fin d'études; Université Catholique de Louvain, Louvain-la-Neuve, BELGIQUE.

BEGIN, Z.B., MEYER, D.F., SCHUMM, S.A. (1981), Development of longitudinal profiles of alluvial channels in response to base level lowering: *Earth Surface Processes and Landforms, v. 6, no. 1, pp. 49-68.*

BHALLAMUDI, S, M., CHAUDRY, H. (1991) "Numerical modelling of aggradation and degradation in alluvial channels", *Journal of hydraulics Division, Proc. of American Society of Civil Engineers, Vol. 117, n°. HY9, pp. 1145-1164.*

BIANCO, G., ROSSO, M., SCHIARA, M. (1994), "Studio teorico e sperimentale di alcuni aspetti dei fenomeni di ripascimento e erosion nei corsi d'aqua naturali", *Internal report, DITIC di Torino, 12 p*.

BLAIR, T.C. (2001), Outburst flood sedimentation on the proglacial Tuttle Canyon alluvial fan, Owens Valley, California, USA: *Journal of Sedimentary Research, v. 71, no. 5, pp. 657-679.*

BOXUS, L., DE ROOVER, C. (1997) "*Conception et Réalisation d'un dispositif d'essais sédimentologiques, Transport Solide dans le cas d'Ecoulement Supercritiques*" Université Catholique de Louvain, Louvain-la-Neuve, Belgique (in French).

BELL R.G., SUTHERLAND A.J. (1983). "Non-equilibrium bed load transport by steady flow". *Journal of Hydraulic Engineering, ASCE, 109(3), pp. 351-367.*

BELLAL, M., UPPALURI, BINDU.M., FERDJALLAH, L. AND ZECH, Y. (2000) " Some hydraulic aspects in the design of rectangular settling tanks" *Procedings 10 th conference on "sediment and sedimentation particles", Wroclaw, Poland, September 2000, pp. 291-301.*

BELLAL, M., SPINEWINE, B., SAVARY, C., ZECH, Y. (2003). "Morphological evolution of steep-sloped river beds in the presence of a hydraulic jump: Experimental study". *Proceedings of XXX IAHR Congress, Thessaloniki, Greece, August 2003, Vol. C-II, pp. 133-140.*

BELLAL, M., IERVOLINO, M., ZECH, Y. (2004). "Knickpoint migration process: experimental and numerical approaches". *Procedings 12 th conference on "sediment and sedimentation particles", Prague, Czech Republic, September 2004, pp. 185-195.*

BELLAL, M., SAVARY, C., ZECH, Y. (2005). "Morphological evolution of steep-sloped river beds in the presence of a hydraulic jump: Numerical and experimental analysis". *Proceedings of XXXI IAHR Congress, Seoul, Korea, September 2005, Theme C-05, pp. 1522-1533.*

BELLAL, M., CAPART, H., SOARES-FRAZÃO, S AND ZECH., Y. (2009) "Analytical, experimental, and numerical models of knickpoint migration" *publication in the proceedings of the 7TH IAHR sympsoium on River, Coastal and Estuarine Morphodynamics. Santa Fe Argentina, 2009, pp. 57-63.*

BRUSH, L.M., WOLMAN, M.G. (1960). "Knickpoint behavior in non-cohesive material: A laboratory study". *Bulletin of Geological American Society 71(1), pp. 59-73.*

BUSNELLI, M.M., STELLING, G.S., LARCHER, M. (2001). "Numerical morphological modeling of open-check dams". *Journal of Hydraulic Engineering, 127(2), pp. 105-114.*

CAPART, H., BELLAL, M., BOXUS, L., DE ROOVER C., ZECH, Y. (1998). "Approach to morphological equilibrium for steep-sloped river beds". River sedimentation - Theory and Applications*, Proceedings of the seventh International Symposium on River Sedimentation, Hong-Kong, Japan, December 1998, pp. 231-237.*

CAPART, H. (2000). "*Dam-break induced geomorphic flows and the transition from solid- to fluid-like behaviour across evolving interfaces*". PhD thesis, Université catholique de Louvain, Louvain-la-Neuve, Belgium.

CAPART, H., YOUNG, D.L. (2002). "Two-layer shallow water computations of torrential geomorphic flows". *Proceedings of River Flow 2002, Louvain-la-Neuve, Belgium, September 2002, pp. 1003-1012.*

CAPART, H., YOUNG, D.L., ZECH, Y. (2002); "Voronoï imaging methods for the measurement of granular flows". *Experiments in Fluids, 32, pp. 121-135.*

CAPART, H. (2004). *Shallow flow. Lecture notes*, National Taiwan University

CAPART, H., BELLAL, M., YOUNG, D.L. (2007). "Self-similar evolution of semi-infinite alluvial channels with moving boundaries*". Journal of Sedimentary Research, 76, pp. 7-17.*

CHANG, H, Y, SIMONS, B, D. (1970) "The Bed Configuration of Straight Sand-Bed Channels When Flow is Nearly Critical", *Journal Of Fluid Mechanics, Vol. 42, part 3, pp 491-495*

CHAUDRY, M, H. (1993) " *Open channel flow* ", Prentice hall, New Jersy, USA.

CHENG, N, S. (1997) "Simplified Settling Velocity Formula for Sediment Particle", *Journal of hydraulics Division, Proc. of American Society of Civil Engineers, Vol. 123, n°. HY2, pp. 149-152.*

CHEN, S.C., PENG, S.H., CAPART, H. (2007). “Two-layer shallow water computation of mud flow intrusions into quiescent water”. *Journal of Hydraulic Research, 45(1), pp. 13–25.*

CORREIA, L.R.P., KRISHNAPPAN, B.G., GRAF, W.H. (1991). “Laboratory verification of a coupled unsteady flow model”. *Proceedings of XXIV IAHR Congress, Madrid, Spain, 1991, pp. A471-A480.*

CORREIA, L.R.P., KRISHNAPPAN, B.G., GRAF, W.H. (1992). “Fully coupled unsteady mobile boundary flow model”. *Journal of hydraulic Engineering, 118(3), pp. 476-494.*

CORREIA, L.R.P. (1992). “*Numerical modelling of unsteady sediment transport*”, PhD thesis, Ecole Polytechnique Fédérale de Lausanne, Lausanne, Switzerland.

CRANK, J. (1984), "*Free and moving boundary problems*", Clarendon press.Oxford.

CUNGE, J.A., PERDREAU, N. (1973). Mobile bed fluvial mathematical model. *La Houille Blanche* 7, *pp. 561-570.*

CUNGE, J.A., HOLLY, F.M., VERWEY, A. (1980). *Practical aspects of computational river hydraulics*. Pitman Advanced Publishing Program, London.

DAUBERT, A., LEBRETON, J.C. (1967).“Etude experimentale et sur modèle mathématique de quelques aspects des processus d’érosion des lits alluvionnaires, en régime permanent et non permanent”. *Proceedings of XII IAHR Congress, 3 (in French).*

DE JAEGER, J. (1991) "*Influence de la Morphologie des Sables sur leur Comportement Mécanique*", Thèse de doctorat Université Catholique de Louvain, Louvain-la-Neuve, Belgique (in French).

DE VRIES, M. (1965). “Consideration about non-steady bed-load transport in open channels”. *Proceedings of the XI IAHR Congress, Leningrad, USSR, 1965, vol. 3, no. 3.8.*

DE VRIES, M. (1973). River-bed variations-aggradation and degradation. *Int. Seminar on Hydraulics of Alluvial Streams, IAHR, New Delhi, (India), 1973, 20 p.*

DEWANDRE, C., LOSSEAU, N. (2004). *Evolution morphologique d’une rivière à l’aval d’un seuil déversant : Etude expérimentale*. Diploma work, Université catholique de Louvain, Louvain-la-Neuve, Belgium (in French).

DI CRISTO, C., LEOPARDI, A., GRECO, M. (2002). “A bed-load transport model for non-uniform flows”. *Proceedings of River Flow 2002, Louvain-la-Neuve, Belgium, September 2002, pp. 859-863.*

DI SILVIO, G, PEVIANI, M. A. (1989). “Modelling Short and Long-term evolution of mountain rivers: an application to the torrente Mallero” Int workshop on fluvial hydraulics of Mountains regions. Trent, Italy.

EINSTEIN, H.A. (1950). “The bed load function for sediment transportation in open channel flows”. *Tech. Bull.1026, U.S. Department of Agriculture, Soil Conservation Service, Washinton D.C.*

FENNEMA, R.J., CHAUDHRY, H. (1986). Explicit numerical schemes for unsteady free-surface flows with shocks. *Water Resources Research., 22(13), pp. 1923-1930.*

FERNANDEZ LUQUE R., E VAN BEEK, R. (1976). Erosion and transport of bedload sediment. *Journal of Hydraulic Research, 14(2), pp. 127-144.*

GAUDIO, R., MARION, A., BOLOVIN, V. (2000). “Morphological effets of bed sills in degrading rivers”. *Journal of Hydraulic Research, 38(2), pp. 89-96.*

GAUDIO, R., MARION, A. (2003). “Time evolution of scouring downstream of bed sills”. *Journal of Hydraulic Research, 41(3), pp. 271-284.*

GILL, M.A. (1983) "Diffusion model for aggrading channels", *J. Hydr. Res., IAHR, 21(5), pp. 355-367.*

GOUTIERE, L., LARAICHI, T. (2006). *Modèle d'évolution morphologique fluvial de Saint-Venant–Exner : Analyse numérique et validation expérimentale*. Diploma work, Université catholique de Louvain, Louvain-la-Neuve, Belgium (in French).

GOUTIÈRE, L., SAVARY, C., SOARES-FRAZÃO, S., SPINEWINE, B., BELLAL, M., ZECH., Y. (2007). "Comparison between a St-Venant–Exner model and a two-layer model for transient flows". *Publication in the proceedings of the 5TH IAHR sympsoium on River, Coastal and Estuarine Morphodynamics. Netherland, 17-21 September 2007, pp. 465-472.*

GOUTIÈRE, L., SOARES FRAZÃO, S., SAVARY, C., LARAICHI, T., ZECH, Y. (2008). "One-dimensional model for transient flows involving bedload sediment transport and changes in flow regimes". *Journal of Hydraulic Engineering, ASCE, 134 (6), pp. 726-735.*

GOUTIÈRE, L., BELLAL, M., SOARES-FRAZÃO, AND ZECH., Y. (2009). "Experimental, analytical and numerical simulation of the propagation of a hydraulic jump over mobile bed" *Proceedings of XXXIII IAHR Congress, Vancouver Canada, August 2009, pp. 5076-5082.*

GRAF, H.W., ALTINAKAR, M.S. (1998). *Fluvial Hydraulics. Flow and transport processes in channels of simple geometry*. Chichester, Wiley.

GRAF, H. W, H., SUSZKA, L (1987) "Sediment transport in steep channels", *Journan of Hydroscience and Hydraulic Engineering, Vol. 5, n° 1, pp. 11-26*

HYDON, P.E., (2000), *Symmetry Methods for Differential Equations*, Cambridge University Press.

JAIN, S.C. (1981) "River bed aggradation due to overloading", *J. Hydr. Div., ASCE, 107(1), pp. 120-124.*

KOSTIC, S., PARKER, G. (2003). Progradational sand-mud deltas in lakes and reservoirs. Part 1. Theory and numerical modeling: *Journal of Hydraulic Research, v. 41, no. 2, pp. 127-140.*

KEVORKIAN, J. (2000). "*Partial differential equations, analytical solutions techniques*", Springer editions.

HIRSCH, C. (1997). *Numerical Computation of Internal and External Flows*. Wiley, UK

HOLLY, F. M., RAHUEL, J.-L. (1990). "New Numerical/Physical Framework for mobile-bed modelling, Part 1: Numerical and physical principles". *Journal of Hydraulic Research, 28(4), pp. 401-416.*

HSU, J.P.C., AND H. CAPART (2008) Onset and growth of tributary-dammed lakes. *Water Resources Research, 44, art. W11201, pp. 1–6.*

IERVOLINO, M. (2005). *Transporto solido di fondo in condizioni non stazionare: modellazione monodimensionale*. PhD thesis, Università degli Studi di Napoli "Frederico II", Naples, Italy (in Italian).

JANSEN, P.PH., VAN BENDEGOM, L., VAN DEN BERG, J., DE VRIES, M., ZANEN, A. (1979). *Principles of River Engineering. The non-tidal alluvial river*. London, UK Pitman.

KABIR, M.R.. (1993), "*Bed Load in Unsteady Flow*", Thèse de doctorat; Université Catholique de Leuven, Leuven, Belgium.

LAI, S.Y.J., AND CAPART, H. (2007), Two-diffusion description of hyperpycnal deltas, *J. Geophys. Res., 112, F03005*.

LAI, S.Y.J., AND CAPART, H. (2009) Reservoir infill by hyperpycnal deltas over bedrock. *Geophysical Research Letters 36, art. L08402, pp. 1–6.*

LEOPARDI, A. (2001). *Modeli Bidimensionali Di Corpi Idrici Naturali*. PhD thesis, Università degli Studi di Napoli "Frederico II", Naples, Italy (in Italian).

LEVEQUE, R.J. (2002). *Finite Volume Methods for Hyperbolic Problems*. Cambridge University Press.

LIGETT, J.A. (1994). *Fluid Mechanics*. McGraw-Hill, New-York.

LIN, M.S., TSAI, C.T. (1991) "Modeling of riverbed evolution with gradually varied unsteady supercritical flow", *J. Chinese Inst. Civil Hydr. Engrg, 3(1), pp. 37-49 (in Chinese).*

LYN, D.A. (1987). “Unsteady sediment transport modelling”. *Journal of Hydraulic Engineering, 113(1), pp.1-15.*

LYN, D.A., ALTINAKAR, M. (2002). “St-Venant-Exner Equations for Near-Critical and Transcritical Flows”. *Journal of Hydraulic Engineering, ASCE, 128(6), pp. 579-587.*

MESELHE, E.A., HOLLY, F. (1997). “Invalidity of Preissmann Scheme for Transcritical Flow”. *Journal of Hydraulic Engineering, 123(7), pp. 552-554*

MEI, C.C. (1995) *Mathematical Analysis in Engineering*, Cambridge University Press, Cambridge, U.K.

MEYER-PETER, E., MÜLLER, R. (1948). “Formulas for bed-load transport”. *2nd IAHR Congress, Stockolm, 1948, pp. 39-64.*

MITCHELL, N.C. (2006), Morphologies of knickpoints in submarine canyons, *Geol. Soc. Am. Bull., 118, pp. 589–605.*

MIZUYAMA, T (1977), "*Bedload Transport in Steep Channels*". PhD. Thesis, University of Koyoto, Koyoto, Japan.

MUTO, T. (2001), Shoreline autoretreat substantiated in flume experiments: *Journal of Sedimentary Research, v. 71, no. 2, pp. 246-254.*

PAOLA, C., HELLER, P.L., ANGEVINE, C.L. (1992), The large-scale dynamics of grain-size variations in alluvial basins*: Basin Research, v. 4, pp. 73-90.*

PAOLA, C. (2000), Quantitative models of sedimentary basin filling: *Sedimentology, v. 47, suppl. 1, pp. 121-178.*

PARKER, G., MUTO, T.(2003) “1D numerical model of delta response to rising sea level”: *Proc. 3rd IAHR Symposium on River, Coastal and Estuarine Morphodynamics, Barcelona, pp. 558-570.*

PENG, S.H. (2004). *Geomorphic change induced by the flow of mud and debris surges into river channels*. PhD thesis, National Chung-Hsing University, Taiwan.

PHILLIPS, B.C., SUTHERLAND, A.J. (1989). “Spatial and lag effects in bed load sediment transport”. *Journal of Hydraulic Research, 27, pp. 275-292.*

PHILLIPS, B.C., SUTHERLAND A.J. (1990). “Temporal lag effect in bed load sediment transport”. *Journal of Hydraulic Research, 28, pp. 5-23.*

PREISSMANN, A. (1961). “Propagation des intumescences dans les canaux et rivières”. *1er Congrès de l’Association Française de Calcul, Grenoble, France, pp. 433-442.*

RAHUEL, J.L. (1988). “ Modélisation de l’évolution du lit des rivières alluvionnaires à granulométrie étendue ” (in French). *Institut National Polytechnique de Grenoble, Grenoble, France.*

RAUDKIVI, A, J. (1991) " *Loose Boundary Hydraulics*", 3 rd edition, Pergamon Press, London Uk.

RIBBERINK, J.S., VAN DER SANDE, J.T.M. (1985), “Aggradation in rivers due to overloading – analytical approaches”*: Journal of Hydraulic Research, v. 23, no. 3, pp. 273-283.*

RICHTMYER, R, D. (1957) " *Defference Methods for Initial Value Problems* " Interscuence Tracts in Pure and applied Mathématics, Number 4, New York.

ROSSI, L. (2002). *Re-thinking the Var river training in Nice*. PhD Thesis, University of Genova, Italy.

SAVARY, C., ZECH, Y. (2006). “Can a two-layer morphological model compete with common sediment transport formulae?”. *Proceedings of River Flow 2006, Lisbon, Portugal, September 2006, pp. 825-832.*

SAVARY, C., BELLAL, M., ZECH, Y. (2006). “Two-layer approach for transcritical flow on mobile bed: knickpoint migration”. *Proceedings of River Flow 2006, Lisbon, Portugal, September 2006, pp. 1155-1163.*

SAVARY, C., ZECH, Y. (2007). “Boundary conditions in a two-layer geomorphical model. Application to a hydraulic jump over a mobile bed”. *Journal of Hydraulic Research, 45 (3), pp. 316-332.*

SAVARY, C (2007). “*Transcritical transient flow over mobile beds. Boundary conditions treatment in a two-layer shallow-water model*”. PhD thesis, Université catholique de Louvain, Louvain-la-Neuve, Belgium

SPINEWINE, B. (2005).”*Two-layer flow behaviour and the effects of granular dilatancy in dam-break induced sheet-flow”*. PhD thesis, Université catholique de Louvain, Louvain-la-Neuve, Belgium.

SIEBEN, J. (1995), "Study on one-domensional and discontinous river flows with mobile beds", *Communications on hydraulic and geotechnical engineering, report 95-3*, Delft University of Technology

SIEBEN, J. (1996), "One dimensional models for mountain-river morphology", *Communications on hydraulic and geotechnical engineering, report 96-2,* Delft University of Technology

SIEBEN, J. (1997). *Modelling of hydraulics and morphology in mountain rivers*. PhD thesis, Delft University of Technology, Delft, The Netherlands

SIEBEN, J. (1999). *“*A theoretical analysis of discontinuous flow with mobile bed”. *Journal of Hydraulic Research, 37(2), pp. 199-212.*

SLOFF, C.J. (1993). “Analysis of basic equations of sediment-laden flows”. Communications on Hydraulic and Geotechnical Engineering, *Report. No. 93-8*, Delft Unversity of Technology, Delft, The Netherlands.

SMART, G. (1984) "Sediment Transport Formula For Steep Slopes", *Journal of hydraulics Division, Proc. of American Society of Civil Engineers, Vol. 110, n°. HY3, pp. 267-276.*

SMART, G, JAEGGI, N, R. (1984) "Sediment Transport on Steep Slopes", *Rapport n° 64*, Mitteilungen der Versuchsanstalt fuer Wasserbau, Hydrologie und galziologie, Eidgenossischen Technishen Hochschule, Zurich, Switzerland.

SOARES FRAZÃO, S. (2002). *Dam-break induced flows in complex topographies. Theoretical, numerical and experimental approaches*. PhD thesis, Université catholique de Louvain, Louvain-la-Neuve, Belgium.

SONI, J.P., GARDE, R.J.,RANGA RAJU, K.G. (1980) "Aggradation in streams due to overloading", *J. Hydr. Div., ASCE, 106(1), pp. 117-132.*

SUSZKA, L (1987) , " *Sediment transport at steady and unsteady flow; a laboratory study*", Thèse de doctorat n° 704, Ecole Polytechnique Fédérale de Lausanne, Lausanne, Switzerland.

SWENSON, J.B., VOLLER, V.R., PAOLA, C., PARKER, G., MARR, J.G. (2000), Fluvio-deltaic sedimentation : A generalized Stefan problem: *European Journal of Applied Mathematics, v. 11, pp. 433-452.*

VOLLER, V.R., SWENSON, J.B., PAOLA, C., (2004), An analytical solution for a Stefan problem with variable latent heat: *International Journal of Heat and Mass Transfer, v. 47, no. 24, pp. 5387-5390.*

VREUGDENHIL, C.B., DE VRIES, M. (1967). "Computation of non-steady bed-load transport by a pseudo viscosity method", *Delft Hydr. Lab. Publ. No 45*, Delft, The Netherlands.

YEN, C.L., LEE, H.Y., CHANG, S.Y. (1987) "Some aspects of channel aggradation due to overloading of coarse material", *Proc. R.O.C.-Japan Joint Seminar on Water Res. Engrg, Taipei, Taiwan, pp. 49-59.*

YEN, C.L., CHANG, S.Y, LEE, H.Y. (1992) "Aggradation-degradation process in alluvial channels*", J. Hydr. Engrg, ASCE, 118(12), pp. 1651-1669.*

WHIPPLE, K.X., AND TUCKER, G.E., (2002), Implications of sediment-flux-dependent river incision models for landscape evolution: *Journal of Geophysical Research-Solid Earth, v. 107, no. B2, art. no. 2039.*

ZECH, Y., (1996). "MODELISATION MATHEMATIQUE DU TRANSPORT SOLIDE ET DE LA MORPHOLOGIE FLUVIALE. UNE VISION CRITIQUE". *L'EAU, LA MATIERE, L'HOMME, LHCN*, LIEGE,*pp. 475-487.*

ZECH, Y., SOARES FRAZÃO, S., SPINEWINE, B., BELLAL, M., SAVARY, C. (2005). "The morphodynamics of super- and transcritical flow". *Proceedings of RCEM 2005 International Conference on River, Coastal and Estuarine Morphodynamics*, *pp. 239-251.*